Characterization of Iron-Doped Titanium Dioxide by Electron Microscopy Techniques

by

Atieh Parisi Couri

Diplôme de Master, École Nationale Supérieure de Chimie de Paris, 2016

Diplôme d'Ingénieur, École Nationale Supérieure de Chimie de Paris, 2016

Bachelor of Engineering, Universidade de São Paulo, 2017

A Thesis Submitted in Partial Fulfillment

of the Requirements for the Degree of

MASTER OF APPLIED SCIENCE

in the Department of Mechanical Engineering

© Atieh Parisi Couri, 2022

University of Victoria

All rights reserved. This thesis may not be reproduced in whole or in part, by photocopy or other means, without the permission of the author.

We acknowledge and respect the lək̓ʷəŋən peoples on whose traditional territory the university stands and the Songhees, Esquimalt and W̱SÁNEĆ peoples whose historical relationships with the land continue to this day.

Supervisory Committee

Characterization of Iron-Doped Titanium Dioxide by Electron Microscopy Techniques

by

Atieh Parisi Couri

Diplôme de Master, École Nationale Supérieure de Chimie de Paris, 2016
Diplôme d'Ingénieur, École Nationale Supérieure de Chimie de Paris, 2016
Bachelor of Engineering, Universidade de São Paulo, 2017

Supervisory Committee

Dr Rodney Herring, Department of Mechanical Engineering
Supervisor

Dr.Barbara Sawicka, Department of Mechanical Engineering
Departmental member

Abstract

Access to clean water is essential for human health and dignity. The increasingly rapid population growth, combined with the emergence of resistant chemical compounds and more concentrated toxic residues in the effluent streams of treatment plants, point towards a decline in freshwater resources resulting in a global water crisis in the next decades. Current wastewater treatment plants rely on Advanced Oxidation Processes (AOPs) for the tertiary (or advanced) step of the treatment. Photocatalysis is one of such processes, by which semiconductors are exposed to radiation of specific wavelengths (traditionally UV) to generate Reactive Oxygen Species (ROS) that can degrade organic molecules through a chain of radical oxidation reactions.

Anatase titania (TiO_2) has been used for many decades as a photocatalyst. Its electronic band structure has a band gap of 3.2 eV, requiring radiation in the UV range to trigger its photocatalytic properties. One way to reduce the band gap energy and shift the absorption peak wavelength to the visible part of the spectrum (thus reducing operation costs) is by doping the photocatalyst particles with transition metal atoms. Iron (III) is a great candidate due to the placement of its conduction/valence bands within titania's band gap, its atomic radius similar to titanium (IV) and its variety of oxidation states. However, iron-doped anatase titania synthesized by ordinary sol-gel methods shows a photodegradation efficiency that is much lower than undoped anatase. Previous studies have shown that this is caused by an inconspicuous iron oxide layer on the surface of the catalyst particle, forming a physical barrier to the mobility of charge carriers that trigger the formation of ROS radicals. Small changes to the synthesis protocol, namely slowing down the hydrolysis of the Ti precursor by lowering the solution's pH and acid-washing the final product, have been shown to result in particles that are photoactive under visible radiation and boast an unobstructed reactive surface.

In this work, the novel Fe-TiO_2 photocatalyst is studied and characterized in terms of its particle size distribution, inner structure and composition using electron microscopy techniques. It is important to know the particle size profile arising from this novel synthetic method, as the presence of nanoparticles could pose a health risk whereas an abundance of oversized particles is undesirable from the perspective of chemical reaction engineering (low surface-to-volume ratio). Inner structure/composition analyses could reveal whether the iron content inside the photocatalyst segregates into iron oxides, which would hinder reaction rates by behaving as a recombination center for charge carriers. As well, gathering more information about the inner structure of the catalyst (such as degree of crystallinity) is desirable as that could help fine-tune the synthesis protocol in order to obtain optimal photocatalytic activity.

The particle size distribution studies using scanning electron microscopy revealed that the catalyst samples contain a significant fraction of nanoparticles (31.55% smaller than 100 nm), even though those particles represent a very small fraction of total sample volume (0.00015%) and reactive area (0.03%). Moreover, oversized particles (bigger than 5 μm) account for the biggest fraction of sample volume and reactive surface. It was suggested that the size distribution of the catalyst be shifted to intermediate particle sizes by introducing additional grinding and separation steps into the synthesis protocol.

The inner structure studies were carried using a combination of scanning, transmission and scanning-transmission electron microscopy, as well as spectroscopy methods such as EDX and

EELS to map composition. It was found that the original anatase lattice structure remained unchanged in terms of interplanar spacings and crystallographic orientations, indicating that the addition of iron impurities at the small concentrations used here (0.5at%) did not result in discernible changes to the lattice. The monocrystalline units of Fe-TiO_2 (termed crystallites) often appear to be bound together by amorphous material. No segregation of Fe was observed inside the particles at this concentration, as shown by the apparent homogenous composition of the catalyst across crystalline and amorphous regions. The external iron oxide contamination layer observed in previous studies was theorized to form during the later steps of the sol-gel process due to the precipitation of the iron content in solution that failed to be incorporated into the TiO_2 gel network. More in-depth studies must be carried to assess whether preferential segregation of iron within the catalyst could occur at higher dopant concentrations.

Table of Contents

List of Tables

List of Figures

Acknowledgements

I acknowledge once again the lək̓ʷəŋən peoples on whose traditional territory the university stands and the Songhees, Esquimalt and W̱SÁNEĆ peoples whose historical relationships with the land continue to this day. It is our responsibility, as settlers, to learn about how we came to be here and about the people on whose (unceded) lands we live. It is our job to recognize the tradition of colonialism in academia, and to work together to dismantle it. It is our responsibility to acknowledge indigenous peoples' traditional stewardship of the land and to include them in the fight against the climate crisis. It is up to us to do the work.

I would like to thank my research supervisor, Dr Rodney Herring, for all the scientific and moral support over the course of my degree. Despite the many bumps on the road, I could always count on his patience, guidance and expertise. My thanks also go to the members of this research group and of the Advanced Microscopy Facility at UVic for their valuable contributions: Dr Barbara Sawicka, Arthur Makosinski, Dr Elaine Humphrey, Dr Arthur Blackburn and Jonathan Rudge. Also, to my fellow graduate students who offered their support through both scientific insights and comraderie on all things related to the life of international graduate students: Zahra Jahanshahi, Muniyat Rafa and Faysal Ahmed. Finally, I would like to thank Dr Daniela Lavric from the Corning European Technology Centre in Avon, France, for teaching me how to marry theoretical and experimental research and setting me on this journey over 4 years ago.

I could not have completed this work without the incredible support of my friends and chosen family. Joël Lavigueur, my partner in life, and Emmanuel Moore, my close friend, deserve special mention as they were always there for me, through countless neuroses and weekly breakdowns, when things got tough and anxiety took over. It is said that where you are is only as good as who you are with – these two made Victoria, BC feel not only as a pit stop on my journey, but as my home. I am fortunate enough to have a support system that extends beyond borders: even from afar my sisters, Isabella and Marina, and my close friend, Larissa, were always willing to share in my frustrations and accomplishments.

I would also like to acknowledge the amazing work from health professionals and the office of the Provincial Health Officer in British Columbia during the many months of fear and uncertainty caused by the COVID-19 pandemic.

Finally, I would like to acknowledge and address an issue that many graduate students struggle with: mental health. Writing a thesis, while trying to balance work and any resemblance of a social life, can be extremely challenging. Anxiety, self-doubt, feelings of isolation and imposter's syndrome, among others, have a way of creeping in and stalling your progress to a halt. If you are reading this and find yourself dealing with these uninvited passengers living in your head, please remember to go easy on yourself and reach out for help. You are not alone.

Dedication

To my friends and chosen family,

Who supported me when it felt like

This Thesis would be the death of me.

Chapter 1 Introduction

This chapter contains an overall introduction to the work done towards the completion of this thesis. The motivation guiding this study is presented in detail, followed by a brief review of the theoretical background necessary to advance this research. Next, the structure of the thesis is discussed, and the novel aspects of this work are presented.

1.1. Motivation for study

Clean water is essential for human health, well-being and dignity, and its availability is a continuous cause for concern around the world. An estimated amount of 40% of the global population is affected by water scarcity, which is projected to rise to 50% by 2025 according to the World Health Organization. The increasingly rapid population growth and the projected decline in freshwater resources point towards an upcoming global water crisis in the next decades [1] [2].

One of the reasons for the decline in freshwater supply is the emergence of new compounds in the effluent streams of processing plants. Some of these new, harmful molecules are resistant to traditional wastewater treatment methods, such as PBDE (used in fire retardants), dyes, pesticides and other polycyclic aromatic hydrocarbons [3] [4] [5]. As well, in recent years the efforts towards waste minimization and water conservation have had the unintended consequence of more concentrated or toxic residues [6].

Treating water properly is crucial to prevent waterborne disease and other health burdens provoked by chemical contamination. A variety of thoroughly studied physical and biological processes are currently used in wastewater treatment facilities, such as chemical precipitation, filtration, bioreactors, etc. An additional treatment step (called tertiary, or advanced, treatment) has been increasingly adopted to include processes designed to target compounds which are not easily removed by conventional methods [7]. Advanced Oxidation Processes (AOP) are a class of chemical treatments designed to degrade organic matter in the system, often indirectly through generation of reactive oxygen species (ROS) [8]. The use of titanium dioxide (TiO_2) as a heterogeneous photocatalyst has become a popular method of generating the hydroxyl radical ($\bullet OH$), the strongest of oxidizing radicals with a redox potential of 2.8V, and as such adequate to completely mineralize organic molecules in wastewater [9].

Anatase TiO_2 is a semiconductor that has been extensively studied as a photocatalyst due to its electronic band structure (bandgap of 3.2 eV), high chemical stability, biocompatibility, and low cost. Upon exposure to photons having an adequately high energy, charge carriers are produced within the TiO_2 lattice which then percolate to the surface of the particles, triggering the chain of reactions that generate the reactive species at the interface with the reaction medium. Doping titanium dioxide particles with transition metal atoms has been shown to decrease the gap between conduction and valence bands, shifting the TiO_2 absorption band from the near-UV towards the visible spectrum. That, in turn, increases the range of applications of TiO_2 as a photocatalyst for wastewater treatment due to the lower cost of visible-light illumination compared to artificial UV sources, which make up a considerable fraction of the treatment cost [10] [11] [12] [13] [14] [15].

The iron (III) ion (Fe^{3+}) is considered to be a good candidate as a doping agent for anatase TiO_2 due to the following reasons:

- the d orbitals of iron and titanium interact to create additional electronic energy levels between titania's conduction and valence bands, lowering the crystal's electronic band gap and red-shifting the photocatalytic peak towards visible wavelengths [16];
- the atomic radius of Fe^{3+} and Ti^{4+} are similar (0.645 A and 0.605 A respectively), as well as the metal-oxygen bond length (1.95 A for Ti-O and 1.97 for Fe-O), facilitating the incorporation of iron atoms to the TiO_2 lattice at substitution sites [17] [18];
- the variety of oxidation states for iron (Fe^{3+}, Fe^{2+} and Fe^{4+}) allows it to dynamically trap both charge carriers (electrons and holes) on their path towards the particle surface, reducing recombination rates and consequently enhancing photocatalytic activity the best among transition metals [19].

Despite the theoretical advantages of using iron atoms as the doping agent, it has been shown that ordinary iron-doped titanium dioxide does not perform as well in photodegradation experiments as TiO_2 doped with other transition metals [5]. Our research group has recently shown that photocatalysis by ordinary Fe-TiO_2 is severely hindered by an inconspicuous iron oxide layer formed on the surface of the particles during synthesis, which inhibits surface reactions. By adjusting the amount of iron used for doping and including an acid-wash step to remove the iron oxide contamination layer during the synthesis, this research group was able to synthesize particles boasting an unobstructed reaction surface. Experiments have shown that the apparent reaction rate constants for the degradation of a model pollutant using Fe-TiO_2 under visible light (>400 nm) could be increased almost 20-fold using our novel synthetic method, becoming comparable to the rate constants of pure TiO_2 under UV light [20]. These particles can be easily deposited onto a glass substrate (flat glass, fiber glass cloth, etc.) through a variety of processes including dip-coating and sintering [21].

Considering the economic burden of current water treatment systems and the shortage in freshwater resources, as well as environmental constraints for wastewater disposal, it is essential to invest in technology that cleans water efficiently, that decreases operation costs and that can be easily implemented. The high performance of Fe-TiO_2 synthesized by this novel method in catalyzing the degradation of organic pollutants represents a significative development in the field of photocatalysis. It is trivial to fabricate and can easily be implemented in simple reactor designs as well as fitted to existing light-based water treatment technologies, increasing their cost-efficiency.

The goal of the studies presented in this work is to provide insights into the macroscopic and microscopic structure of the novel Fe-TiO_2 particles, ultimately leading to improvements in its fabrication protocols and catalytic activity. This is achieved by using electron microscopy techniques to determine the particle size distribution of Fe-TiO_2 samples and to investigate the lattice structure of the material as well as that of the amorphous material between monocrystals. The particle size distribution provides important information about the area available for surface reactions, as well as the presence of nanoparticles that could pose a threat for human and environmental health. The structural and compositional analysis of the lattice reveals how the monocrystals are organized into macroscopic aggregates, which affects the mobility of charge carriers (electrons and holes) percolating to the particles' surface to generate ROS.

1.2. Advanced Oxidation Processes

Advanced Oxidation Processes (AOPs) are a class of chemical techniques able to generate highly active Reactive Oxygen Species (ROS), such as hydroxyl radicals, under relatively mild conditions. These oxidating species are produced in high concentrations, which promote the degradation of most complex chemicals present in the solution [6] [8].

Hydroxyl radicals are one of the most common and powerful ROS produced from Advanced Oxidation Processes. Hydroxyl radicals are a powerful, non-specific oxidant that can be produced on-site to react with most organic compounds at high-rate constants, degrading them into fully mineralized end-products [7] [22]. Its oxidation potential stands at 2.73 V, providing faster reaction rates than conventional oxidizing agents such as H_2O_2 or $KMnO_4$ [23].

1.2.1. Uses in water treatment

Advanced Oxidation Processes are more generally employed as the final step in municipal or industrial treatment facilities, designed to remove specific compounds that persist in the wastewater even after traditional physical and biological separation processes. The importance of this final step of treatment is accentuated due to the ongoing shift in composition of domestic and industrial effluent streams, carrying dissolved compounds that are more resistant and/or more concentrated [6] [7].

A brief outline of the usual treatment steps in wastewater plants is as follows [7]:

- Pre-treatment: this step is usually carried within the industrial plants before the effluent stream is discharged to a central industrial sewage system. It is aimed to reduce the overall toxicity and impact of the wastewater stream on the rest of the treatment system, and usually designed to comply with local or federal regulations for emissions. Examples of processes that can be included in this step are flow equalization (which levels out hydraulic demands on treatment units caused by batch discharges), neutralization (of the wastewater's pH) and grease/oil removal (grease traps, separation by gravity).
- Primary treatment: processes designed to concentrate and remove suspended solids with the least amount of effort, usually employing physical separation techniques such as screening, filtration, grit chambers, sedimentation, and chemical precipitation (flocculation).
- Secondary treatment: biological processes that use microorganisms, referred to as "biomass" and usually composed of bacteria, to stabilize waste components and incorporate them as more biomass (reproduction). Design of this treatment step must account for the specific environment conditions required by the microorganisms employed (pH, temperature, nutrients, ionic balance, etc.), as well as the presence of electron acceptors (molecular oxygen, oxidized nitrogen, oxidized sulfur, etc.) to enable the oxidation of electron donors (waste). Biological processes are widely adopted because of their low cost, because they are self-sustaining due to the microorganisms' self-replication, and because most substances in the waste stream are amenable to biological breakdown. However, challenges include the need to remove and dispose of excess microorganisms from the system as "sludge" (increasing the operation costs) and managing factors that affect the biodegradability of certain compounds (molecular structure, concentration threshold for toxicity, solubility of pollutants, etc.). Processes belonging to this category of

treatments include activated sludges (both aerated and anaerobic), trickling filtration (using microbe biofilms) and lagoons/ponds (with different levels of aeration).

- Tertiary treatment: this is the class of processes which AOPs are a part of. Due to their elevated cost compared to secondary treatments, tertiary treatments are only implemented when it is necessary to remove specific solubilized pollutants not easily degraded by biomass. Processes that can be used in this step include adsorption, ion exchange, air stripping, selective membranes, and chemical oxidation processes (including AOPs).

1.2.2. Types of AOPs

The highly oxidizing environments characteristic of Advanced Oxidation Processes can be generated through several techniques, such as photochemical processes [24], photocatalysis [25], catalytic processes [26], cavitation [27], electrochemical oxidation [28], X-ray irradiation and γ-radiolysis [29], electron beam irradiation [30], radiation in general [31] and supercritical water oxidation [32].

Among the available techniques, photochemical and photocatalysis processes are favored due to their low cost for generating high concentrations of ROS. Semiconductor-mediated photocatalysis will be discussed in a separate section. Some other processes belonging to these two categories are listed below [15]:

- Photooxidation (UV photolysis) – used to degrade molecules that do not require an additional catalyst. The process is initiated by the electronic excitation of an organic molecule and the subsequent creation of a radical by either electron transfer to molecular oxygen, or by homolysis of the initial molecule. This process is usually inefficient due to poor reaction rates or high energy requirements (short UV wavelengths), and benefits from the presence of other oxidating species [33].
- UV/H_2O_2 (UV/Peroxide) Process – UV radiation at wavelengths around 253.7 nm promotes the homolytic breakdown of H_2O_2, generating hydroxyl radicals that then scavenge electron-rich species in solution. The new radicals formed as a result of this electrophilic attack, $RH\bullet$ (where R is an organic chain), can then be further oxidized by molecular oxygen to extend the chain of reactions, or polymerize to form R_n [34].
- UV/O_3 (Photolytic Ozonation) Process – dissolved ozone in an aqueous medium establishes a chemical equilibrium with H_2O_2 and O_2. These species react among themselves and with UV radiation at 254 nm to produce the hydroxyl ($\bullet OH$), hydroperoxyl ($HO_2\bullet$) and ozonide ($O_3^{\bullet -}$) radicals. Aqueous ozone, by itself, has a reduction potential of 2.07V and can attack organic molecules containing double or triple bonds [24].
- Photo-Fenton Process – the traditional Fenton process uses a ferrous (Fe^{2+}) salt in aqueous medium as a catalyst to the conversion of H_2O_2 into hydroxyl radicals [35]. Adding UV radiation to the process increases efficiency because it participates in the regeneration reactions of the catalyst (usually ferrioxalate, $Fe(C_2O_4)_3^{3-}$) and it also enables the photolytic decomposition of the iron-water complex to generate more hydroxyl radicals ($\bullet OH$). The wavelength range that can be used in this process is between 300 and 500 nm, making it attractive for applications intended to use natural light [36].

1.2.3. Photocatalysis through semiconductors

Semiconductors are the standard approach to heterogenous photocatalysis in AOPs, an alternative to the homogenous photocatalysis methods outlined in the previous section.

The operating principle for semiconductors is based on the energy band model. When multiatomic systems (such as molecules or crystalline lattices) are formed, molecular orbitals are created as a linear combination of the individual atomic orbitals of the atoms constituting the system (LCAO approach) [37]. The molecular orbitals are equal, in number, to the combined atomic orbitals, and each corresponds to a unique energy level. By increasing the number of atoms in the multiatomic system, the difference between individual energy levels decreases until a continuous band of energy is formed [38].

Crystalline solids can be classified using the energy band model, according to how their conduction and valence bands are positioned, as well as to how they are occupied with electrons. If a material's valence band overlaps its conduction band, or if it is only partially filled (Figure 1 (a) and (b), respectively), electrons can move freely along the empty band and conduction of electricity is possible. This is the case for metals, where the Fermi level is located within the valence band. If the valence band is fully occupied and does not overlap with the conduction band, the energy levels between the bands are said to be forbidden. The difference in energy between the valence band's highest occupied level and the conduction band's lowest permitted level is called the band gap (E_g). High band gaps ($> 4\ eV$) prevent valence electrons from escaping into the conduction band, making the material an insulator (Figure 1 (c)). Small band gaps allow valence electrons to be excited into the conduction band with a relatively low energy input, making the material a semiconductor. Commonly, semiconductors have $E_g > 3\ eV$ while materials with band gap between 3 and $4\ eV$ are classified as wide band gap semiconductors. The conduction band in semiconductors is usually not completely empty due to temperature effects [11] [15].

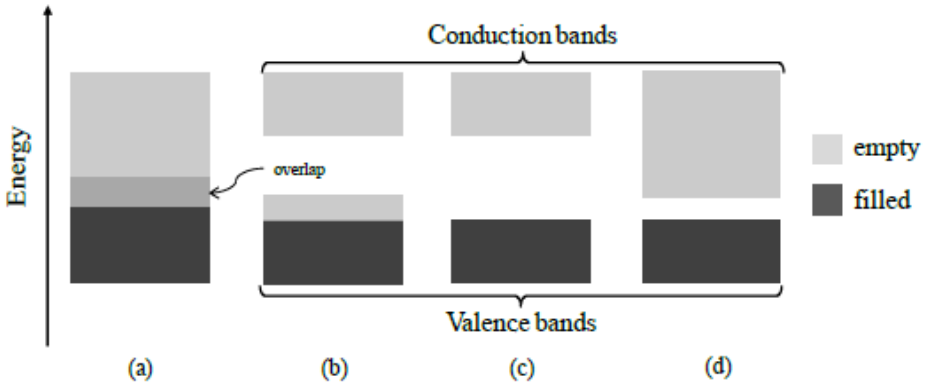

Figure 1 Simplified representation of the energy bands closest to the Fermi level at 0 K for conductors (a and b), insulators (c) and semiconductors (d) [15]

Within the context of AOPs, the intrinsic electronic structure of semiconductors is interesting because the promotion of valence electrons into the conduction band originates two excited charge carriers within the crystal lattice: an electron (e^-) that can move freely along the conduction band, and a positive vacancy known as a hole (h^+) that can move along the valence band (through movement of valence electrons towards the vacancy). The generation of charge carriers is

illustrated in Figure 2, where E_g, E_c, E_v and E_f are the band gap energy, conduction band energy, valence band energy and the Fermi energy level. The energy required to excite a valence electron to the conduction band is commonly supplied by absorption of a photon of sufficiently high energy (equal or greater than the band gap energy). Once the charge carriers reach the surface of the material within which they are generated, they can interact with adsorbed molecules to generate free radicals which will form the Reactive Oxygen Species in the medium. For instance, the percolating electron will react with molecular oxygen to form the superoxide radical ($O_2 + e^- \rightarrow O_2^{\bullet -}$) and electronic holes will react with water to form the hydroxyl radical ($H_2O + h^+ \rightarrow \bullet OH + H^+$) [9] [39]. More detail on the surface chemistry of select semiconductors will be provided in following sections.

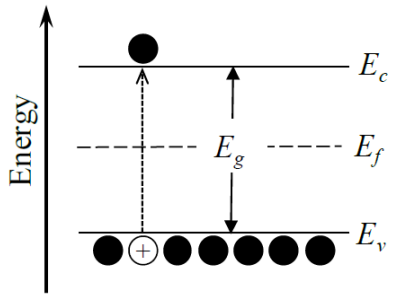

Figure 2 Excitation of an electron from the valence to conduction bands, creating an electron-hole charge carrier pair (e^- and h^+, respectively) [15]

1.2.4. Reactive Oxygen Species and the Hydroxyl Radical

The Reactive Oxygen Species used in Advanced Oxidation Processes are usually free radicals of stoichiometry O_x or HO_x, where $x = 1, 2, 3\ or\ 4$ [8]. The main species usually involved in AOPs, as well as their half-reactions and reduction potentials, are summarized in Table 1. Data for the fluoride radical-ion pair ($F \bullet / F^-$) was included for comparison.

Table 1 ROS commonly present in AOPs with the respective half-reactions and reduction potentials (against the standard hydrogen electrode) [40]

Reactive Oxygen Species	Redox Couple	E_0 (V)
$\boldsymbol{O_2}$	$O_2 \,/\, O_2^{\bullet -}$	-0.33
	$O_2(^1\Delta_g) \,/\, O_2^{\bullet -}$	0.65
$\boldsymbol{HO_2^{\bullet}}$	$HO_2^{\bullet} \,/\, HO_2^-$	0.79
$\boldsymbol{H_2O_2}$	$H_2O_2, H^+ \,/\, H_2O, \bullet OH$	0.80 [41]
	$H_2O_2, H^+ \,/\, 2H_2O$	1.77 [41]
$\boldsymbol{O_2^{\bullet -}}$	$O_2^{\bullet -}, 2H^+ \,/\, 2H_2O_2$	0.94
	$O_2^{\bullet -}, H^+ \,/\, HO_2^-$	1.00
$\boldsymbol{O_3}$	$O_3 \,/\, O_3^{\bullet -}$	$1.19 - 1.60$
	$O_3, H^+ \,/\, HO_3^{\bullet}$	1.80
	$O_3, H^+ \,/\, O_2, H_2O$	2.07
$\boldsymbol{\bullet OH}$	$\bullet OH \,/\, OH^-$	1.90
	$\bullet OH, H^+ \,/\, H_2O$	2.73
$\boldsymbol{F \bullet}$	$F \bullet / F^-$	3.60

Radical species possess an unpaired electron, which is generated by homolytic bond cleavages enabled by either thermal or photochemical processes. For the AOPs addressed in this work, a photochemical event is the *initiation step* by which radicals are formed. They trigger a chain of reactions with other species in the medium, generating new radicals (including organic ones) in what is called the *propagation step*. The *termination step* happens when two radicals combine to form a stable product, ending the chain reaction [42].

The hydroxyl radical ($\bullet OH$) is considered the primary oxidative species in AOPs [8], and the main product generated from the photocatalytic process on Fe-TiO_2 as it will be discussed later. As shown on Table 1, it also boasts one of the highest reduction potentials aside from fluoride, indicating that it is a powerful oxidizing agent. Its high reactivity indicates that the hydroxyl radical is non-selective and has a short half-life, leading to low steady-state concentrations in media that contains organic matter or other electron-rich compounds [43].

The oxidation of organic substrates by the hydroxyl radical can follow three main reaction pathways [24]: hydrogen abstraction (Equation 1), electrophilic addition (Equation 2) and electron transfer (Equation 3). The newly formed radicals then proceed to react with other species in solution. Such chain of reactions can originate intermediate radicals such as superoxide ($O_2^{\bullet -}$), hydroperoxyl ($HO_2^{\bullet}$) and organic peroxyl ($RO_2^{\bullet}$). Equation 4 shows how these species are formed and contribute to the propagation of the oxidation chain, illustrated by the partial oxidation of benzene [44].

$$\bullet OH + RH \rightarrow R\bullet + H_2O \qquad \text{Equation 1}$$

$$\bullet OH + PhX \rightarrow HOPhX\bullet \qquad \text{Equation 2}$$

$$\bullet OH + RX \rightarrow RX^{\bullet +} + OH^- \qquad \text{Equation 3}$$

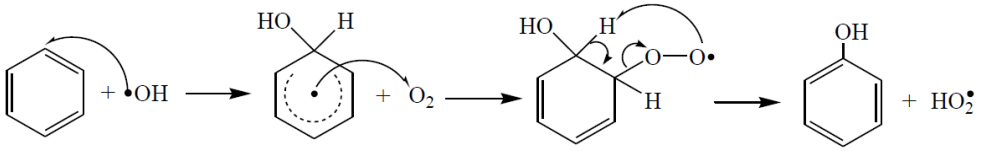

Equation 4

1.3. Titanium dioxide

Titanium dioxide (TiO_2) is a semiconductor widely used in the industry. It is traditionally used as an additive or component of paints, plastics, paper, ceramics, coated fabrics, textiles, and catalysts. Due to its superior optic, electric and surface qualities, around 95% of all titanium mined is consumed as titanium dioxide [45]. TiO_2 is often an important component in cutting-edge technologies such as thin-film devices (for instance, solar cells) [46], gas sensors at high temperatures [47] and bone-substitution structures for biological applications [48].

Several characteristics of TiO_2 make it a choice candidate for photocatalyst applications. It has an intrinsic bandgap around 3.03-3.20 eV (depending on the polymorph), efficiently absorbing wavelengths in the near-UV part of the spectrum, as well as somewhat into the visible range. It is

photo-stable, biocompatible in the usual range of particle sizes (0.2-0.4 μm [45]), relatively inert chemically, has an electronic band structure that is conducive to the generation of ROS, and is widely available [11].

1.3.1. Phases and structure

The most common polymorphs of titanium dioxide found in nature are rutile, anatase and brookite, where only the first two have a significant role in industrial applications. As shown in Figure 3, the lattice structure can be understood in terms of TiO_6 octahedrons with each Ti atom coordinating with six O atoms, and each O atom coordinating with three Ti atoms. The polymorphs differ in the distortion of each individual TiO_6 octahedron, as well as in how they are assembled. Table 2 provides more information on the lattice organization, as well as on macroscopic information such as density and band gap [49].

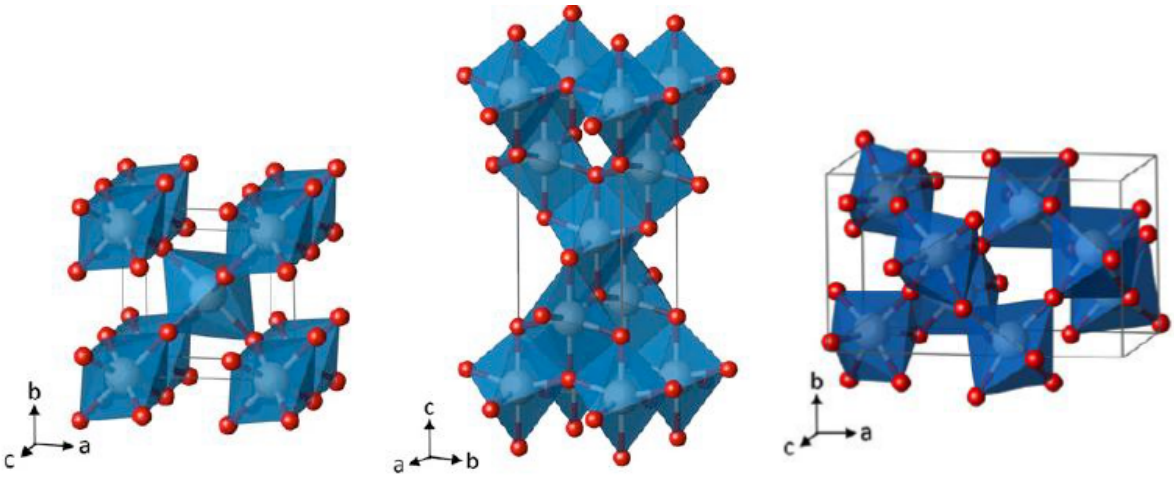

(a) (b) (c)

Figure 3 TiO_2 lattice assembly patterns for (a) rutile, (b) anatase and (c) brookite. The blue octahedrons represent the TiO_6 units, where white spheres are Ti atoms and red spheres are O atoms [49]

Table 2 Selected lattice and bulk parameters for the most common TiO_2 polymorphs [49] [50]

Polymorph	System	Specific mass (kg/m^3)	Lattice parameters (Å)	Band gap (eV)
Rutile	Tetragonal	4240	a = b = 4.5937 c = 2.9581	3.03
Anatase	Tetragonal	3830	a = b = 3.7842 c = 9.5146	3.20
Brookite	Rhombohedral	4170	a = 9.16 b = 5.43 c = 5.13	3.13

1.3.2. Photocatalytic activity

As described in section 1.2.3 above, TiO_2 can be used as a photocatalyst through the absorption of a photon of energy comparable to its band gap energy, which generates an excited electron in the conduction band and an electron vacancy (hole) in the valence band. These energetic species, referred to as *charge carriers*, are generated within the material's lattice and percolate to the interface between TiO_2 and reactive medium. There, the charge carriers react with species adsorbed on the particle's surface, generating ROS (such as the hydroxyl radical) which trigger radical reactions capable of degrading electron-rich organic pollutants. Figure 4 illustrates the phenomena resulting from the absorption of a photon by a TiO_2 particle.

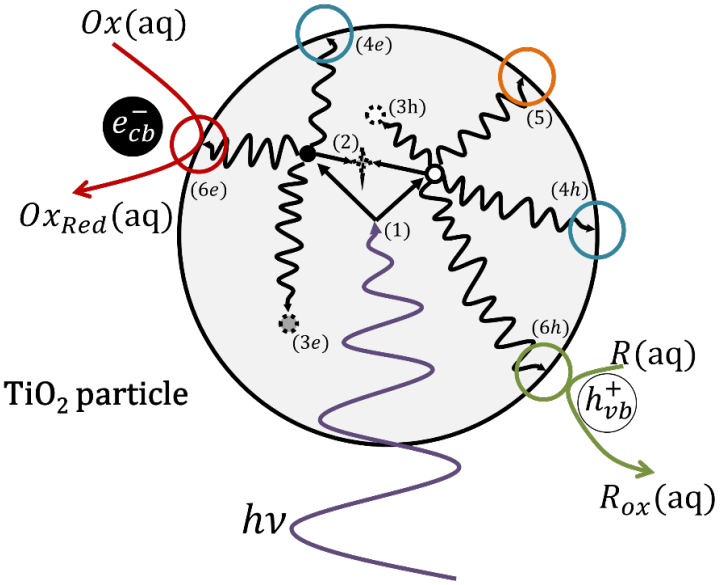

Figure 4 Photocatalytic phenomena triggered by photogeneration of charge carriers within the TiO_2 lattice (modified from Ramos, 2014 [15])

The main processes illustrated on Figure 4 can be summarized by the following equations [26] [51]:

(1) Generation of charge carriers:

$$TiO_2 \xrightarrow{h\upsilon} h^+_{vb} + e^-_{cb} \qquad \text{Equation 5}$$

(2) Recombination of charges:

$$h^+_{vb} + e^-_{cb} \rightarrow heat \qquad \text{Equation 6}$$

(3) Trapping of charge carriers in the bulk of the particle:

(h) $h^+_{vb} + Ti^{III} \rightarrow Ti^{IV}$ Equation 7

(e) $e^-_{cb} + Ti^{IV} \rightarrow Ti^{III}$ Equation 8

(4) Trapping of charge carriers on the surface of the particle:

(h) $h_{vb}^{+} + (Ti^{III}OH)_s \rightarrow (Ti^{IV}OH)_s$ Equation 9

(e) $e_{cb}^{-} + (Ti^{IV}OH)_s \rightarrow (Ti^{III}OH)_s$ Equation 10

(5) Cycle of oxidation mediated by the hydroxyl radical

$h_{vb}^{+} + (OH^{-})_s \rightarrow (\bullet OH)_s$ Equation 11

$(\bullet OH)_s + (\bullet OH)_s \rightarrow (H_2O_2)_s$ Equation 12

$(H_2O_2)_s + h_{vb}^{+} \rightarrow (HO_2^{\bullet})_s + H_{aq}^{+}$ Equation 13

$(HO_2^{\bullet})_s + h_{vb}^{+} \rightarrow (O_2)_{aq} + H_{aq}^{+}$ Equation 14

$(H_2O_2)_s + e_{cb}^{-} \rightarrow (\bullet OH)_s + (OH^{-})_s$ Equation 15

$(\bullet OH)_s + R_{aq} \rightarrow \bullet R_{aq} + (OH^{-})_s + H_{aq}^{+}$ Equation 16

(6) Cycle of oxidation/reduction of adsorbed species mediated by holes/electrons

(h) $(R)_{aq} \rightleftarrows (R)_{ads} + h_{vb}^{+} \rightarrow (R_{ox})_{ads} \rightleftarrows (R_{ox})_{aq}$ Equation 17

(e) $(Ox)_{aq} \rightleftarrows (Ox)_{ads} + e_{cb}^{-} \rightarrow (Ox_{red})_{ads} \rightleftarrows (Ox_{red})_{aq}$ Equation 18

The reactions represented by Equation 11 through Equation 18 show some of the possible degradation pathways triggered by electrons and holes reaching the surface of the photocatalyst particle. If organic species are adsorbed on the particle's surface, these compounds can be directly oxidized or reduced by holes or electrons (respectively) before being desorbed back into the medium, as illustrated by Equation 17 and Equation 18. Another pathway is mediated by hydroxyl groups bound to Ti atoms at the surface of the catalyst (titanol groups), reacting with organic species in the solution to create organic radicals (Equation 16) which can then extend the chain reaction through the mechanism outlined by Equation 4.

The reactions outlined above show how reactive oxygen species participate in the oxidation of organic molecules while remaining bound to the catalyst's surface. However, these oxidation processes are not limited to the immediate proximity of the catalyst particle, and oxygen radicals may desorb from the surface to oxidize other species in solution [9] [39]. In fact, adsorbed molecular oxygen (O_2) may undergo reduction by a conduction band electron (e_{cb}^{-}) to generate the superoxide radical ($O_2^{\bullet -}$) in solution, and the adsorbed hydroxyl ion (OH^{-}, either in protonated or deprotonated form) can undergo oxidation by a valence band hole (h_{vb}^{+}) to form a hydroxyl radical ($\bullet OH$) in solution. These radicals can then shift configurations in solution upon further interaction with other species/charge carriers or be incorporated into a step of an oxidation chain reaction such as the one outlined in Equation 4. Some of the changes the ROS may undergo are illustrated by the following equations (where steps involving transfer of charge carriers take place in the proximity of the catalyst's surface, otherwise in the aqueous medium):

$(O_2)_{ads} + e_{cb}^{-} \rightarrow (O_2^{\bullet -})_{aq}$ Equation 19

$O_2^{\bullet -} + H^{+} \rightarrow HO_2^{\bullet}$ Equation 20

$HO_2^{\bullet} + H^{+} + e_{cb}^{-} \rightarrow H_2O_2$ Equation 21

$H_2O_2 + e_{cb}^{-} \rightarrow \bullet OH + OH^{-}$ Equation 22

$(OH^{-})_{ads} + h_{vb}^{+} \rightarrow (\bullet OH)_{aq}$ Equation 23

The optical properties, and therefore photocatalytic activity, of TiO_2 is dependent on the crystal polymorph. As shown in Figure 5, the crystal structure of anatase, rutile and brookite generate distinct absorbance/reflectance spectra, from which different values for the band gap energy can be calculated. The lower calculated band gap energy for rutile could suggest that this polymorph is more efficient in terms of photocatalytic activity as it requires photons carrying less energy to be activated, with applications using natural light ($3.0\ eV$ translates to a wavelength of roughly $413\ nm$, well into the visible spectrum). However, rutile is observed to be significantly less efficient in oxidizing organics than anatase or mixed-phase (anatase/rutile) TiO_2. Other factors such as particle size, lattice defects, electron-hole recombination rates, surface area and state of surface (hydroxylation ratios, presence of a contamination layer, etc.) have an important role in determining the final photocatalytic activity. In particular, the high temperatures necessary to crystallize the rutile phase might be responsible for the de-hydroxylation of the catalyst's surface, hindering its photocatalytic activity [52] [53].

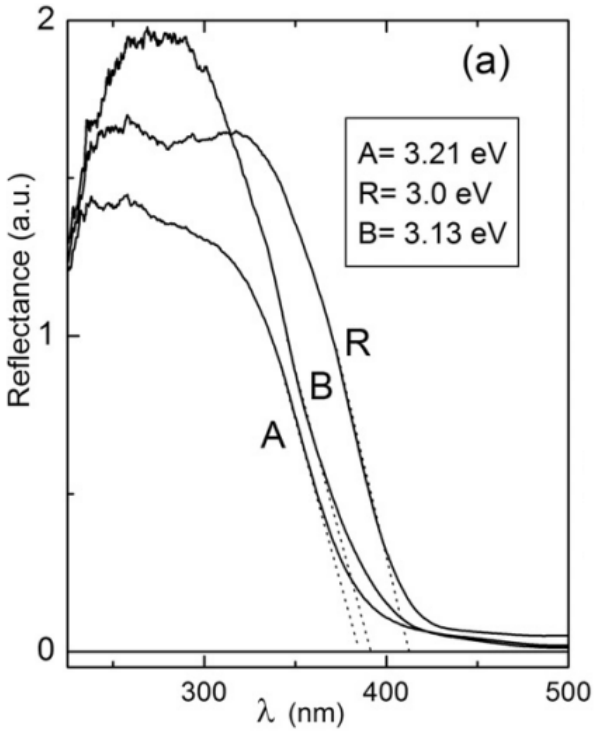

Figure 5 UV-visible reflectance spectrum of phase-pure titania nanomaterials, where A, R and B correspond to anatase, rutile and brookite respectively. The inset shows the band gap energy calculated for indirect transitions [54]

Macroscopically, the kinetics of photodegradation of organic pollutants follows the Langmuir-Hinshelwood model, as most heterogeneous catalytic processes do [55] [56]. The model assumes that the rate-determining step of the process is given by the oxidation surface reaction involving the adsorbed pollutant molecules, at maximum coverage of the catalyst particle [57] [58]. Indeed, it has been reported that the charge transfer step across the interface between catalyst and reaction medium is relatively slow (hundreds of nanoseconds to the order of microseconds) when compared to other processes taking place in the bulk of the catalyst particle such as charge carrier generation and trapping [55]. The reaction rate is given by Equation 24:

$$r = -\frac{dC}{dt} = \frac{k_r K_{ad} C}{1 + K_{ad} C} \quad \text{Equation 24}$$

where r is the rate of photo-oxidation, C is the concentration of the organic pollutant in question, t is the reaction time elapsed (after an adsorption equilibrium in the dark has been established), k_r is the rate constant of the degradation reaction and K_{ad} is the adsorption equilibrium constant between the catalyst and pollutant. In dilute systems ($C \ll 1$), the denominator on the right-hand side of Equation 24 is approximately 1 and the reaction kinetics can be taken as pseudo-first order. After integrating, the evolving pollutant concentration is given by Equation 25:

$$ln\left(\frac{C_0}{C}\right) = k_r K_{ad} t = k_{app} t \quad \text{Equation 25}$$

where C_0 is the initial concentration of pollutant at $t = 0$ and k_{app} is the apparent first-order reaction rate constant. Under the same dilution conditions and catalyst concentration, the initial degradation rate can be estimated in terms of the apparent rate constant and initial concentration:

$$r_0 = k_{app} C_0 \quad \text{Equation 26}$$

1.3.3. Doping

Despite TiO_2's attractive properties for its use in wastewater treatment applications, there are some challenges involved in optimizing process efficiency. The high charge carrier mobility within the crystal lattice enables an elevated charge carrier recombination rate (illustrated by Equation 6) which limits the number of electrons/holes reaching the catalyst's surface. Another challenge is titania's large band gap energy ($\sim 3.2\ eV$ for anatase), which allows the generation of highly energetic ROS but on the other hand requires radiation in the near-UV range to be photoactivated. UV accounts for only a fraction ($3 \sim 5\%$) of the natural light wavelength spectrum, and as such artificial light is required to photoactivate TiO_2. Generating artificial UV is expensive and, combined with its safety requirements, often amount to a significant portion of the overall operation costs [39] [59] [60].

Doping is an attractive solution to remedy the issues outlined above. Several types of doping agents, such as nitrogen interstitial impurities [61] and carbon-based materials [59], have been studied. However, metallic dopants, when incorporated into the semiconductor's lattice in small quantities, address these issues and improve the overall photocatalytic efficiency due to the following effects:

- the interaction between the d orbital of the dopant and the $3d$ orbital of Ti creates an intra-band energy level (between TiO_2's valence and conduction band) just below pure titania's conduction band, enabling electronic transitions to occur upon absorption of longer wavelengths. Consequently, the material's absorption spectrum is red-shifted and charge carriers may be generated using less energetic photons [39] [62].
- metallic atoms allowing several oxidation states can act as temporary traps for electrons and holes, reducing the recombination rates and therefore increasing the number of charge carriers reaching the surface to trigger the charge transfer reactions shown in Section 1.3.2 [5] [63].

Noble metals such as Pt, Au and Pd have been shown to greatly increase the photocatalytic activity of TiO_2, but the elevated cost of those elements is prohibitive to their large-scale adoption as doping agents [64] [65]. Transition metals are an efficient, more affordable alternative. The effects of several transition metals (such as Cr, Cu, Fe, Zn, Ag, W, V, Mn, Mo and Ni, among others) within the TiO_2 lattice have been studied [5] [62] [66].

Iron (III) is an excellent candidate as a dopant. It has been reported to reduce the band gap energy from $3.08\ eV$ (equivalent to $\sim 403\ nm$) in mixed-phase TiO_2 to $2.03\ eV$ (equivalent to $\sim 611\ nm$) with as little as 0.3% in weight of iron impurities [5]. These values match predictive studies reporting the HOMO (highest occupied molecular orbital) energy level of the combined Ti^{4+}/Fe^{3+} band structure to be $0.5 \sim 0.8\ eV$ above the conduction band, and the LUMO (lowest unoccupied molecular orbital) to be $0.7\ eV$ below the conduction band [67]. As well, iron (III) has a similar atomic radius (0.68 Å) to titanium (IV) (0.64 Å), indicating that it might occupy substitution sites in the TiO_2 lattice. Indeed, XRD studies show no disruption of the pure-anatase diffraction peaks and no presence of Fe_xTiO_y peaks up to an atomic concentration of 2.5% in iron impurities [68]. Moreover, the different oxidation states of iron atoms enable them to act as charge carrier traps, as illustrated by the following equations where all species are contained within the catalyst lattice:

$$TiO_2 \xrightarrow{h\upsilon} h_{vb}^{+} + e_{cb}^{-} \quad \text{Equation 27}$$

$$Ti^{4+} + e_{cb}^{-} \rightarrow Ti^{3+} \quad \text{Equation 28}$$

$$O^{2-} + h_{vb}^{+} \rightarrow O^{-} \quad \text{Equation 29}$$

$$Fe^{3+} + Ti^{3+} \rightarrow Fe^{2+} + Ti^{4+} \quad \text{Equation 30}$$

$$Fe^{3+} + O^{-} \rightarrow Fe^{4+} + O^{2-} \quad \text{Equation 31}$$

According to crystal field theory, both Fe^{2+} and Fe^{4+} ions are less stable than Fe^{3+} due to the latter having a half-filled d orbital (d^5). As such, the electrons and holes trapped within the iron sites are expected to be eventually released. Charges trapped in impurities deep within the lattice will continue their path to the surface (Equation 32 and Equation 33), while charges trapped sufficiently close to the interface might participate in the direct oxidation/reduction of chemical species adsorbed on the surface (Equation 34 and Equation 35). Iron atoms act, then, as charge traps that decrease the electron-hole recombination rate and ultimately increase the overall photocatalytic activity. That holds true if the iron impurities are present in small quantities, otherwise they may become recombination centers for charge carriers and significantly reduce photocatalytic activity [68].

$$Fe^{2+} + Ti^{4+} \rightarrow Fe^{3+} + Ti^{3+} \quad \text{Equation 32}$$

$$Fe^{4+} + O^{2-} \rightarrow Fe^{3+} + O^{-} \quad \text{Equation 33}$$

$$(Fe^{2+})_s + (O_2)_{ads} \rightarrow (Fe^{3+})_s + (O_2^{\bullet -})_{ads} \quad \text{Equation 34}$$

$$(Fe^{4+})_s + (OH^{-})_{ads} \rightarrow (Fe^{3+})_s + (\bullet OH)_{ads} \quad \text{Equation 35}$$

Despite the desirable properties described above, iron (III) has traditionally been reported to be a poor dopant for TiO_2.

Figure 6 shows the results of a study carried by Kerkez-Kuyumcu et al. (2015) [5], where the photocatalytic activity of TiO_2 doped with several transition metals at 0.3wt% was measured by means of degradation of methyl orange. As can be seen in the figure, Fe-TiO_2 performed significantly more poorly than other combinations, including pure titania, when traditional fabrication methods were used to synthesize the catalyst.

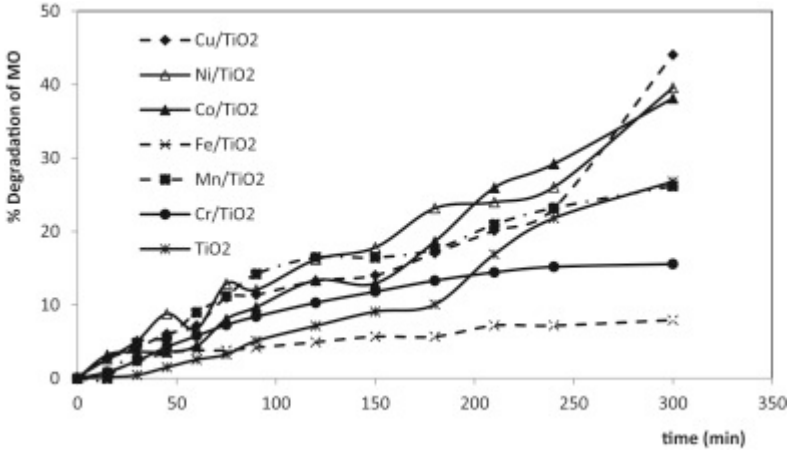

Figure 6 Comparison between the photocatalytic activity of TiO_2 doped with several transition metals, in terms of % of degradation of methyl orange over time. The catalysts were fabricated using usual synthetic methods [5]

A previous study by this research group [20] has demonstrated that the usual fabrication protocols for Fe-TiO_2, such as sol-gel methods, produce an amorphous iron oxide layer covering the surface of the catalyst particles. This iron oxide contamination layer acts as a barrier between the active surface of the crystalline lattice and the reaction medium, preventing the interfacial charge transfer reactions. It has been shown that adding an acid-wash step to the end of the sol-gel fabrication protocol removes said contamination layer and exposes the catalyst's active surface. This increases the apparent reaction rate constant (from Equation 25) over thirteen times, restoring iron's status as an attractive doping agent.

1.3.4. Toxicity and biocompatibility

Titanium dioxide has traditionally been classified as a bio-inert material with low toxicity for human health and for the environment. This has led regular-sized TiO_2 particles (that is, those of characteristic dimension $> 100\ nm$) to be extensively employed in several segments of industry, including foods and cosmetics [69]. Titania's excellent biocompatibility has also been thoroughly studied for in vitro cell studies [70], bone grafts and implants [71] and prostheses [72]. Human exposure to TiO_2, whether intended or unknowingly, is unavoidable and raises concern about the possible harmful effects of titania nanoparticles, which have not been studied as thoroughly as non-nanosized particles. Exposure to TiO_2 nanoparticles may happen if they are present as an additive in common commercial products such as toothpaste, sunscreen and paint [73], or even through corrosion of metallic Ti implants which may release nanosized wear debris [74].

Nanoparticles raise concern due to their unusual physicochemical properties, stemming from the incredibly high surface-to volume ratio they exhibit. Those properties, which are not present in the conventional bulk material counterparts, has led some researchers to treat them as an intermediate state of matter between molecules and bulk materials. Metal-based nanoparticles in particular often exhibit increased toxicity as the characteristic size decreases, regardless of whether the corresponding bulk material is inert [75]. For TiO2 and other semiconductor nanoparticles, the main mechanism through which toxicity is triggered is the generation of ROS,

inducing oxidative stress, inflammation, genotoxicity, metabolic changes and possibly carcinogenesis [69].

Early studies tried to verify whether the toxicity of TiO_2 nanoparticles could be attributed to crystallinity or size. It was found that pure anatase TiO_2 induced cell necrosis regardless of particle size, while rutile TiO_2 initiated cell apoptosis (programmed death) through formation of ROS, which is size dependent. That confirms the increased toxicity of anatase when compared to rutile [76]. In-vitro studies have shown that nanoparticle uptake through the cell membrane is dose-, size- and shape-dependent, and that spherical, mixed-phase particles have the highest uptake [77].

Nanoparticles can enter the human body via ingestion, the airways, or the skin [78]. Oral uptake has been shown to allow the particles to travel within the bloodstream and accumulate in different organs in mice [79]. The inhalation of ultrafine particles has been shown to cause oxidative stress in the lungs, related to their high surface area [80]. Nanoparticles can also clear the air-blood barrier in the lungs and reach the bloodstream, gaining access to other organs [81]. Studies using live pigs and mice have shown that TiO_2 nanoparticles penetrate the skin and reach several organs (mainly spleen, heart and liver) after topic sub-chronic exposure [82].

The negative effects of chronic exposure to TiO_2 nanoparticles on humans can be predicted to some extent from in-vitro and in-vivo studies using mammalian test subjects. Among the expected adverse consequences are: protein misfolding and fibrillation [83], chronic inflammation in the lungs and other organs [84], high-risk pregnancies [85] [86], damage of liver function [87], chromosomal aberrations (in high doses) [87] and neurodegeneration [88].

1.3.5. Fabrication methods

Titanium dioxide can be fabricated through a miscellanea of processes depending on the properties desired for the final product, such as particle size, morphology, crystallinity, purity, doping needs, among others. Such processes can be split into gas phase methods and solution routes [50].

Gas phase methods are usually employed when TiO_2 must be synthesized in the form of thin films on a substrate, which can then be collected as a powder if a method to retrieve the particles is employed. Common gas phase methods are chemical vapour deposition (CVD) [89], physical vapour deposition (PVD) [90], spray pyrolysis deposition (SPD) [91] [92], sputtering [93], molecular beam epitaxy [94], ion implantation [95] and dynamic ion beam mixing [96]. They differ in reactivity of precursors in the gas phase, method for vaporizing the precursors, deposition being inertia- or diffusion-dominant, operation temperature and pressure, source of gas-phase precursors, among other factors.

Solution routes can be more convenient to achieve than gas phase methods in terms of equipment required, aside from the advantage of providing better control over the stoichiometry of the final product, producing homogenous materials, allowing controlled formation of complex shapes and preparation of composite materials. Disadvantages occasionally include the need for expensive precursors, long fabrication times and presence of carbon impurities in the final products [50]. Some of the most common solution routes are precipitation of TiO_2 from $TiCl_3$/$TiCl_4$ solutions through alkalinization [97], hydro/solvothermal methods where elevated temperatures and

pressures are employed [98] [99], microemulsions for synthesis of nanoparticles [100], combustion synthesis producing high surface area crystalline particles [101], electrochemical synthesis [102] and sol-gel methods. The latter, in particular, are of special interest due to its simplicity and versatility in terms of control over the composition and morphology of the final product.

Sol-gel methods can be based on non-alkoxide or alkoxide routes. Non-alkoxide routes use inorganic titanium salts as precursors, such as $TiCl_4$, $Ti(SO_4)_2$ and others. Inorganic precursors may be more economical than alkoxide precursors but might also require more carefully controlled reactive medium conditions (such as pH and the concentration of all species involved, including "control agents"), high/low temperatures and longer reaction times ("aging" of the sol/gel solution) [103]. The alkoxide route is more often employed to fabricate TiO_2 and uses organometallic compounds as titanium precursors. It involves at least the following steps: hydrolysis, polycondensation, drying and thermal decomposition/calcination [104]. The alkoxide route will be detailed further as it was employed in this study to synthesize anatase TiO_2.

Titanium sources for the alkoxide route follow the stoichiometry $Ti(OR)_n$. The most usual sources are titanium tetra-ethoxide ($Ti(OEt)_4$), tetra-iso-propoxide ($Ti(OiPr)_4$, also commercially known as TTIP) and tetra-n-butoxide ($Ti(OnBu)_4$) [50]. The alkoxide precursors undergo hydrolysis, producing titanium hydroxides and alcohols according to Equation 36:

$$Ti(OR)_n + m\,H_2O \rightarrow Ti(OH)_m(OR)_{n-m} + m\,ROH \qquad \text{Equation 36}$$

where the substitution of alkoxyl ligands $(-OR)$ by hydroxyl groups $(-OH)$ might take place in successive steps. In the polycondensation step, the $M-OH$ and $M-OR$ bonds can react to form $M-O-M$ bond as follows:

$$Ti-OH + HO-Ti \rightarrow Ti-O-Ti + H_2O \qquad \text{Equation 37}$$

$$Ti-OR + HO-Ti \rightarrow Ti-O-Ti + ROH \qquad \text{Equation 38}$$

Several parameters, such as pH, temperature, reaction time and additives, can be adjusted during these steps to control morphology and crystallinity of the final product. It is usually good practice to use conditions that separate the hydrolysis from the condensation steps, in order to better control the evolution of the microstructure. For instance, the addition of coordination agents such as carboxylate or β-diketonate ligands provide control over particle and pore morphology as polycondensation takes place. Surfactants and block co-polymers can also be employed to yield mesoporous structures. Another strategy is to regulate the pH of the reaction medium to control crystallinity. Acid catalysis accelerates hydrolysis and yields fully crystalline powders resulting from a fully hydrolyzed precursor, while alkaline catalysis promotes early condensation which forms amorphous powders containing unhydrolyzed ligands. It is also during the hydrolysis and condensation steps that inorganic salts are added to the reaction medium to be incorporated into the final product. At the right ratios, the added metallic cations act as doping agents and can increase TiO_2's photocatalytic activity as described in Section 1.3.3 [50].

Following the hydrolysis and polycondensation steps, a thermal treatment (often referred to as "calcination") is used to remove water and the organic residues in the final product, as well as to

crystallize the TiO_2 powder as either anatase or rutile. The quality of the catalyst is sensitive to the calcination process, as it affects the phase structure of the particles (and hence the band structure). Furthermore, excessively high temperatures and long treatment times are usually not desired as calcination is bound to cause a reduction of the surface area due to crystal growth and sintering, besides the loss of surface $(-OH)$ groups which are essential to charge transfer reactions upon photocatalysis. Calcination temperatures are usually between 450°C and 600°C, but formation of both anatase and rutile outside of this range has been reported. Anatase can crystallize at temperatures as low as 250°C, while the rutile phase will start to form above 600°C [50] [105].

1.4. Electron microscopes and spectrometry techniques

Electron microscopes were initially developed to overcome the limitations in resolution imposed by the use of visible light in traditional light microscopes. The smallest distance δ that can be resolved, according to the classic Rayleigh criterion, is:

$$\delta = \frac{0.61\lambda}{\mu \sin\beta} \qquad \text{Equation 39}$$

where λ is the wavelength of light, μ is the refractive index of the medium and β is the semi-angle of collection of the lens. For visible light microscopes, the maximum theoretical resolution is about 300 nm.

With the development of quantum physics and the discovery of the electron's wave-particle duality, it has been found that the electron has a wavelength that depends on its kinetic energy. The expression for the wavelength of an electron accelerated through a potential drop is given by Equation 40, which includes relativistic corrections since an acceleration voltage of 100 kV (easily achievable in most modern TEMs) imparts on the electron a speed of around $0.5c$. In Equation 40, λ is the electron's wavelength, h is Planck's constant, m_0 is the electron's rest mass, e is the electron's fundamental charge, V is the microscope's acceleration voltage and c is the speed of light.

$$\lambda = \frac{h}{\left[2m_0 eV\left(1 + \frac{eV}{2m_0 c^2}\right)\right]^{1/2}} \qquad \text{Equation 40}$$

The resulting wavelength for a 100 keV electron is 3.70 pm, clearly allowing a much greater resolution than visible light. A combination of high acceleration voltages and corrections to spherical- and chromatic-aberrations has allowed modern electron microscopes to achieve resolutions well below $1\ \text{Å}$ [106].

The interaction between an accelerated electron beam with matter in a sample gives off a range of signals that can be used for imaging, crystallographic analysis, compositional analysis, among others. Figure 7 illustrates some of the signals generated when a high-energy electron beam traverses a thin specimen. The specimen shown in the Figure is thin enough to allow *transmission* of the electron beam, which is by no means always the case. Among these signals, secondary electrons (SE), characteristic X-rays, the direct beam and (in)elastically scattered electrons were of particular interest for the analyses carried in this work.

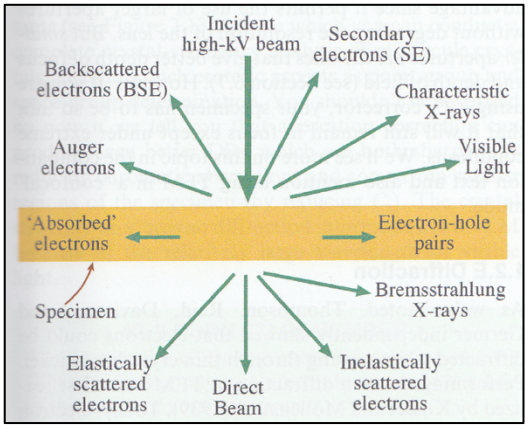

Figure 7 Several types of signals are generated upon the interaction of the accelerated electron beam with matter in the sample. A thin specimen is represented here (in yellow), allowing transmission of the direct beam through the material. Taken from [106].

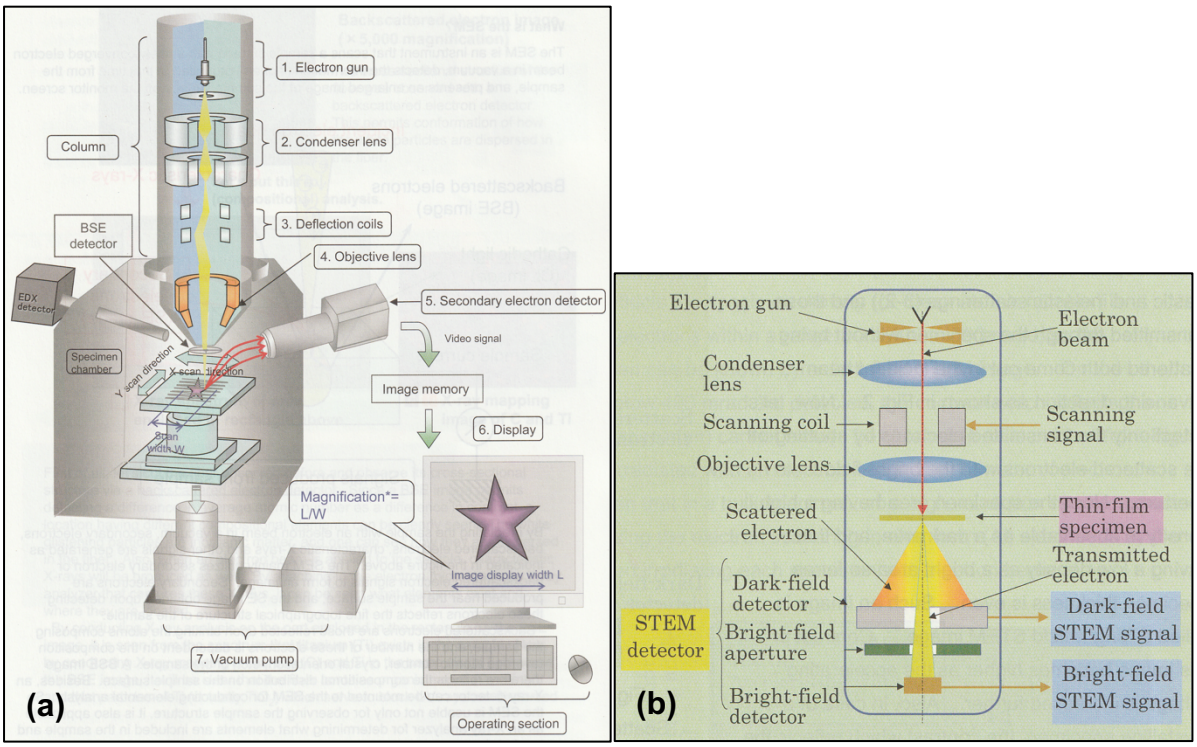

Figure 8 Usual setup for a (a) scanning electron microscope and (b) scanning-transmission electron microscope. Taken from [107].

Some of the most usual electron microscope configurations are the *Scanning Electron Microscope* (SEM, shown in Figure 8a), *Scanning-Transmission Electron Microscope* (STEM, shown in Figure 8b) and *Transmission Electron Microscope* (TEM). Any electron microscope is equipped with an electron gun (operating either by thermionic or field emission) and with a set of electromagnetic lenses that are able to manipulate the electron beam, making it coherent. As it can be seen in Figure 8a, a scanning electron microscope uses deflection coils to scan the sample with the electron probe (that is, the focus point of the electron beam), generating a signal (usually secondary or backscattered electrons) whose intensity is used to construct an image digitally. The

SEM may also be equipped with an X-ray detector, as shown in the Figure, which may be used to obtain compositional information of the sample. Due to the fact that scanning electron microscopy is usually used to reveal surface featured of a sample, the specimen is not usually required to be thin.

Figure 8b shows how specimen information can be obtained in a STEM system. The transmitted beam intensity is detected by either a Bright-Field or Dark-Field detector, depending on the scattering angle, after traversing the thin specimen. Deflection coils are used to move the electron probe over the sample, scanning the specimen and constructing an image where the scattering contrast provides valuable information about morphology, crystallinity and composition of the sample. A TEM system, not shown in the Figure, operates by condensing the emitted electrons into a parallel beam of variable spot size. The parallel beam traverses the sample and is preferentially diffracted off atomic planes in the sample, at angles defined by Bragg's law (Equation 41). A transmission image can be obtained by using an objective lens to recombine the diffracted beams, which are then projected onto a CCD (Charge Coupled Device) camera (TEM imaging mode). Diffraction images are produced by projecting the diffraction pattern formed at the back focal plane of the objective lens onto the CCD camera (TEM diffraction mode) [106].

$$n\lambda = 2d \sin 2\theta \qquad \text{Equation 41}$$

The diffraction pattern (DPs) is a powerful tool to characterize specimens in terms of composition and structure. As it will be explained further in Section 3.3.3, DPs contain information about the specimen's *reciprocal lattice*, which reveals data such as crystallographic orientations, zone axes and interplanar spacings.

Electron microscopes can be equipped with an array of detectors that make them extremely versatile for different types of analyses. It has been mentioned above that SEMs are often equipped with X-ray detectors that enable EDX compositional studies. EDX is an analysis method pertaining to the *spectroscopy* class of techniques. That is, some sort of signal emerging from the specimen is collected and classified according to certain criteria (photon wavelength, in the case of EDX) to generate a *spectrum*, from which information can be inferred. Two spectroscopic techniques were employed over the course of this work: Energy-Dispersive X-ray Spectrometry and Electron Energy-Loss Spectrometry. The details of these techniques will be further discussed below.

1.4.1. Energy Dispersive X-Ray analysis (EDX)

Energy Dispersion X-Ray analysis (EDX), also often named X-Ray Energy-Dispersive Spectrometry (XEDS), is a compositional analysis technique by which characteristic X-rays generated within a sample are used to identify and quantify the elements present in the specimen. The emmited X-rays are element specific and are generated when the incident electron beam ejects an electron from one of the atom's inner shells. A cascade of internal electronic transitions ensue to fill the lower-energy core electron vacancy, emmiting X-rays of wavelength equivalent to the energy difference of the electronic states involved in each transition [107]. This process is illustrated in Figure 9a. The different types of X-rays that a given atom can generate, depending on the electronic transition triggered by the ionization event, are illustrated in Figure 9b.

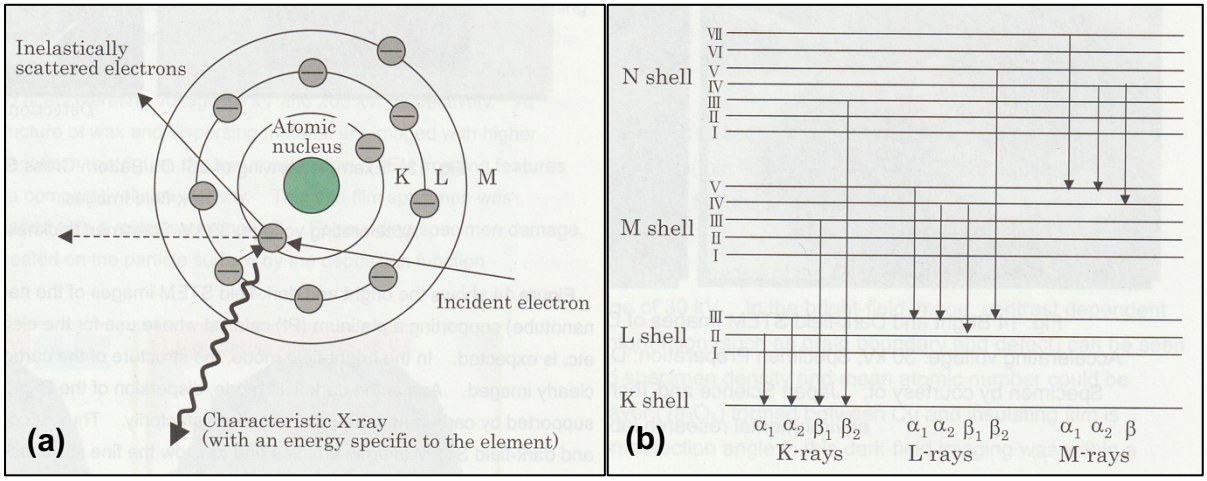

Figure 9 Mechanism through which characteristic X-rays are generated (a) and some of the possible types of electronic transitions (b). Taken from [107].

An EDX spectrum contains the signal from two types of X-rays. The element-specific characteristic X-rays, described above, appear as sharp peaks (lines, ideally) centered at the energy value for the electronic transition they represent. There is also a background radiation signal often called *bremsstrahlung* radiation, or "braking radiation". This type of X-rays originates from the inelastic interaction of the electron beam with the Coulomb field of the nucleus of the atoms in the sample. The electrons may lose any amount of energy, depending on the strength of the inelastic interaction with the specimen, which results in the emission of a continuous radiation background up to the electron beam energy. The bremsstrahlung background is assymetrical (skewed towards the low energy range depending on the specimen's average Z) and strongly forward-scattered. The final EDX spectrum is composed, then, of Gaussian-shaped elemental peaks superimposed on a continuous inelastic scattering background whose peak position depends on the composition of the specimen [106]. Figure 10 illustrates this by highlighting the portions of an EDX spectrum corresponding to characteristic and bremsstrahlung X-rays.

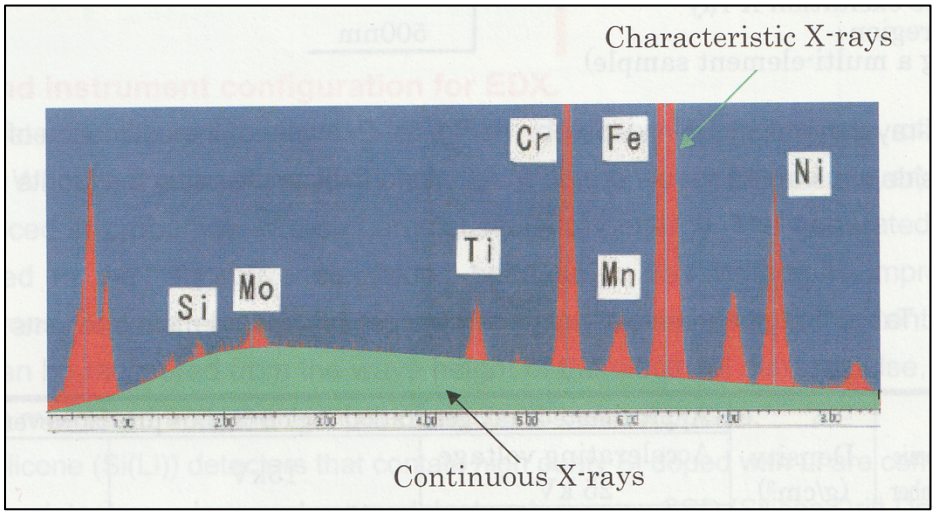

Figure 10 EDX spectrum of a stainless steel sample, where the intensities generated from characteristic X-rays and from bremsstrahlung radiation are indicated. Taken from [107].

Element quantification based on characteristic X-ray emissions is done by measuring the X-ray intensity emerging from the specimen and then comparing it to the intensity emerging from a standard of known composition. The final value must then undergo a *ZAF correction*, termed so because the X-ray emission ratio (a combined effect of the probability of excitation and the fluorescence yield) depends on the atomic Z number (Z), the absorption (A), and the fluorescence (F) of X-rays within the specimen. Having a thin specimen greatly enhances quantification by EDX, since the absorption and fluorescence effects within the sample are minimized and can be ignored ("thin-foil criterion"). In that case, the elemental ratios are proportional to the X-ray intensities emerging from the sample, weighted by a factor related to the atomic-number correction factor. More details on how to quantify the results of X-ray spectra can be found in the Williams&Carter textbook [106], which contains a comprehensive description of different methods and assumptions.

1.4.2. Electron Energy Loss Spectrometry (EELS)

According to Williams and Carter [106], EELS is defined as the "analysis of the energy distribution of electrons that have come through the specimen". This technique interprets the energy-loss events within the sample (usually inelastic electron-electron collisions) to infer information about the chemistry and electronic structure of the sample's atoms. Some of the sample characteristics that may be unveiled using EELS include: bonding/valence state, atomic structure, composition, dielectric response, free-electron density, band gap and specimen thickness. EELS analysis complements EDX since it is able to detect light elements more accurately, has better spatial resolution an analytical sensitivity, and it provides more information than just element identification.

An EELS spectrum is usually subdivided into low-loss and high-loss regions. Inelastic interactions in the low-loss region are mainly phonon excitations (in the order of 0.02 eV, so at times indistinguishable from the zero-loss peak), inter/intra-band transitions (2-20 eV) and plasmon interactions (5-30 eV). Losses in this region usually correspond to interactions with the weakly bound conduction and valence electrons, which can provide information about the electronic properties of the specimen. The transition to the high-loss region of the spectrum is usually taken to be around 50 eV, as losses above this threshold are dominated by the ionization of inner-shell electrons. The ionization loss signal in the EELS spectrum is called an edge and allows elemental quantification. Since this compositional analysis technique relies on high-energy electrons that interacted with the sample, and not on the emission of X-rays or Auger electrons, element quantification through EELS is not hindered by the fluorescence yield limitations that restrict light element analysis using EDX. The zero loss peak is a feature present in virtually all EELS spectra, corresponding to electrons that have retained the original beam energy due to mainly elastic- and forward-scattering (electron-nucleus interactions).

Elemental identification in EELS is done through the analysis of partial ionization events in the high-loss region of the spectrum. The ionization of a given element occurs upon the transfer of a certain critical ionication energy E_C, specific for a given core-shell electron, from the electron beam. However, the ionization event can occur upon energy transfers $\varepsilon \geq E_C$, with decreasing probability as the energy loss increases. This results in the ionization events appearing in the spectrum not as Gaussian peaks, like in EDX, but as triangular-shaped *ionization edges*. Figure 11a illustrates the triangular, saw-tooth shape of an idealized hydrogenic edge. In actual

specimens, one verifies that the ionization edges rise from an exponentially-decreasing plural-scattering background, then slowly decrease in intensity back towards the background. This is shown in Figure 11b.

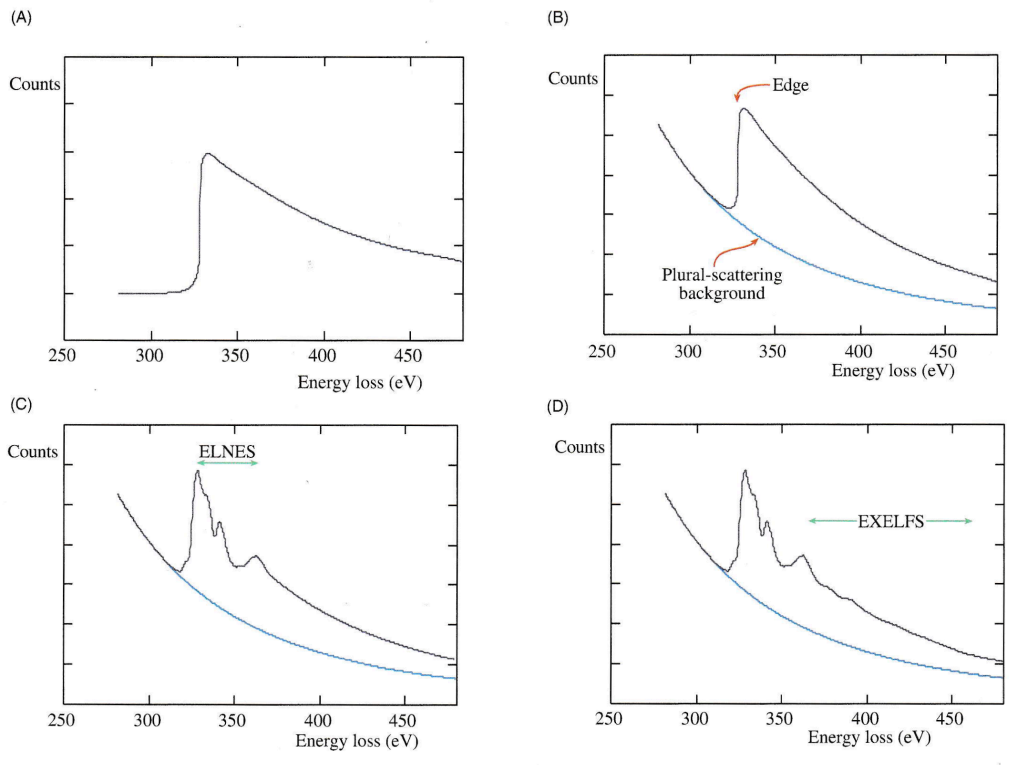

Figure 11 Examples of EELS spectra of (a) an idealized hydrogenic edge, (b) an hydrogenic edge superimposed on the plural inelastic scattering, (c) the ELNES fine structure and (d) the EXELFS fine structure. Adapted from [106]

There are yet other effects arising from not dealing with isolated atoms, which would produce a clean edge such as the one shown in Figure 11a. Bonding effects can generate a fine, oscillating structure extending up to 50 eV from the ionization edge onset. This feature is termed *Energy-Loss Near-Edge Structure* (ELNES), and is illustrated in Figure 11c. Above 50 eV after the edge onset, one might still detect small oscillations in intensity arising from diffraction effects off the atoms surrounding the ionized atom. This kind of structure, illustrated in Figure 11d, is called *Extended Energy-Loss Fine Structure* (EXELFS). Another artifact often present in EELS spectra from thick specimens is plasmon peaks following the ionization edge onset. All of these effects must be taken into account when interpreting the results of an EELS analysis.

1.5. Structure of the thesis

Chapter 1 opens this work with the motivation for the studies realized herein, followed by a literature review containing the necessary theoretical background to guide the research and to interpret the results. The original contributions of this thesis to the field of semiconductor photocatalysis and, more broadly, materials sciences, are also listed in this chapter.

Chapter 2 explores the particle size distribution of the novel Fe-TiO_2 photocatalyst using scanning transmission microscopy, elaborating on how such distribution affects its catalytic performance and commenting on the possible health hazards stemming from the presence of nano-sized particles among the catalyst. Suggestions for improvements to the fabrication protocol, addressing both catalytic efficiency and nanoparticle hazard, are provided.

Chapter 3 elucidates the inner structure of the Fe-TiO_2 photocatalyst, focusing on the nanosized monocrystals (crystallites) that constitute the polycrystalline catalyst particle and on the regions between crystallites. To that end, a thin specimen is fabricated and subsequently analyzed using transmission and scanning-transmission electron microscopy techniques. Morphology, crystallinity, and composition are investigated. The analyses provide insights concerning crystal growth and dopant segregation during synthesis, as well as the microstructure of the photocatalyst.

Chapter 4 summarizes the findings of the studies carried throughout this work and restates their importance for the continuity of research and development of real-world applications of Fe-TiO_2 as a photocatalyst, especially in the field of water treatment. It also outlines the direction future research must follow in order to answer questions that could not be addressed in these studies, or that arose from the result of this work.

1.6. Novel aspects in this work

The discovery of the iron oxide contamination layer on the surface of iron-doped anatase titania photocatalyst particles, and the subsequent development of a method to remove this barrier, could represent a significant advancement in the field of photocatalysis and wastewater treatment. Indeed, observations from previous studies reveal that Fe-TiO_2 has the potential to improve current technologies and gain a bigger share of the AOP systems currently used to treat wastewater. This is due to the elevated oxidation reaction rates achieved through an unobstructed photocatalyst surface, as well as to the narrower band energy gap which allows photoactivation of the particles under cheaper, less energetic wavelengths (into the visible spectrum).

Some aspects of this novel material have already been elucidated, such as reaction rate constants and crystallite size. However, several questions remain that need to be answered in order to employ the photocatalyst safely and efficiently.

One of the questions this work addresses is whether Fe-TiO2 nanoparticles are generated during the synthesis of the photocatalyst powder. Like with many other substances, exposure to anatase titania nanoparticles poses concerns to human and environmental health. Since the synthesis method used to fabricate iron oxide-free Fe-TiO_2 is novel, a particle size analysis must be carried to ensure samples can be safely manipulated and employed in industrial applications. As well, a size distribution analysis will provide information on the catalyst surface area available for the desired reactions to take place. Such a study can direct efforts to fine-tuning the synthesis method towards photocatalyst particles that are safe and efficient.

Another aspect that is investigated in this work, and that has not yet been elucidated to the best of our knowledge, is the inner structure of the novel photocatalyst's particles. XRD peak broadening analysis has indicated that the catalyst's particles are composed of monocrystalline units of dimensions in the tens of nanometers, termed *crystallites*. It is unknown, however, how

these crystallites are organized within a particle, what the nature of the material bonding crystallites together is, or whether the infamous iron oxide contamination is present in the interior of the particles as well as on their surface. This study will provide insight on the mechanisms by which the gel $(-Ti-O-Ti-)_n$ network coalesces into the photocatalyst particles during synthesis, and whether the bulk-generated charge carriers encounter additional mobility barriers while percolating towards the surface of the particles to trigger oxidation reactions.

Chapter 2 Particle Size Distribution

This chapter presents the studies on size characterization of a Fe-TiO_2 sample carried out using Scanning Electron Microscopy. It opens with an introduction of the core issues to be investigated experimentally (2.1), followed by a description of the sample synthesis protocol (2.2.1), secondary electron image acquisition (2.2.2) and data processing approach (2.2.3). The results of the data analysis are presented next, along with their discussion and interpretation (2.3). The chapter closes with concluding remarks and recommendations for future work in the subsequent stages of research (2.4).

2.1. Introduction

The first work developed in this thesis was the study of the size distribution of a Fe-TiO_2 sample synthesized using the methodology developed in previous works by this research group. This novel material has shown improved performance in terms of photocatalytic activity, but its potential for applications might be limited due to the presence of nanoparticles. Particularly, approval by Health Canada for commercial applications could be significantly delayed if an appreciable fraction of the particles present in the sample is measured to be under 100nm in dimension, falling under the agency's "nanoparticle" category of materials. Nanoparticles have raised concern due to possible adverse effects on human and environment health, as exposed in Section 1.3.4.

Likewise, estimating the size distribution of Fe-TiO_2 particles could provide a better understanding of their overall performance. The photocatalytic reactions involved in cleaning wastewater are ultimately dependent on the particle surface area available for the generation of ROS, and the available surface can, in turn, be estimated using the particles' characteristic dimension. Another useful metric that can be inferred from the size distribution calculations is the distribution of sample mass across particle sizes (assumed to be proportional to the volume distribution, if particle density is assumed to be constant).

Therefore, the main goals of this study are:

I. Characterize the morphology of a Fe-TiO_2 sample through the calculation of its particle size distribution, determining the fraction of potentially harmful nanoparticles.
II. Draw insights, from the calculated distributions, about how particle morphology might affect photocatalytic performance (in terms of surface generation of ROS) and identify possible areas of improvement.

2.2. Experimental

2.2.1. Synthesis and sampling Fe-TiO_2 particles

Iron-doped titanium dioxide was synthesized using the sol-gel method outlined in Moradi (2017) [52] and described in detail below. The reagents used were of analytical grade and without further purification. Suppliers and quantities used are shown in Table 3.

Table 3 List of reagents used on the Fe-TiO_2 synthesis, with respective quantities and suppliers

Reagent	*Quantity*	*Supplier*
TTIP	90 mL	MilliporeSigma
$Fe(NO_3)_3.9H_2O$	0.6 g	Sigma-Aldrich
Ethanol	600 mL	Greenfield Global
Deionized water	21.6 g	UVic's Department of Biology
HNO_3	dropwise to regulate pH	Sigma-Aldrich
HCl	dropwise to regulate pH	Sigma-Aldrich

The particles were prepared using TTIP (Titanium Tetra Iso Propoxide) as a precursor and ferric nitrate as the iron (III) source. An iron-to-titanium atomic ratio of 0.5% was used as this was shown to be the optimal doping ratio for the photocatalytic activity of anatase [20]. The amount of water used corresponds to a 1:4 ratio of Ti:H_2O, which is adequate for the controlled hydrolysis of TTIP. Nitric acid was used to lower the pH of the solution and slow down hydrolysis, enabling the iron atoms to be incorporated more efficiently [108].

$Fe(NO_3)_3$ was completely dissolved into deionized water and the solution was dispersed into a large beaker of anhydrous ethanol using a magnetic stirrer. Concentrated HNO_3 was added to the beaker dropwise in order to maintain the pH between 2 and 3. The titanium precursor was added dropwise into the solution and the reaction medium was stirred continuously with a magnetic bar for 2 hours until a gel formed in the beaker. The evolution of this process is illustrated in Figure 12.

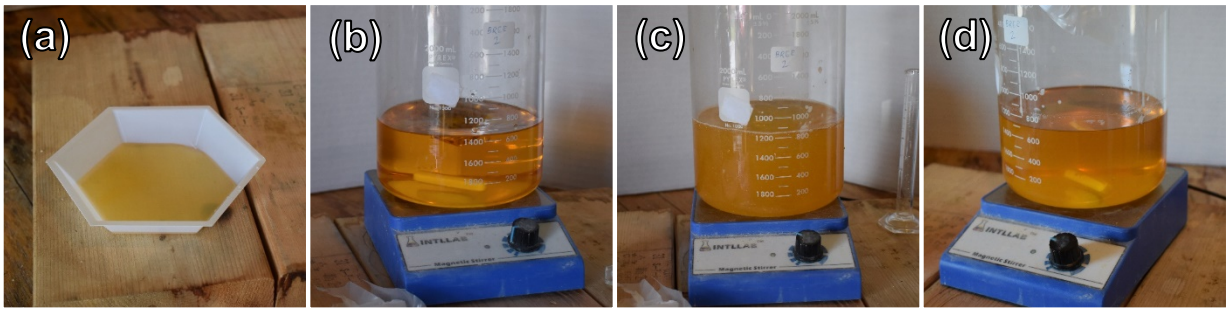

Figure 12 Images illustrating steps in the sol-gel process: (a) aqueous solution of the iron precursor; (b) beaker containing the reagents for the sol-gel synthesis before the addition of TTIP; (c) the solution becomes cloudy with the addition of the titanium precursor, marking the onset of hydrolysis; (d) at the end of the process, a transparent, viscous gel is formed

The gel was then poured into a refractory tray and dried completely in a furnace at 90°C for 2 hours. The resulting solid was then ground into a fine powder and washed with deionized water for 3 hours using a large beaker and a magnetic stirrer. This step is necessary in order to remove residual carbon compounds that might contaminate the particles' surface. The dispersion was returned to the oven to dry overnight at 95°C, which allows the volatile organic compounds formed during hydrolysis to evaporate. The resulting solid was ground again and brought to 400°C in a furnace to calcinate for 3h, allowing the anatase crystalline phase to form.

The crystallized Fe-TiO_2 was then ground again, using a different grinder to avoid cross-contamination, and washed in a solution of HCl overnight at pH 2-3. The particles were then

washed three times for 2 hours in deionized water in a stirred beaker and dried out at 95°C. Selected steps of the sample preparation are illustrated in Figure 13.

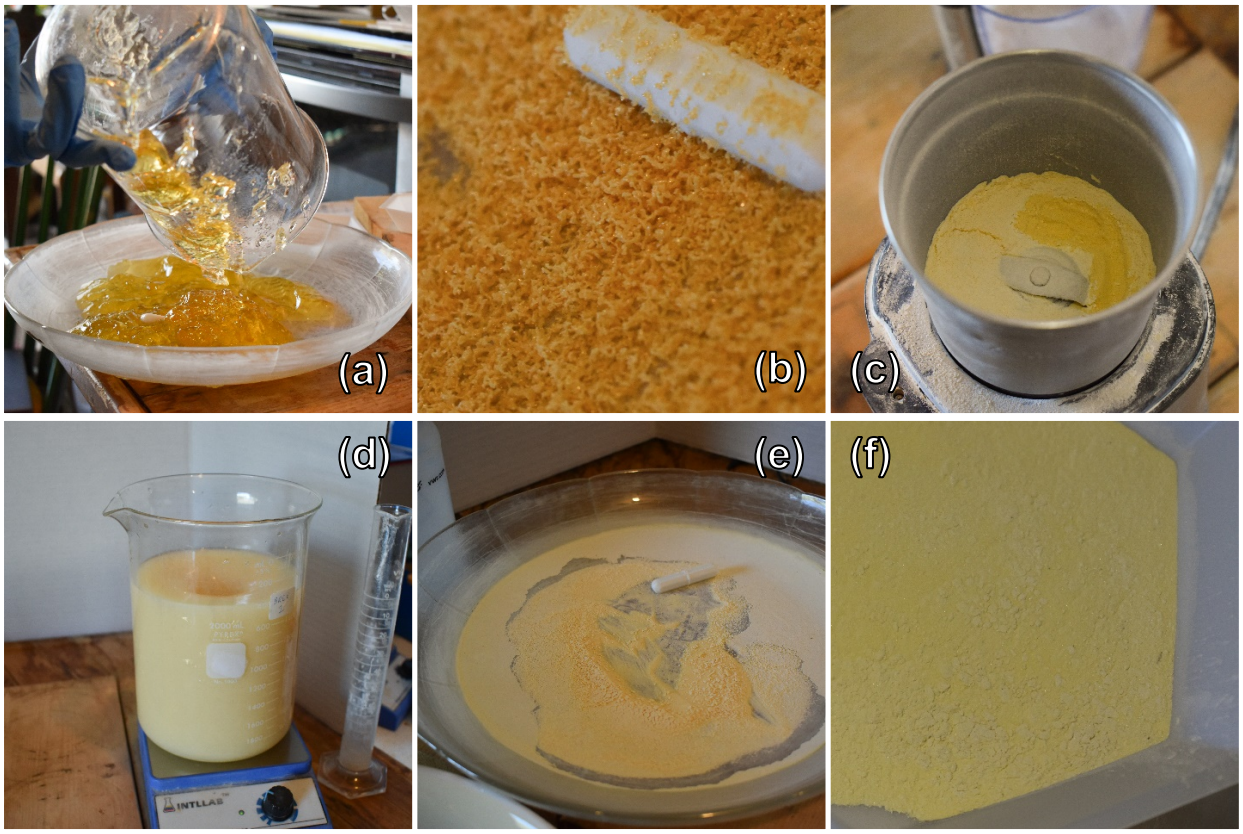

Figure 13 Steps on the synthesis of Fe-TiO_2 after gel formation: (a) transfer of the gel batch to a refractory tray for drying at 90°C; (b) close view of Fe-TiO_2 after drying from gel, showing the elongated shape of the particles; (c) particles after being ground to a fine powder, exhibiting some discoloration from exposure to air; (d) setup used to water- or acid-wash the doped titania particles; (e) Fe-TiO_2 particles before calcination; (f) iron-doped anatase titania after calcination at 400°C and acid-wash to remove iron oxide surface contamination

In order to verify the photocatalytic activity of the Fe-TiO_2 particles, part of the batch was reserved and added to a 10 ppm solution of methyl orange (Sigma-Aldrich). The suspension was brought into direct sunlight and stirred magnetically whilst photodegradation of methyl orange (M.O.) took place. The solution was sampled at regular intervals of time, filtered, and the M.O. concentration was measured using a spectrometer in the UV-Vis range (UNICO UV-3210PC).

The Fe-TiO_2 particles were moved onto a SEM stub using the following method. A small amount of powder (scooped with the flattened tip of a toothpick) was added to approximately 1 mL of ethanol in a small vial and shaken lightly by hand to form a suspension. The suspension was not sonicated, as we wished to study the agglomerate size without breaking down the particles any further. A few drops of that suspension were applied onto a regular Aluminum SEM stub, and the excess liquid was wicked away with filter paper by delicately bringing the paper into contact with the stub surface at a 45° angle. The stub was covered for dust protection and the residual ethanol was left to dry overnight.

2.2.2. Scanning Electron Microscopy

Due to the dielectric nature of the Fe-TiO_2 particles, a conductive coating had to be applied to the stub to facilitate electron drainage from the particles' surface and avoid charging problems while imaging. An amorphous carbon coating between 10 and 20 nanometers-thick was applied using a Cressington Carbon Coater (model 208carbon), maintaining a 30° deposition angle and constant rotation speed in order to reach regions of the stub which otherwise would be in the particles' shadow.

In order to estimate the particle size distribution of the sample, a Hitachi S-4800 scanning electron microscope was used to obtain secondary electron (SE) images of the Fe-TiO_2 powder dispersed on the aluminum stub. An acceleration voltage of 1 kV at a working distance of 5.2 mm was used to obtain images at magnifications ranging from 700 to 30,000. The low acceleration voltage was chosen to prioritize the visibility of surface morphology over bulk information (density contrast, etc). A short working distance was necessary to resolve small particles at high magnification levels. Different magnifications were needed to account for the wide range of particle sizes (less than 100 nm to up to 50 μm), which are not all well resolved at a given zoom level. At each magnification, a number of sites on the stub were chosen at random to ensure that the particle count is representative of the entire sample. A breakdown of the magnifications used, and the area surveyed, is shown on Table 4.

Table 4 Break down of number of images and area surveyed by SE imaging at each magnification level

Magnification	*# of sites surveyed*	*Total stub area surveyed*
700	5	1.07×10^{-1} mm^2
3,000	5	5.85×10^{-3} mm^2
6,000	20	5.08×10^{-3} mm^2
18,000	20	6.49×10^{-4} mm^2
30,000	10	1.17×10^{-4} mm^2

2.2.3. Data processing

ImageJ, an open-source image processing software, was used to analyze the SEM images and obtain the characteristic length of the Fe-TiO_2 particles visible in each picture. The actual pixel size was calculated by indexing the scale bar included in each of the images as a known length using ImageJ's "Set Scale" tool. The characteristic lengths could then be determined using the "Measure" tool on each individual particle, which generates a table of values that can be exported to a number-processing software such as Microsoft Excel for further analysis. Figure 14 illustrates the process of determining the pixel size for a given magnification and obtaining the characteristic length of a particle on ImageJ. It is important to note that the characteristic length was picked arbitrarily for each particle, in a transversal direction different than the respective major or minor axis as can be seen on Figure 14. This was considered acceptable as the majority of particles exhibited a relatively small aspect ratio (no bigger than 2:1) and the values were categorized into broad size ranges for the purpose of calculating the size distribution.

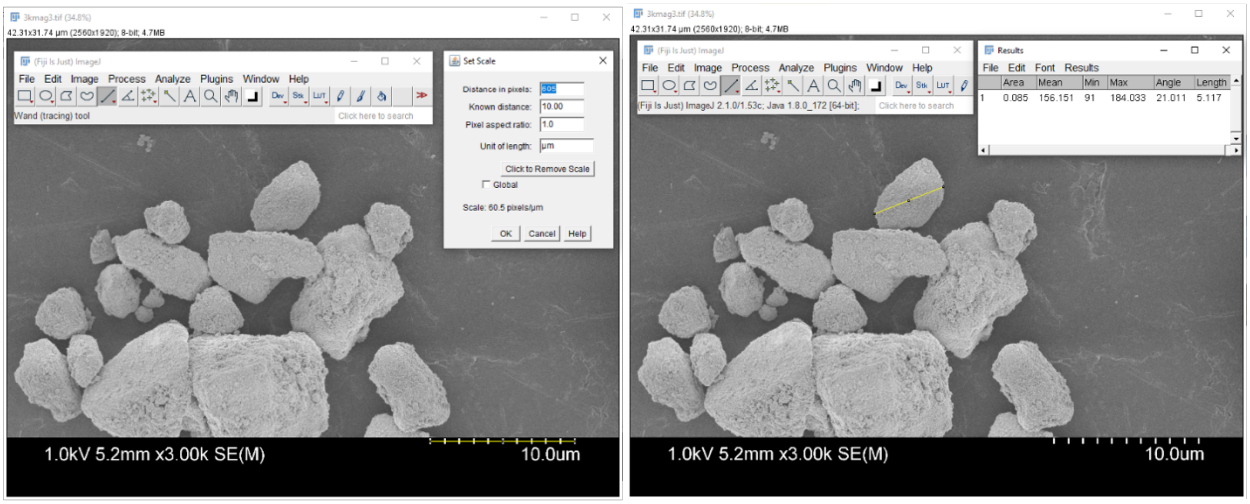

Figure 14 Calculation of the actual pixel size for a given magnification (left) and measurement of the characteristic length of an individual particle (right) on ImageJ

The particle measurements for each SEM image were sorted according to the size categories listed on Table 5, and a particle count per size category was established for each image. As well, the volume and surface area of each particle was roughly approximated as that of a sphere and the total particle volume and surface area per size category was tallied up.

Because the particles' size varies greatly, not all magnifications were found to be appropriate for analyzing all size categories. At lower magnifications, the smaller particles could not be resolved or accurately measured due to a large pixel size; at higher magnifications, the bigger particles are unlikely to be contained within the bounds of the image. For that reason, only images at selected magnifications were used in further calculations for each size category, as shown in Table 5.

Table 5 Size categories for estimation of particle size distribution, with the magnifications used in each category

Size category	*Range (μm)*	*Magnifications used*
1	0.0 – 0.1	6k, 18k, 30k
2	0.1 – 0.5	6k, 18k, 30k
3	0.5 – 1.0	3k, 6k, 18k, 30k
4	1.0 – 5.0	700, 3k, 6k
5	5.0 – 10.0	700, 3k
6	10.0 – 50.0	700

For each magnification, the total particle number, volume and surface area within a size category were calculated by adding up the values across all images taken at that magnification value. This is represented by Equation 42, Equation 43 and Equation 44, where P is the number of images taken, N is the particle count, V is the particle volume, S is the particle surface area, d is the particle characteristic dimension, and the indices c, mag and i refer to size category, magnification and picture number, respectively. Equation 45, Equation 46 and Equation 47 show the calculation of the of the particle number density ($\breve{N}$), specific particle volume ($\breve{V}$) and specific particle surface area ($\breve{S}$) per size category on the stub at each magnification.

$$N_{mag}^{c} = \sum_{i=1}^{P_{mag}} N_{mag,i}^{c} \quad \text{Equation 42}$$

$$V_{mag}^{c} = \sum_{i=1}^{P_{mag}} {}^{4}/_{3}\,\pi \left({}^{d_{mag,i}^{c}}/_{2}\right)^{3} \quad \text{Equation 43}$$

$$S_{mag}^{c} = \sum_{i=1}^{P_{mag}} 4\pi \left({}^{d_{mag,i}^{c}}/_{2}\right)^{2} \quad \text{Equation 44}$$

$$\breve{N}_{mag}^{c} = {}^{N_{mag}^{c}}\Big/_{A_{mag}} \quad \text{Equation 45}$$

$$\breve{V}_{mag}^{c} = {}^{V_{mag}^{c}}\Big/_{A_{mag}} \quad \text{Equation 46}$$

$$\breve{S}_{mag}^{c} = {}^{S_{mag}^{c}}\Big/_{A_{mag}} \quad \text{Equation 47}$$

In order to consolidate the data across all magnifications into a simple, useful breakdown by particle size category, Equation 48 through Equation 50 shown below were used. The values of $\breve{N}_{mag}^{c}$, $\breve{V}_{mag}^{c}$ and $\breve{S}_{mag}^{c}$ were used to calculate the weighted average values $\breve{N}^{c}$, $\breve{V}^{c}$ and $\breve{S}^{c}$ using the total area surveyed at each magnification (A_{mag}) as weights. This was done to mitigate errors introduced by the smaller sample size used at higher magnifications. It is worth repeating that only the magnifications listed on Table 5 were used in the calculations of the respective size categories.

$$\breve{N}^{c} = {}^{\sum N_{mag}^{c}}\Big/_{\sum A_{mag}} = {}^{\sum\left(\breve{N}_{mag}^{c}.\,A_{mag}\right)}\Big/_{\sum A_{mag}} \quad \text{Equation 48}$$

$$\breve{V}^{c} = {}^{\sum V_{mag}^{c}}\Big/_{\sum A_{mag}} = {}^{\sum\left(\breve{V}_{mag}^{c}.\,A_{mag}\right)}\Big/_{\sum A_{mag}} \quad \text{Equation 49}$$

$$\breve{S}^{c} = {}^{\sum S_{mag}^{c}}\Big/_{\sum A_{mag}} = {}^{\sum\left(\breve{S}_{mag}^{c}.\,A_{mag}\right)}\Big/_{\sum A_{mag}} \quad \text{Equation 50}$$

The surface-specific values $\breve{N}^{c}$, $\breve{V}^{c}$ and $\breve{S}^{c}$ were then converted into surface-independent values $N\%^{c}$, $V\%^{c}$ and $S\%^{c}$ using Equation 51 through Equation 53, representing the frequency of each size category, as well as the respective volume and surface shares. Those values are surface-independent and can be extrapolated to estimate the composition of the original Fe-TiO_2 sample.

$$N\%^c = \breve{N}^c \Big/ \sum \breve{N}^c \qquad \text{Equation 51}$$

$$V\%^c = \breve{V}^c \Big/ \sum \breve{V}^c \qquad \text{Equation 52}$$

$$S\%^c = \breve{S}^c \Big/ \sum \breve{S}^c \qquad \text{Equation 53}$$

2.3. Results

The spectrometry data yielded by the M.O. degradation experiment is shown in Figure 15. A calibration curve for methyl orange was obtained from concentration measurements using the same spectrometer (presented in detail in Appendix A, Figure 68 and Figure 69). The calibration curve was used to translate the absorbance data at 464 nm (which is an absorption peak for methyl orange, as seen in Figure 15) into concentration values for methyl orange in the reaction medium. The degradation data over time, both in terms of concentration of M.O. and degradation percentage, can be found in Figure 16.

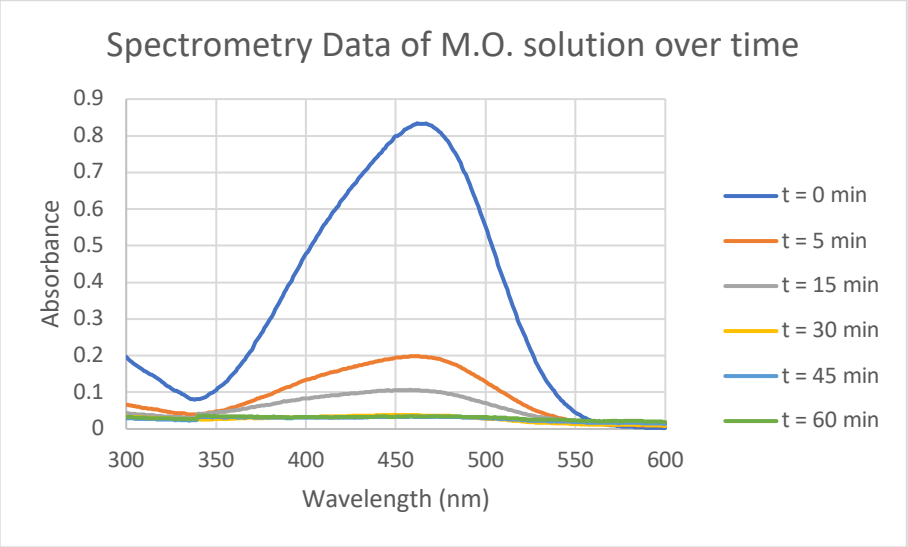

Figure 15 Evolution of measured absorbance of the reaction medium at wavelengths between 300 and 600 nm

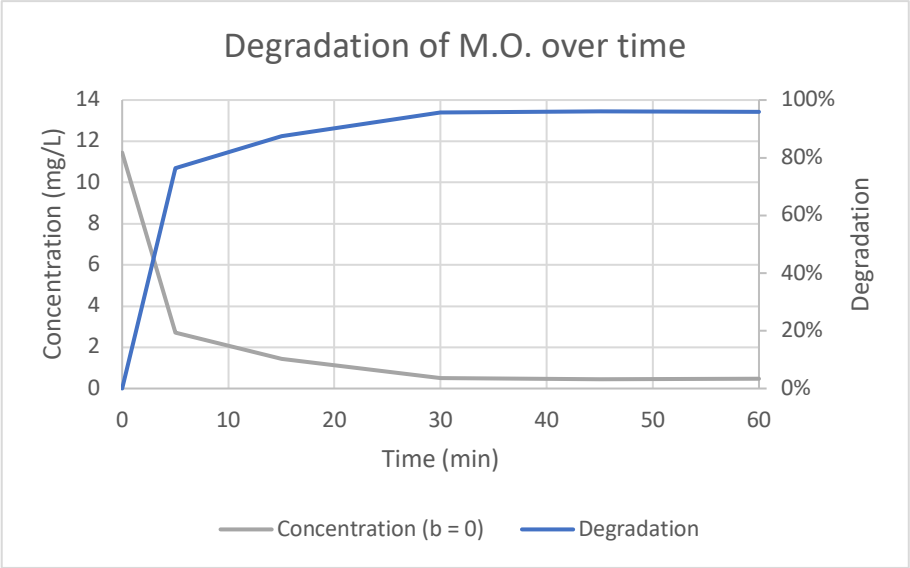

Figure 16 Methyl orange degradation data, plotted in terms of both concentration (main vertical axis) and degradation (secondary vertical axis) over time

The experimental data shows rapid degradation of the methyl orange solution via the photocatalytic effect of Fe-TiO_2 when exposed to intense natural light. As can be seen in Figure 16, close to 90% of the total amount of M.O. in solution is degraded in the first 15 minutes of the reaction, corresponding to an estimated apparent rate constant (from Equation 25) of $0.127\ min^{-1}$. This estimated rate constant is slightly superior (about twice the amount) to the values reported by Moradi et al. (2018) for anatase TiO_2 doped with the same amount of iron [20]. This can be attributed to different experimental conditions such as amount of photocatalyst added to the solution, batch size and radiation source used (direct natural light versus UV-filtered artificial light). The remaining M.O. in solution then proceeded to be almost completely degraded, up to about 96%, in the following 15 minutes of reaction. The rapid reaction rates upon solar exposition reveal that the synthetic method was successful in producing anatase TiO_2 particles with increased photocatalytic activity. It is important to note that errors bars are absent because the purpose of this experiment is not to estimate the reaction rate constant accurately, but to verify that the sample fabricated has photocatalytic activity.

Figure 17 shows examples of the SE pictures taken of the Fe-TiO_2 sample at different magnifications. Those four specific images were not taken at a random site on the SEM stub but were curated to illustrate how the magnification affects the visibility of particles in different size ranges. A comprehensive list of randomized images used to calculate the sample's particle size distribution can be found in Appendix B.

From Figure 17 it becomes clear that each magnification surveyed can only be used to count and measure particles within a certain size range. Otherwise, small particles will be measured incorrectly due to a characteristic dimension comparable to the pixel size and big particles will not be contained within the frame of the picture. At a magnification of 700x, it is easy to see particles of up to tens of micrometers, but particles smaller than 1 μm are not clearly resolved. At 3000x, it is possible to identify particles as small as 100 nm, however it becomes unlikely that particles bigger than 10 μm will be captured entirely within the frame. It is also at that magnification that one can start observing minuscule particles sitting on top of bigger ones. This observation adds

some error to the particle size distribution calculation: because it is hard to distinguish between diminutive particles and surface features of the large particles on a two-dimensional still image, these ambiguous particles were discarded when tallying up the numbers. This indubitably skews the final particle size distribution towards bigger particle sizes, as only a certain fraction of small particles rest against the darker aluminum background instead of adhering to the surface of larger particles. However, this error was found to be acceptable because the goal of this work was to find as accurate an estimate of the particle size distribution as possible within the experimental limits of the equipment used.

At a magnification of 6000x, particles smaller than 10 μm still fit well within the frame of the image and particles smaller than 100 nm can be clearly seen, as Figure 17 illustrates. However, the superposition of particles of roughly the same size often makes the boundaries unclear. This introduces some error into the calculations, which was found to be acceptable since the exact value of a given particle's characteristic dimension does not matter as much as the size category within which that particle falls. It was also observed that, for a magnification of 6000x, particles become scarce when the surveyed spots on the stub are randomized, as can be seen in the pictures for this magnification shown in Appendix B. This problem was mitigated by taking pictures of more random sites in order to increase the overall surveyed area. For magnifications higher than 18000x, particles bigger than 1 μm are very unlikely to be completely contained within the picture, and finding particles of any size becomes a challenge due to the small area surveyed per picture.

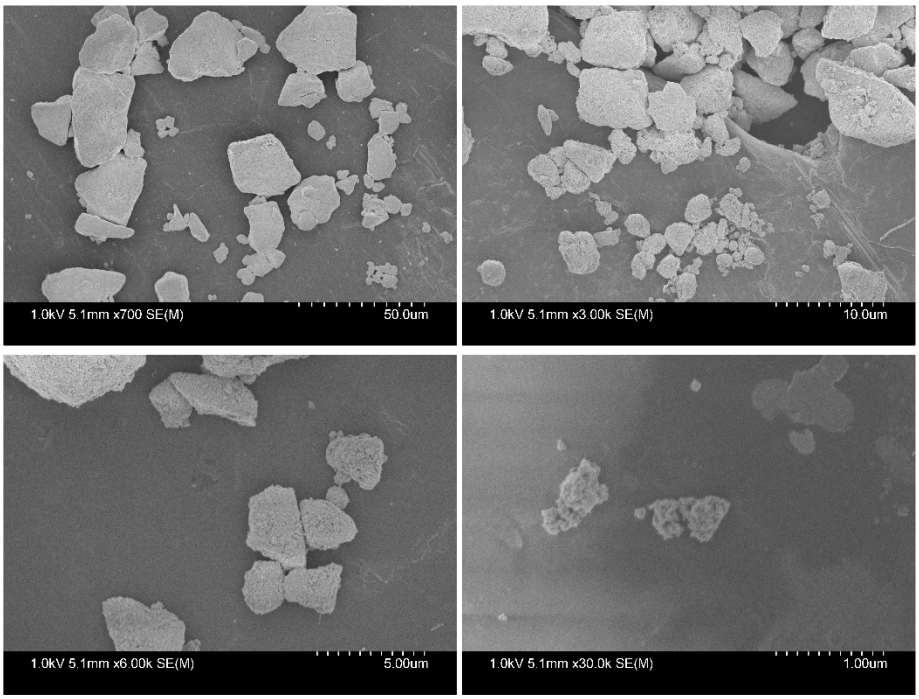

Figure 17 Illustrative examples of the size and aspect of particles expected to be seen at randomized sites at different magnifications

It is important to note that the difficulty in counting very small particles (less than 100 nm) arises from: a) them not being fully resolved (which is mitigated by employing higher magnifications); b) them being relatively scarce at high magnifications (which is mitigated by surveying a bigger area); c) them adhering to a bigger particle's surface; or d) their features being smoothed out by

the carbon coating during the sample preparation process. However, despite these difficulties, the scanning electron microscope employed for this study is largely suitable to identify very small particles against the stub background. Figure 18 shows that the difference in secondary electron emissions from TiO_2 and Aluminum provides enough contrast for particles as small as 30 nm to be clearly distinguished from surface features on the SEM stub. Therefore, one can be assured that, despite the challenges of counting and measuring small particles as described above, particles below 100 nm can be clearly seen against the aluminum stub background even though they might appear as unresolved specks at lower magnifications.

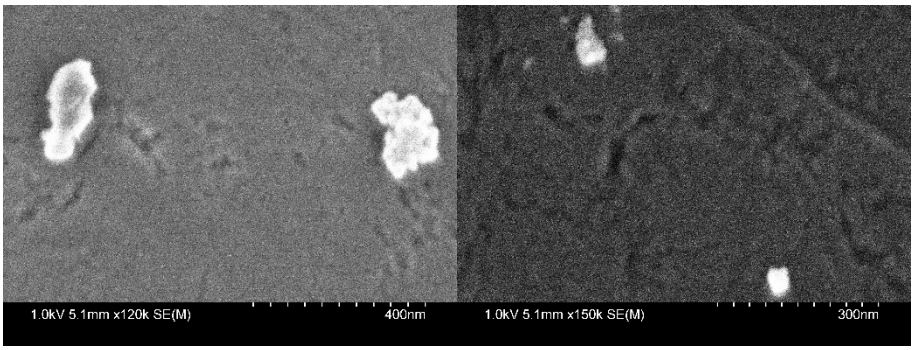

Figure 18 The contrast between TiO_2 and Aluminum due to different secondary electron emissions can be clearly seen even at high magnifications (120,000x on the left, 150,000x on the right)

These considerations were used to count all the particles in the SE images and systematically classify them according to the size categories described in Table 5. The results are presented in Table 6, where the columns show the number of particles (and their combined volume/surface) found in each magnification, and the rows divide the particle count (and respective combined volume/surface) into the aforementioned size categories. The numbers in red indicate the particle counts that will not be used for the final size distribution calculations, due to the magnification and particle size being incompatible as explained above. Table 6 also shows the total area surveyed at each magnification, and Figure 19 displays that information in graphic form to better illustrate the difference in sample size depending on the zoom level. The data labels in Figure 19 reveal that disparity: images taken at 700x surveyed an area roughly 18 times greater than those taken at 3,000x, and roughly 165 times greater than the images taken at 18,000x despite more random sites being surveyed at the latter.

Table 6 Number of particles (#), calculated combined volume (μm^3) and particle surface (μm^2) for different particle size categories, as inferred from SE pictures at different magnifications. Red figures indicate data considered inconsistent for size distribution calculation purposes. (table continues on next page)

Mag.	*700x* *1.07E-1 mm²*			*3,000x* *5.85E-3 mm²*			*6,000x* *5.85E-3 mm²*			*18,000x* *6.49E-4 mm²*			*30,000x* *1.17E-4 mm²*		
(μm)	*N*	*V*	*S*	*N*	*V*	*S*	*N*	*V*	*S*	*N*	*V*	*S*	*N*	*V*	*S*
0.1	0	0.00	0.00	6	0.00	0.12	95	0.02	1.40	9	0.00	0.08	8	0.00	0.09
0.5	3	0.09	1.42	99	1.86	30.20	129	1.66	29.69	11	0.11	2.17	5	0.05	1.00
1.0	42	12.16	86.52	43	8.32	67.64	40	10.57	77.22	2	0.16	1.80	1	0.21	1.73
5.0	577	8185	14254	47	439	866	32	126	304	6	44.84	96.36	1	1.78	7.11

10.0	195	35606	29263	12	1913	1662	2	205	212	0	0.00	0.00	0	0.00	0.00
50.0	62	$1.68x10^5$	50128	1	751	400	0	0.00	0.00	0	0.00	0.00	0	0.00	0.00

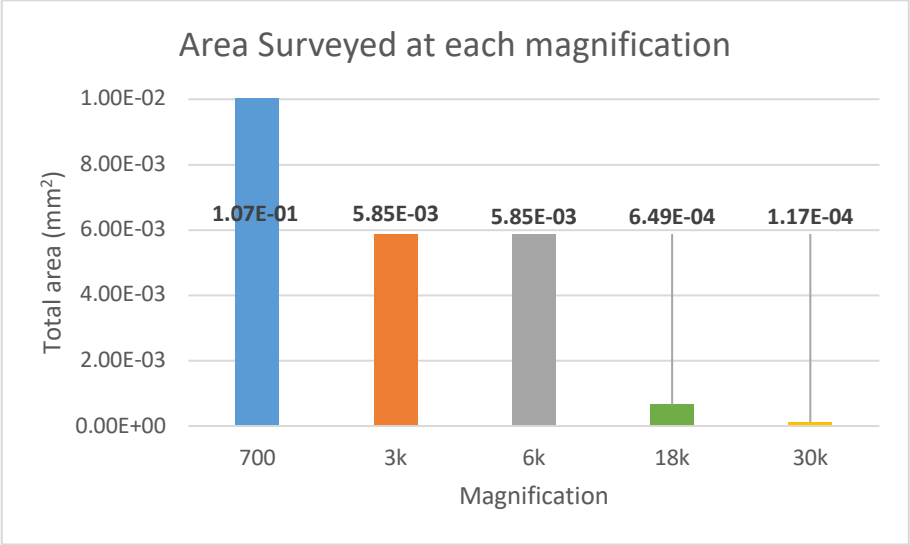

Figure 19 Chart illustrating the area surveyed using a scanning electronic microscope at each magnification. The leftmost column (magnification 700) is represented out of scale in order to fit the chart

The figures in Table 6 represent absolute numbers, which were then converted into surface-specific counts using Equation 45 through Equation 47 (surface area in mm^2). Those figures are shown in Table 7, where only the numbers in black will be used to calculate the final size distribution. Surface-specific data allows the results to be extrapolated to the entire sample as the total area surveyed affects no longer the magnitude of the calculated values, but solely their accuracy.

Table 7 Surface-specific values for the number of particles (in $\#/mm^2$), combined particle volume ($\mu m^3/mm^2$) and combined particle surface ($\mu m^2/mm^2$) found through imaging at several magnifications, divided by particle size category. Red figures indicate data considered inconsistent for size distribution calculation purposes

Mag.	*700x*			*3,000x*			*6,000x*			*18,000x*			*30,000x*		
(µm)	$\breve{N}$	$\breve{V}$	$\breve{S}$	$\breve{N}$	$\breve{V}$	$\breve{S}$	$\breve{N}$	$\breve{V}$	$\breve{S}$	$\breve{N}$	$\breve{V}$	$\breve{S}$	$\breve{N}$	$\breve{V}$	$\breve{S}$
0.1	0	0.00	0.00	1026	0.29	20.98	16243	3	241	13876	1.28	117	68524	8.38	747
0.5	28	0.86	13.20	16925	318	5164	22056	283	5076	16960	175	3339	42827	391	8602
1.0	391	113	806	7351	1422	11563	6839	1808	13203	3084	248	2780	8565	1839	14855
5.0	5376	76257	$1.33x10^5$	8035	75217	$1.48x10^5$	5471	21619	52032	9251	69138	$1.49x10^5$	8565	15288	60950
10.0	1817	$3.31x10^5$	$2.73x10^5$	2052	$3.27x10^5$	$2.84x10^5$	342	35078	36201	0	0.00	0.00	0	0.00	0.00
50.0	578	$1.57x10^6$	$4.67x10^5$	171	$1.28x10^5$	68338	0	0.00	0.00	0	0.00	0.00	0	0.00	0.00

Equation 48 through Equation 53 were used to consolidate data across all the magnification levels surveyed. The results of these calculations are presented in Table 8, where $\breve{N}$, $\breve{V}$ and $\breve{S}$ represent the surface-specific count, volume and surface distributions, respectively, for each of the size categories, while $N\%$, $V\%$ and $S\%$ represent those values normalized to 100%.

Table 8 Consolidated results across all magnifications for particle count and particle volume, in terms of surface-specific values and share per size category

Size category (um)	$\breve{N}$ $(\#/mm^2)$	$N\%$ $(-)$	$\breve{V}$ $(\mu m^3/mm^2)$	$V\%$ $(-)$	$\breve{S}$ $(\mu m^2/mm^2)$	$S\%$ $(-)$
0.1	16934	31.55%	3	0.00%	237	0.03%
0.5	21923	40.84%	275	0.01%	4968	0.59%
1.0	6900	12.86%	1546	0.08%	11907	1.34%
5.0	5511	10.27%	73521	3.71%	129571	14.61%
10.0	1829	3.41%	331483	16.74%	273222	30.81%
50.0	578	1.08%	1573270	79.45%	467008	52.66%

The following charts were generated in order to facilitate visualization of data presented in Table 7 and Table 8. The bars in Figure 20 show the surface-specific particle counts obtained at each magnification level, grouped by size category. Note that not all magnification levels are shown under all size categories, as per Table 5. The purple curve overlaid on top of the columns shows the final overall count share per size category, after all magnification levels were consolidated using the method described above. Figure 21 shows the same information, but in terms of particle volume per size category, and Figure 22 does so in terms of particle surface. Figure 23 compares the size, surface and volume distribution of the Fe-TiO_2 particles side by side.

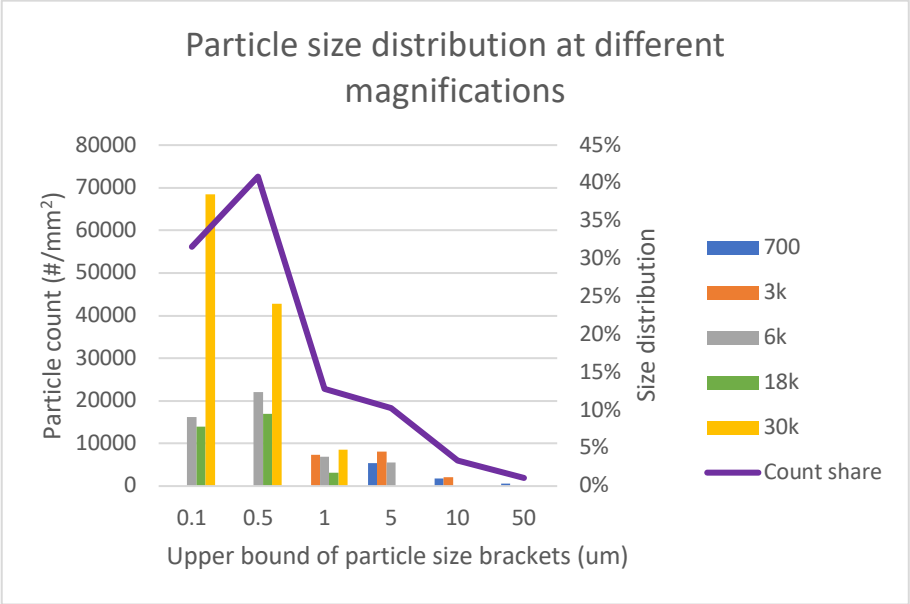

Figure 20 Chart showing the surface-specific particle counts obtained at different magnification levels and grouped by size category (bars), overlaid with a curve showing the final calculated size distribution

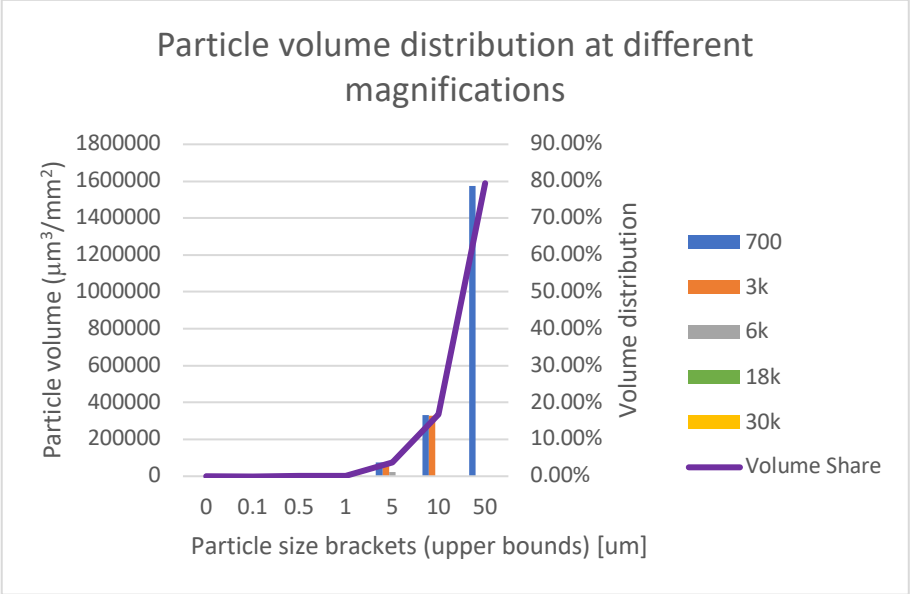

Figure 21 Chart showing the surface-specific particle volume obtained at different magnification levels and grouped by size category (bars), overlaid with a curve showing the final calculated particle volume distribution

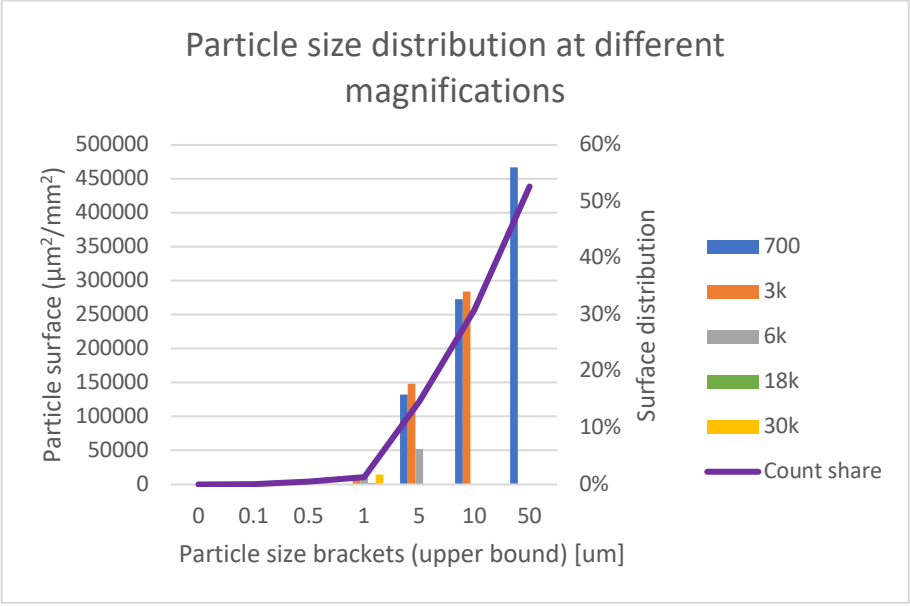

Figure 22 Chart showing the surface-specific particle surface area obtained at different magnification levels and grouped by size category (bars), overlaid with a curve showing the final calculated particle surface distribution

The column data in Figure 20 reveal that, while most magnifications yielded a similar particle count for a given size category, the calculations for 30k overestimated the presence of particles

smaller than 500nm. The counts at 30k were approximately 2.5 to 5 times greater than those at the lower magnification levels that were still able to accurately detect those particles (6k and 18k). This was somewhat expected, as finding particles at random sites becomes increasingly difficult when one increases the magnification levels, reducing the area surveyed. All of this contributes to increase the experimental error. However, due to the nature of the method used to consolidate data from different magnifications, the final values are skewed towards the data obtained using larger surveyed areas. This asymmetric weighing of the data sets contributes to offset the error generated by the small sample size of surveys at high magnification levels. This kind of discrepancy, however, cannot be observed in Figure 21 or Figure 22. In that case, experimental errors at high magnification levels are smoothed out when the particle volume or surface are calculated: as it can be seen in the charts, particles smaller than 1µm have a minuscule contribution to the total sample volume or surface area.

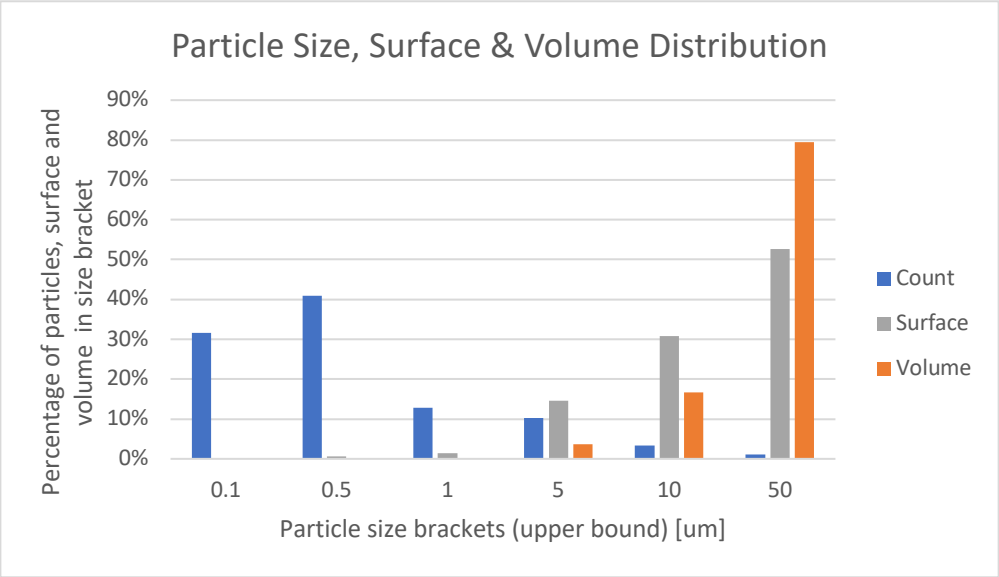

Figure 23 Column chart showing the final size, suface and volume distribution of a Fe-TiO_2 sample as calculated from SE images taken with scanning electron microscopy

Figure 23 groups the results for the size, surface and volume distribution calculations of the initial Fe-TiO_2 sample. The size distribution peaks in the 0.1-0.5µm bracket and is visibly skewed towards smaller particles sizes: 85.25% of all particles are smaller than 1µm, while the bottom 31.55% of the distribution is composed of particles smaller than 100nm and can therefore be correctly categorized as nanoparticles. It is expected that the true particle size distribution of the Fe-TiO_2 sample used could be further skewed to small particle sizes. As explained above, equipment limitations and other factors would have prevented all of the very small particles in the sample to be included in the count, if they were indeed present. This suggests that a considerable fraction of particles could fall below the 100nm threshold and therefore pose a risk to human and environmental health. An additional separation step during fabrication could sift out dangerous particle sizes and make the Fe-TiO_2 particles adequate for use, as it will be discussed in the conclusion of this chapter.

The surface and volume distribution data in Figure 23 reveal that the shape of the particle size distribution, peaking at 0.1-0.5µm, is smoothed out by the quadratic and cubic relationship of surface and volume, respectively, with the particles' characteristic length. In fact, particles bigger

than 1μm account for 98.07% of the total available surface area, and 99.91% of the total sample volume. When looking at particles bigger than 10μm, it can be verified that that group accounts for 52.66% of the total surface area and 79.45% of the total volume of the sample. Even if one considers that the true particle size distribution is skewed towards smaller particle sizes (compared to the estimated distribution in this study), it is safe to assume that the surface and volume distributions will still lean heavily towards bigger particles. The contribution of nanoparticles (smaller than 100nm) to the volume and surface distributions is close to negligible: 0.00015% and 0.03%, respectively.

As mentioned before, particle volume is proportional to particle mass if constant density is assumed. Similarly, particle surface area is assumed to be an indicator of photocatalytic activity, as the generation of Reactive Oxidating Species (ROS) occurs at the particle's surface. This indicates that small particles, namely those under 1μm, do not contribute significantly to the chemical activity of the Fe-TiO_2 sample, nor represent a significant fraction of the sample. This analysis supports the idea that nanoparticles could be filtered out of the sample without any meaningful losses to the reaction rate, and without any increase of the material costs involved in fabricating the particles. A bigger size cut-off could be employed to ensure nanoparticles are efficiently removed from the sample, and that would still be cost-efficient in terms of chemical activity and materials. A few methods for removing particles from the sample are described in the Conclusion section of this chapter.

On the other hand, it can be inferred from Figure 23 that a small fraction of particles concentrates almost the entirety of the sample's mass, while being responsible for virtually all of the oxidation reactions happening on the particles' surface. For instance, only 4.48% of all particles are bigger than 5μm and yet they represent 96.19% of the sample mass and are responsible for 83.46% of the surface chemical activity. Given that the surface-to-volume ratio of particles increase at a rate proportional to the inverse of its characteristic length (for spheres: $\frac{S}{V} = \frac{4\pi R^2}{4/3\pi R^3} = \frac{3}{R}$), one could expect a significant increase in the surface area, and hence photocatalytic activity, of the sample if the mass distribution were to be shifted to smaller particle sizes. This could be achieved by breaking down massive particles into intermediate sizes – arbitrarily small enough to create more surface area enhancing reaction rates, but not small enough to drop below the 100nm threshold and become harmful. The size range between 500nm and 5μm, for instance, could be adequate.

A list of all the randomized site images used to count and measure particles, as well as image-specific information, is shown in Appendix B.

2.4. Conclusion

The following insights can be drawn from the experimental results of this study:

- Methyl orange degradation experiments using Fe-TiO_2 particles under natural light showed rapid degradation of the model pollutant as expected, suggesting the synthetic method was effective in incorporating the optimal amount of doping agent into the crystalline lattice.
- Multiple magnifications were needed to investigate the size distribution due to the wide size range of particles and the obstacles associated with it (too big a pixel size or too narrow a field of view).

- Small particles resting on top of bigger particles often cannot be distinguished from surface features of the bigger particle, which skews the distribution curve towards larger particle sizes. Likewise, particles of sizes comparable to the Carbon coating applied onto the stub (10-20nm) might have their features smoothed out in the secondary electron images. However, there is enough contrast between the secondary electron emissions from Al and Fe-TiO_2 to allow small particles to be clearly seen against the Aluminum stub background.
- Lower magnification levels enabled the survey of a larger area of the stub, increasing the accuracy of the surface-specific results. Accordingly, higher magnification levels introduce an increasingly bigger error due to a smaller area surveyed.
- Errors in the estimation of volume and surface distribution stem from the approximate measurements of individual particles and from modelling them as spheres, which does not include form factors. However, due to the particles' aspect ratio relatively close to 1 and the power relationships between length, surface and volume (d^1, d^2 and d^3 respectively), the overall trend is expected to resemble the true distribution curve.
- The calculation of surface-specific values allows the extrapolation of the particle counts to the entire sample, and the accuracy of those results depend on the surface area initially surveyed.
- The size distribution for the sample used in this study is skewed towards small particle sizes (85.25% smaller than 1μm, 72.39% smaller than 500nm), but the approximated surface area and volume distributions show that bigger particles concentrate most of the sample's mass and chemical activity.
- The estimated fraction of nanoparticles (smaller than 100nm) in the sample is 31.55%, however that accounts for only 0.03% of the sample's surface area and 0.00015% of the sample mass. This indicates that a separation step could be added to the fabrication process to remove harmful nanoparticles from the sample, without significant losses to the reaction rates or reagent amounts used.
- Due to the relationship between specific surface and particle size, the photocatalytic activity of the sample is expected to improve if the particle mass distribution is shifted towards intermediate particle sizes.

This study has revealed the size, surface and volume profile of the novel Fe-TiO_2 particles synthesized using a sol-gel method. It has also addressed potential areas of improvement, both in terms of increasing the surface area available for AOP reactions and in terms of making this material safe for day-to-day applications.

Increasing the reactive surface area of Fe-TiO_2 particles is done by shifting the mass distribution towards smaller particle sizes, which can be achieved by breaking up big particles at the later steps of the fabrication process. Extending the time of the grinding step during synthesis, or increasing the grinder's power, can be expected to result in a finer mass distribution. Another possible solution would be to sonicate an aqueous suspension of the particles, which might break down the bigger aggregates. Ideally, this additional refinement step would limit particle size to under 5μm.

Removing nanoparticles from the sample can be most easily achieved by introducing a separation step to the fabrication protocol, most likely following the additional particle break-up step explained above. This would ensure that any new nanoparticles released from the big aggregates are also removed from the sample. Separation methods based on the particles' fluid dynamics are promising: a cyclone separator, for instance, uses a pressurized air stream to carry the

samples into a cylindrical chamber, where the balance between air drag and centrifugal force will segregate big particles towards the walls of the chamber. Since a fluid's velocity is generally smaller close to static interfaces than in the bulk of the stream (no-slip boundary condition), the big particles fall to the bottom of the cyclone separator. Small particles are carried away by the reject air stream through a central shaft, exiting from the top of the unit. Cyclone separators are a versatile unit that has been widely studied and used in the chemical industry [109]. The particle size cut-off can be carefully selected by fine-tuning the unit's geometry (inner and outer diameters, length, inlet/outlet dimensions) and the operation's parameters (air flow rate, air pressure, concentration of particles in the inlet stream). The simple geometry of this unit also makes it easy to prototype via 3D printing, which would enable quick initial testing until the final geometry and operation parameters are determined. A reasonable lower bound for particle cut-off would be around 500nm, providing a good safety margin from the 100nm threshold which characterizes particles as nano-sized.

Future work following this size distribution analysis will focus on improving the fabrication process to optimize photocatalytic activity while minimizing health concerns stemming from the presence of nanoparticles, as described above. Another area for improvement during the synthesis is the analysis of the residual liquid used to wash the particles at different steps of the fabrication process. The identification of residual organic by-products of the hydrolysis reactions (assumed to be mostly alcohols, such as isopropanol, or ethers generated by the condensation of alcohols, such as diisopropyl ether) can provide insights about the sol-gel reactions taking place and about the purity of the final product. Unfortunately, a High-Performance Liquid Chromatograph (HPLC) was not available for this analysis at the time of this study. Finally, improvements to electron microscopy analysis can be conceived in order to refine the accuracy of the final particle size distribution, such as: fine-tuning the thickness of the carbon coating to avoid smoothing out nanoparticles of comparable size while still preventing charge-up issues; employing a higher acceleration voltage to detect Fe-TiO_2 nanoparticles under the amorphous carbon layer; and adding a sonication step during the sample preparation to separate big particles from smaller ones that might adhere to their surface.

Chapter 3 Electron Microscopy Analyses

This chapter presents the morphological and compositional characterization of Fe-TiO_2 nano-crystallites using high-resolution scanning and transmission microscopy. An introductory section (3.1) explains the relevance of this study and outlines its experimental goals. The experimental section details the sample preparation method (3.2.1 and 3.2.2), as well as the configuration of both high-resolution microscopes employed to collect data and the analysis methods that follow (3.2.3 and 3.2.4). The results of the sample fabrication and data processing are presented next, along with discussion and interpretation (3.3). The chapter closes with concluding remarks and recommendations for future work in the subsequent stages of research (3.42.4).

3.1. Introduction

The novel, highly active Fe-TiO_2 particles have been previously characterized in terms of their macroscopic properties such as reaction rate constants, electronic band gap energy [52] [110], particle size distribution (Chapter 2 of this work), etc. However, it is also important to investigate the particles' characteristics at a very small scale in order to obtain insight about the resulting macroscopic properties. This, in turn, can direct further efforts towards understanding and optimizing the photocatalytic performance of this novel material.

The photocatalytic activity of semiconductors originates from the separation of charge carriers within the bulk of the material, which then percolate to the surface of the particles to catalyze AOP reactions. It has also been shown [20] that, for iron-doped titania specifically, the iron content tends to accumulate on the surface of the photocatalyst particles as iron oxides and that this contamination layer can be chemically removed to greatly enhance the material's catalytic activity. However, the crystalline and compositional structure of Fe-TiO_2 within the photocatalyst particle has yet to be elucidated. The distribution of iron within the particles has not yet been investigated and, if Fe atoms segregate to inner regions of the catalyst as iron oxides, that could form an additional barrier in the path of charge carriers towards surface reactive sites.

Analyses by XRD peak broadening [20] have revealed that Fe-TiO_2 particles are polycrystalline structures formed by monocrystalline units (crystallites) of size ranging from approximately 5.9 to 13 nm depending on the concentration of doping agent. The morphology of these crystallites has yet to be demonstrated. The nature of the material joining crystallites together is also still unclear, even though it is initially suspected to be amorphous TiO_2 with unknown iron content. Having a clear understanding of the inter-crystallite structure is important because it provides answers to whether charge carriers formed deep within the particles are able to move easily towards the interface with the reaction medium and contribute to the reaction rates. For instance, the iron atoms that fail to be incorporated into the crystallites' lattice could potentially accumulate in the inter-crystallite space as iron oxide and act as recombination centers, hindering charge carrier mobility.

Fabricating a Fe-TiO_2 sample as a thin specimen facilitates the investigation of its inner structure. Reducing the specimen thickness to a few crystallites' width (in the tens of nanometers) enables the use of transmission and scanning-transmission imaging. The resulting secondary electron

and bright field images have increased spatial resolution that allows the observation of individual crystallites as well as of the regions of different crystallinity within the specimen. Moreover, one can extract valuable crystallinity information from diffraction patterns of the polycrystalline sample or from digitally generated Fourier Transforms of monocrystalline regions within the specimen. Lastly, compositional information can be obtained from Electron Energy Loss Spectrometry (EELS) and high-resolution EDX. The increased spatial resolution for EDX on thin specimens stems from the fact that only the region immediately close to the electron beam spot is excited to emit characteristic X-rays, since the reduced thickness prevents the X-ray generating region from blooming under the sample surface. Effects such as self-absorption of X-rays by the sample and fluorescence are also minimized.

The goals of this study are therefore the following:

I. Fabricate a Fe-TiO_2 specimen allowing the use of electron microscopy techniques requiring a reduced specimen thickness.
II. Obtain information on the crystallinity of the Fe-TiO_2 crystallites and inter-crystallite regions using said electron microscopy techniques.
III. Investigate the concentration of Fe in different regions of the Fe-TiO_2 specimen using advanced compositional analyses.
IV. Draw insights about crystallite growth and iron oxide formation during Fe-TiO_2 synthesis from the information gathered.

3.2. Experimental

3.2.1. Sampling Fe-TiO_2 particles

Iron-doped titanium dioxide particles were synthesized using the protocol described in detail in Section 2.2.1. A piece of conductive carbon tape was placed on a standard SEM sample stub, and the dry Fe-TiO_2 powder was sprinkled on the tape. The purpose of the carbon tape is twofold: to hold the particles in place enabling careful manipulation with a microprobe, and to drain the charge resulting from the collision of the Focused Ion Beam with the sample. The excess powder was delicately shaken off, and the stub was mounted onto a FIB stub holder. The entire ensemble was taken to a Hitachi FIB (model FB-2100) for the lift-off and milling procedure.

The FIB system uses an accelerated, focused Gallium ion beam to interact with the sample in the following ways: magnification (through a secondary electron detector), etching (due to the impact of heavy Ga ions with the sample) and welding (in the presence of a gaseous tungsten precursor). Any of these competing effects can be selected by carefully managing the Ga beam parameters such as acceleration voltage, current and apertures used. As well, welding is conditional to the presence of a tungsten precursor which is deposited as solid W upon contact with the ion beam. For this study, 4 configurations of the Ga beam were used, labeled as follows: 40-0-30 (for magnifying), 40-0-80 (for welding), 40-1-80 and 40-1-150 (both for cutting, depending on the required intensity). The first number on these labels is the same for all four beams, corresponding to the accelerating voltage employed (in kV). The second number indicates the ion beam current, with a value of 1 corresponding to an increase of four times compared to the current's base level indicated by 0. Finally, the last number indicates the diameter of the aperture used for the ion beam, in μm.

Figure 24 shows the procedure for lifting off a particle from the sample stub. A digitally controlled microprobe is used to approach a suitable particle on the surface of the stub (a), which is then welded to the probe by the deposition of a metallic tungsten strip covering both the probe's tip and the particle's surface (b). Finally, the sample stage is lowered down while the particle remains attached to the probe (c). It can be seen in the figure that some residue from the carbon adhesive tape is lifted off with the particle, which is allowed at this stage as it will be removed during the milling step.

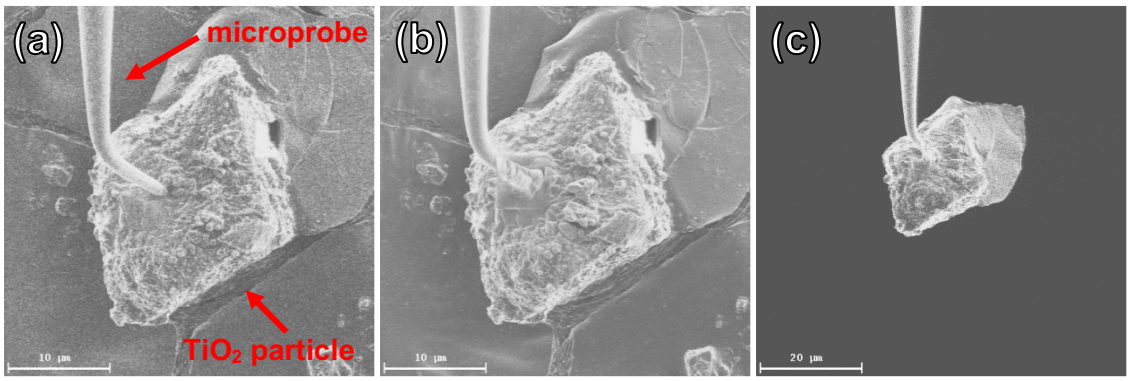

Figure 24 Secondary electron images showing (a) the microprobe approaching a Fe-TiO_2 particle secured to a stub with adhesive carbon tape; (b) the microprobe welded to the particle using a tungsten precursor gas; and (c) the particle lifted off the stub by the microprobe (with a patch of carbon tape still attached)

Figure 25 shows the method by which the Fe-TiO_2 particle is transferred from the microprobe to a TEM sample holder (a multi-pronged copper half-grid). The TEM half-grid is inserted into the FIB specimen chamber and positioned in close proximity to the microprobe supporting the titania particle (a). Once contact between the particle and the grid is established, the focused ion beam is used to weld the contact points (b). With the particle secured to the grid, the microprobe is milled off around the region where it is attached to the particle, and then taken out of the specimen chamber (c).

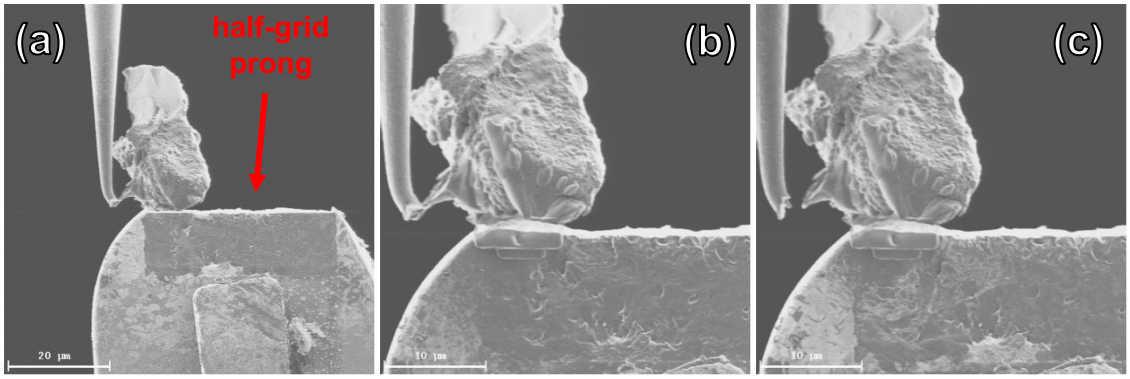

Figure 25 Secondary electron images showing (a) the particle suspended from the microprobe approaching a prong on a TEM copper half-grid; (b) the particle welded to the prong using a tungsten precursor gas; (c) the particle being separated from the microprobe by the ion beam

The contact point between the TEM grid and the particle must be welded securely on both sides to ensure the sample can be milled into a thin TEM specimen without falling off. Figure 26

illustrates that procedure, which consists of rotating the TEM half-grid 180° around the sample holder axis (a) and applying a thick layer of tungsten to the base of the particle (b). This ensures the specimen will stay firmly attached to the half-grid and will not be lost during milling or transfer between different specimen holders. This lift-off protocol was repeated for a total of three Fe-TiO_2 particles attached to the same TEM half-grid, ensuring redundancy of the samples.

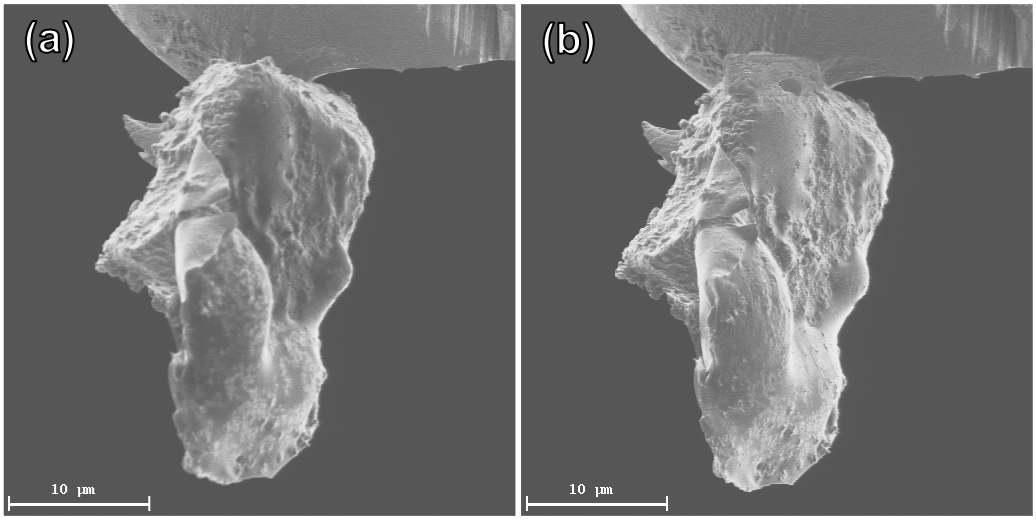

Figure 26 Secondary electron images of the particle attached the TEM copper grid after being flipped over to reinforce the tungsten weld, (a) before and (b) after the weld was applied to the contact points

3.2.2. Specimen preparation

In order to be able to observe the Fe-TiO_2 particles with a transmitted electron beam, the specimen must be thinned. The desired upper bound for the specimen thickness is usually the extinction distance of the electron beam in the [111] crystalline direction (lowest order plane that diffracts). For most materials, a thickness of under 100 nm is enough to achieve this. This was accomplished by using the FIB to mill the particles into a wedge with an angular opening of 45°. The sampled particles were rotated in the FIB specimen chamber by an angle of +22.5° and -22.5° around the sample holder axis, and the “cutting” configuration of the Gallium beam was used to cut the particles to the desired wedge shape. Figure 27 illustrates that procedure.

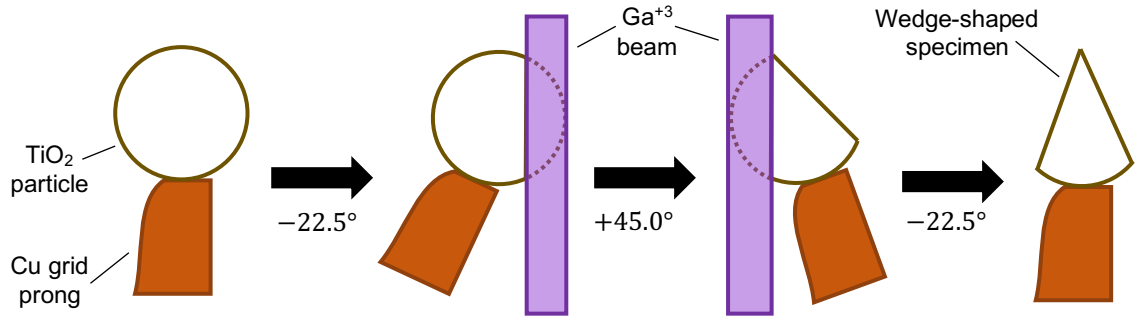

Figure 27 Procedure to cut Fe-TiO_2 particles into wedge-shaped TEM specimens using the FIB

The FIB milling technique can produce a wedge-shaped specimen whose thickness progressively decreases towards 0 immediately next to the edge. However, it also produces a damage layer on the surface of the specimen due to the inertial impact of the large, heavy Ga ions with the crystalline substrate. For this synthesis, the depth of the damage corresponding to ion implantation and disorganization of the lattice structure was estimated to be roughly 40 nm. A superficial polishing was carried using an Argon broad ion beam (Fischione Instruments “Low Angle Ion Milling & Polishing System”, Model 1010). This broad ion milling step was done at a shallow angle of 15° on each side of the specimen, using an ionic current of 5 mA accelerated by 3 kV, and with stage rocking of ±35°. The configuration of the TEM half-grid on the sample holder used for this step is shown in Figure 28.

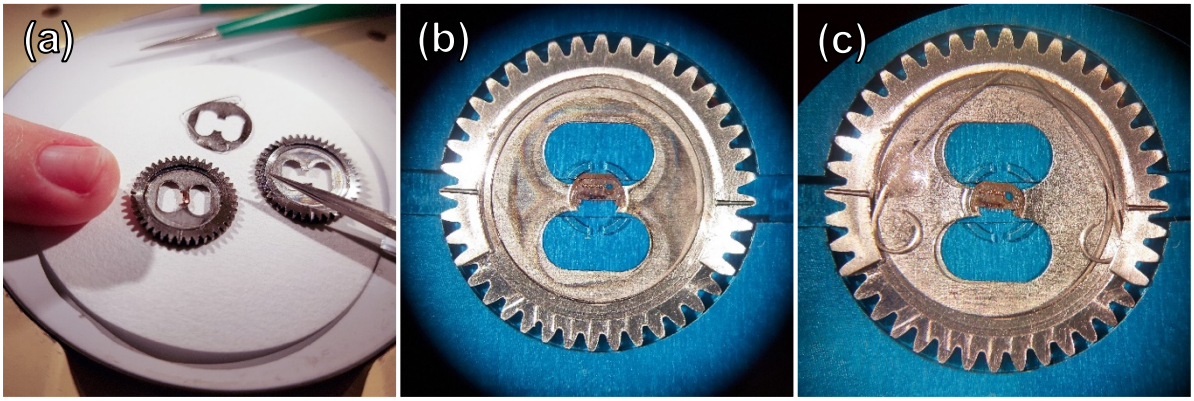

Figure 28 Sample holder enabling stage rocking in the broad ion milling system, composed of a gear-shaped base and a removable top piece to clamp the Cu half-grid in place

Low-resolution scanning electron microscopy was used to monitor the state-of-surface of the Fe-TiO_2 specimen throughout the milling step. A Hitachi S-4800 SEM with compositional analysis capabilities was used. The specimen was taken out of the broad ion miller equipment at pre-determined time increments and transferred to an SEM sample stub. A piece of carbon tape was used to delicately secure the TEM half-grid to the substrate (Figure 29). Secondary electron images (1 kV accelerating voltage, 7.9 mm working distance) of the specimen were obtained throughout the surface polishing step, as well as Energy Dispersive X-Ray (EDX) maps (19 kV accelerating voltage, 15.1 mm working distance). The ion polishing was carried for a cumulative total of 12 minutes, at the end of which the secondary electron images indicated the surface of the specimen was clear of the gallium damage layer.

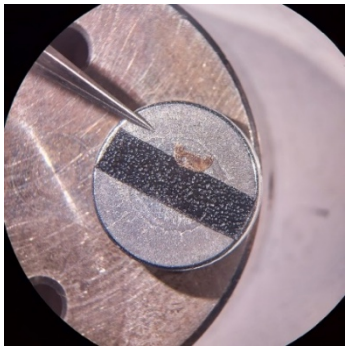

Figure 29 Sample holder setup for observing the TEM specimen in the SEM. A strip of conductive carbon tape was used to secure the TEM half-grid in place

Finally, a Hitachi ZoneTem sample cleaner was used to remove hydrocarbon contamination which might be adsorbed on the surface of the specimen. The specimen was initially cleaned for 30 minutes on each side, and subsequently another 10-15 minutes per side before being inserted into the specimen chamber if it was exposed to ambient atmosphere for an extended period of time.

3.2.3. High-resolution STEM imaging and EDX

A Scanning Transmission Electron Microscope (Hitachi STEM model SU9000) was employed to obtain high magnification information on the Fe-TiO_2 specimen. Figure 30 shows the configuration of the specimen holder used, which allows the electron beam to generate both Secondary Electron (SE) and Bright Field (BF) signals as it travels across the thin region of the wedge-shaped sample. The high opening angle of the holder under the sample (as can be seen in Figure 30 (c)) makes it possible to obtain High-Angular and Low-Angular Annular Dark Field images (HAADF and LAADF, respectively), although these types of imaging were not used in the present study.

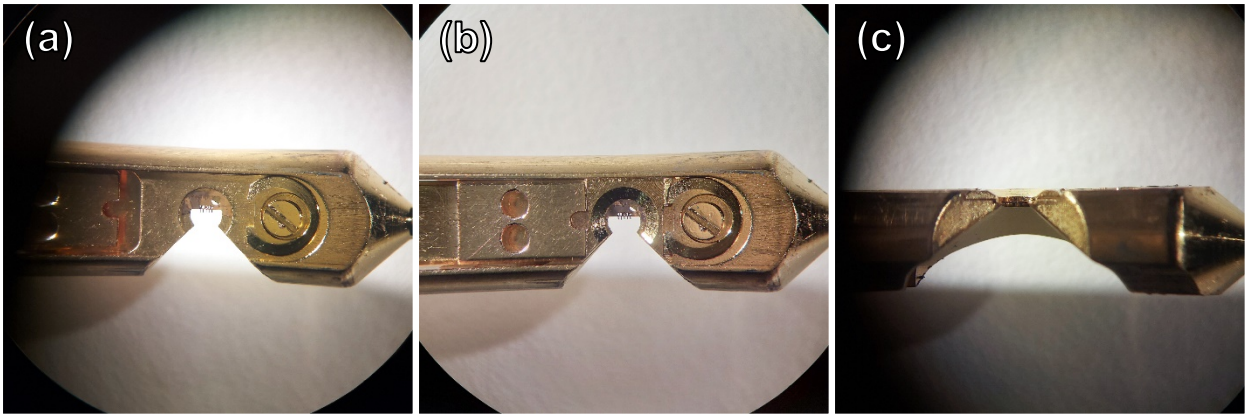

Figure 30 Configuration of the specimen holder used for STEM imaging in the SU9000 system, illustrating (a) the TEM half-grid resting on the holder, (b) the half-grid locked into place and (c) the sample rotated of 90° revealing the path of the transmitted electron beam, from top to bottom

For topographical and transmission imaging, the sample was positioned at a working distance of 1.198 mm and the electron beam was accelerated by a voltage of 25 kV, providing an emission current of 9800 nA. Several images of the thin edge of the wedge specimen were taken using SE and BF signals, up to a magnification of 1000k times.

Compositional information of the specimen was obtained by EDX at an acceleration voltage of 10 kV. Element data was obtained in the form of line scans and point analysis. Compositional profiles were plotted using software-generated element counts and count ratios. The relative abundance of elements in the point analyses was provided by the signal processing software used based on the characteristic emissions from elements present in the specimen. Elemental mapping could not be accurately determined due to relatively homogenous concentrations of Ti, Fe and O in the sample area scanned, and instability of the quantification function of the EDX software used. The generated element maps exemplifying this are shown in Appendix C.

3.2.4. High-resolution TEM imaging and EELS

A Scanning Transmission Electron Holography Microscope (STEHM, Hitachi HF-3300V) was used to collect transmission and diffraction images, as well as Electron Energy Loss Spectroscopy (EELS) spectra on scanning-transmission mode, from the thin edge of the Fe-TiO_2 specimen. The holography imaging function of the microscope was not used for this study. An acceleration voltage of 200 kV was employed, enabling magnifications of up to 810k times. The camera length used for identification of diffraction patterns was 1.0 m.

All images and spectra were treated using the Digital Micrograph software. The “Fourier Transform” tool was used to generate spot diffraction patterns from seemingly crystalline and amorphous regions in images taken using the microscope’s “imaging mode”. “Diffraction mode” imaging of polycrystalline regions of the sample generated ring diffraction patterns which were used to characterize interplanar spacings and diffraction angles. As well, an aperture was used to select specific regions of the ring diffraction patterns and highlight the individual monocrystals contributing to that diffracted intensity. The EELS spectra of several regions along the edge of the specimen were analyzed to investigate the presence of segregated iron oxides in the amorphous material between monocrystals.

3.3. Results

3.3.1. Specimen preparation

The Focused Ion Beam milling procedures yielded three wedge-shaped Fe-TiO_2 samples attached to a prong on a TEM copper half-grid, as can be seen from several angles in the FIB-SE pictures shown in Figure 31. All three specimens have an opening angle of 45°, with depth dimension at the base between 4 and 6 μm tapering to 0 μm at the edge, and a height between approximately 5 and 7 μm when observed from the side. The images show that the wedges possess a sharp, well-defined edge that might be ideal as a thin specimen for transmission microscopy observations. Both sides of the specimens are relatively smooth, with a few streaks along the longitudinal direction (better seen on the right-hand specimen in Figure 31) which could be imperfections resulting from the milling ion beam. As well, there is a slight difference in brightness between the region closer to the edges (darker) and closer to the base (brighter) of the specimens. This difference in SE emissions is clearer in the pictures taken by the S-4800 microscope, which show better contrast and will be addressed later. The brighter regions could be a result of two phenomena during the FIB milling step: the superficial implantation of Ga ions, material at the base of the wedges (W, Cu) being sputtered back onto the sample, or a combination of both.

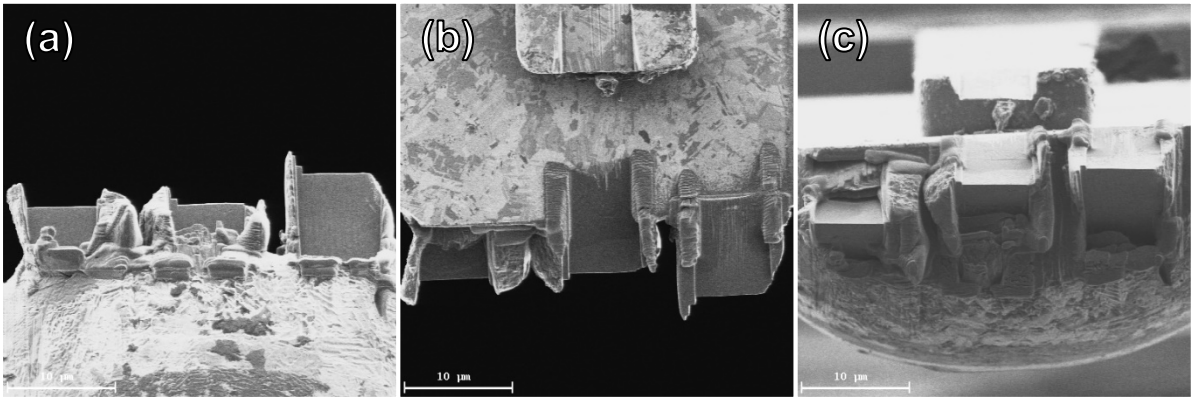

Figure 31 Secondary electron images of different views of the specimen after being milled with a Ga focused ion beam

The EDX analysis of the specimens provided information on the nature of the damage layer created by the FIB milling process. Figure 32 shows the elemental mapping of Ti, Ga and Al on the surface of one specimen, right after the FIB milling and without any additional surface polishing. The aluminum map is a good visual indicator of the increase in specimen thickness along the longitudinal direction (height) of the wedge: the background counts originating from the Al sample holder stub decrease as less of the electron beam is able to travel through the specimen and excite Al atoms. As well, the Ga map shows that although there are counts originating from everywhere in the image, they are concentrated on the surface regions of the original particle which were not milled into the wedge shape. Moreover, the milled surface exhibits a concentration of counts that is comparable to that originating from the background of the image, suggesting that this face of the specimen might only contains Ga in trace amounts. This suggests that ion implantation occurred weakly (if at all) in the direction that is perpendicular to the ion beam. The higher concentration of Ga on the untouched surfaces of the original particle was most likely implanted during the sampling step, where the entire particle was directly exposed to the ion beam. Figure 33, showing the compositional profile along the longitudinal direction of the wedge, supports this analysis. One can clearly observe the Al atomic ratio decreasing while that of Ti and O increase along the thickness of the specimen. As well, the concentrations of W and Ga are not relevant until 9 µm into the specimen, clear of the clean wedge face. This analysis indicates that the damage layer on the specimen is amorphous titania without Ga contamination.

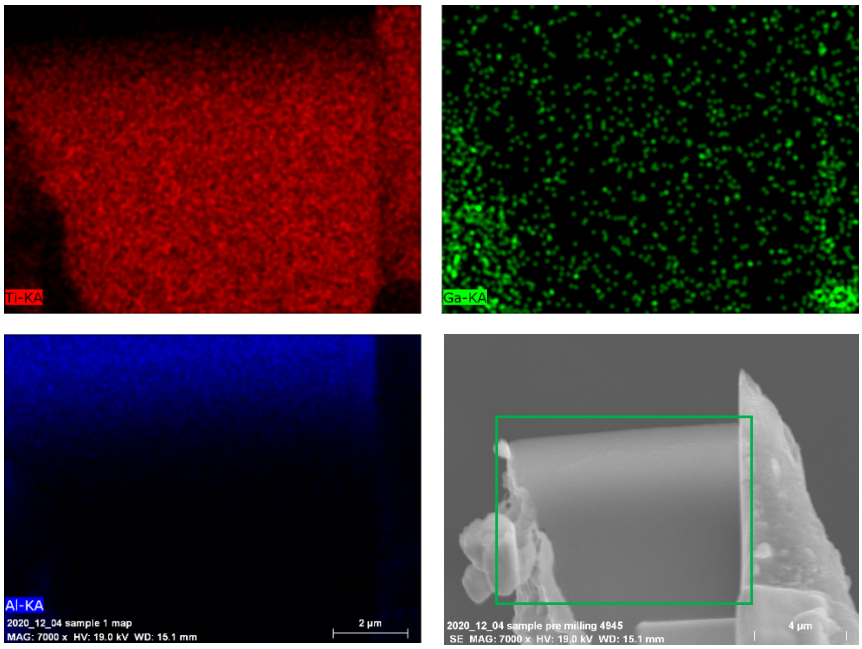

Figure 32 EDX mapping (Ti, Ga, Al) and SE image of a FIB-millled Fe-TiO_2 TEM specimen before surface cleaning

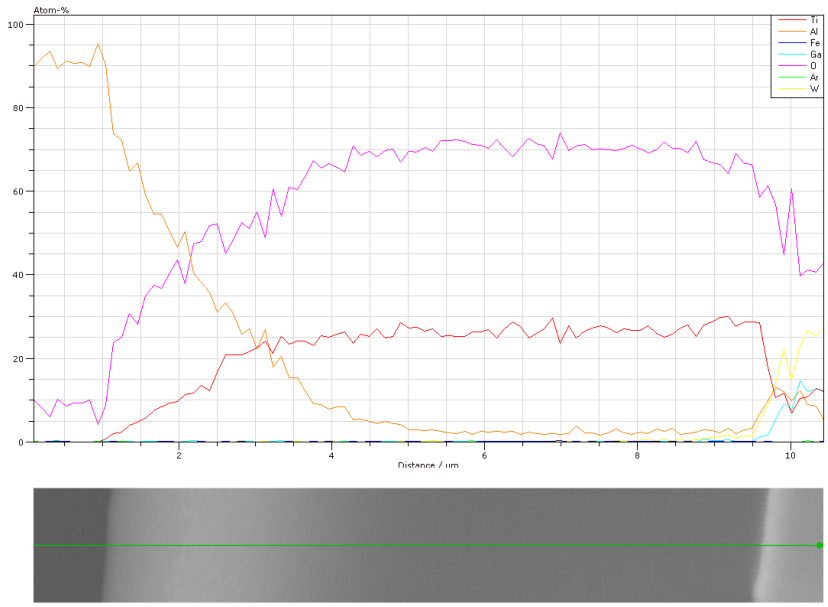

Figure 33 Compositional profile (atomic percentage) of a FIB-milled Fe-TiO_2 TEM specimen

The EDX analysis was repeated after the sample had gone through broad ion beam milling on both sides for 1 minute per side. Figure 34 and Figure 35 are the element mapping and compositional linear profile, respectively, of the sample after this surface polishing. This new set of images support the conclusions drawn from the previous set: that the faces of the specimen are not contaminated with Ga or W, and that the damage layer must be mostly amorphous TiO_2. Were the wedge faces contaminated with another element, one would expect the concentration profile of these elements to decrease due to the etching effect of the broad Ar ion beam on the

surface. Such an effect can be noticed comparing Figure 33 and Figure 35 between 9.50 and 10.25 µm, where the relative concentrations of Ga and W decrease significantly after 1.0 min of surface polishing. The “clean” face of the specimen remains unaffected, as expected under the assumption that Ga and W are absent. The linear profiles shown in Figure 35 also confirms that virtually no Ar ions from the BIB polishing system were implanted into the sample.

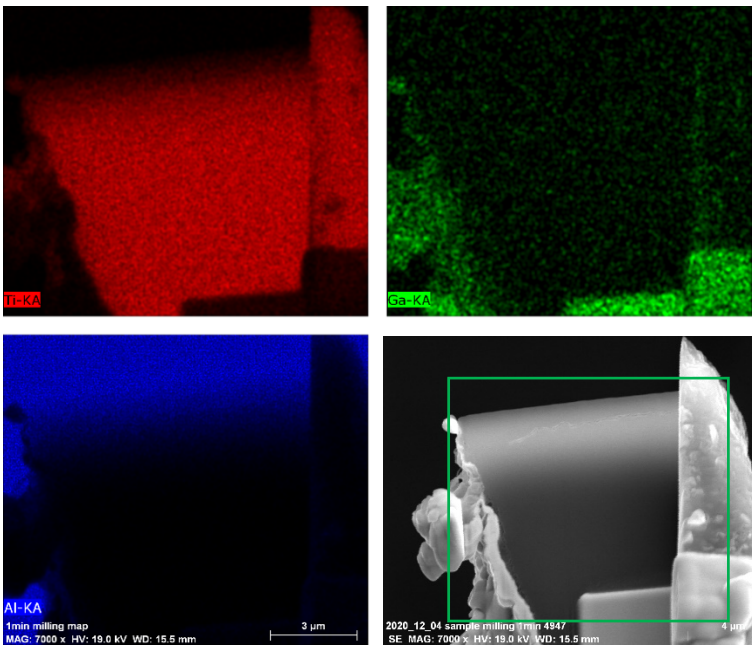

Figure 34 EDX mapping (Ti, Ga, Al) and SE image of a FIB-milled Fe-TiO_2 TEM specimen after surface cleaning using an Ar broad ion beam (1 minute per side)

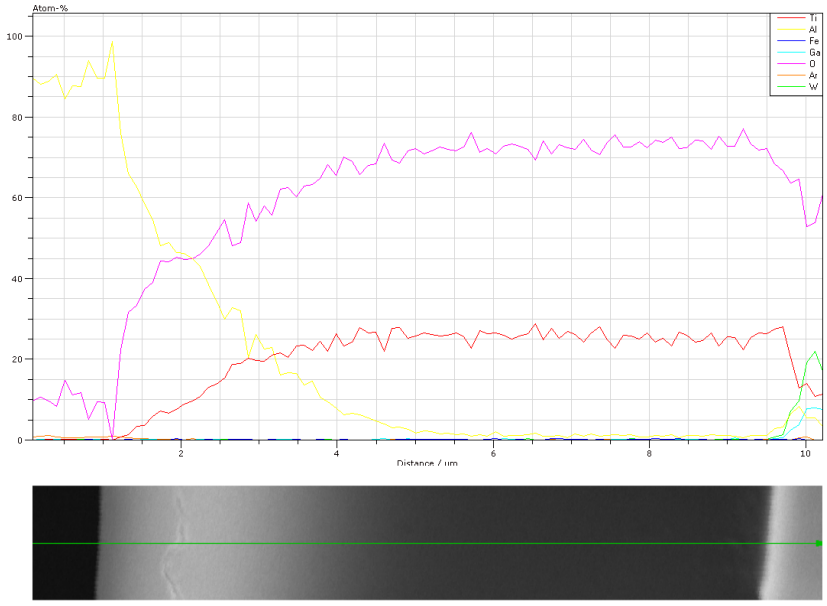

Figure 35 Compositional profile (atomic percentage) of a FIB-milled Fe-TiO_2 TEM specimen after surface cleaning using an Ar broad ion beam (1 minute per side)

With contamination concerns from Ga, W and Ar eliminated, the surface polishing could proceed until the amorphous damage layer was considered completely removed. Figure 36 through Figure 39 are secondary electron images taken in the SEM (Hitachi S-4800) demonstrating the evolution of this process at pre-determined time increments. Each figure contains images of both sides of the specimen. The better contrast of the SEM reveals more clearly the brighter regions, close to the base of the specimen, that could be gleamed in Figure 31. As the surface polishing progresses, it can be observed that this unusual feature recedes into the half-grid prong until it disappears completely from the wedge face after 12.0 min. Due to the SE emission of these bright regions being similar to that of the half-grid prong, it is assumed that its origin is contamination from Cu atoms that sputtered back onto the specimen during the FIB milling step, once the Ga beam reached the substrate. This possibility was not contemplated during previous steps, which caused Cu to be left out during the EDX analyses.

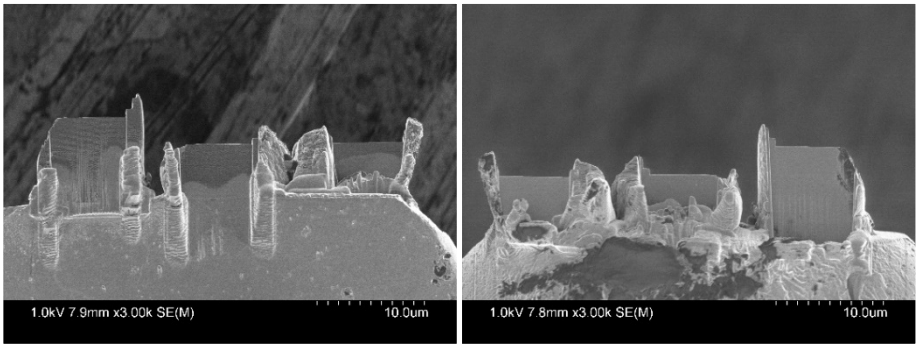

Figure 36 Fe-TiO_2 TEM specimen after milling for 1.5 minutes (total surface polishing time)

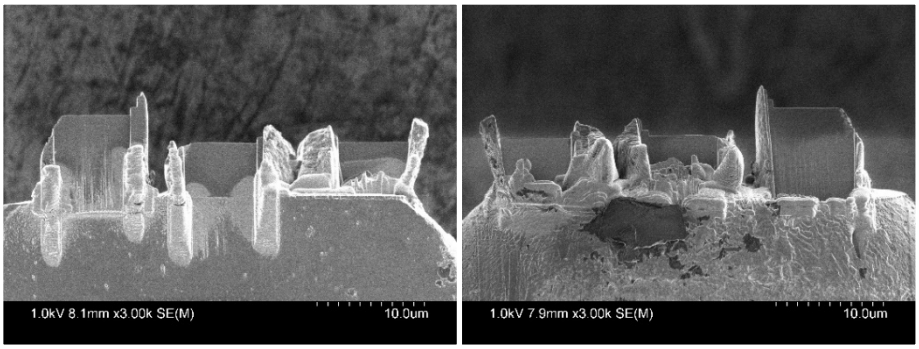

Figure 37 Fe-TiO_2 TEM specimen after milling for 3.0 minutes (total surface polishing time)

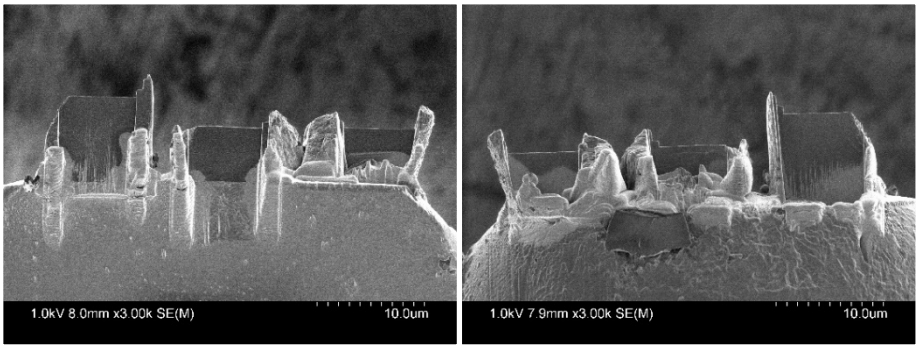

Figure 38 Fe-TiO_2 TEM specimen after milling for 6.0 minutes (total surface polishing time)

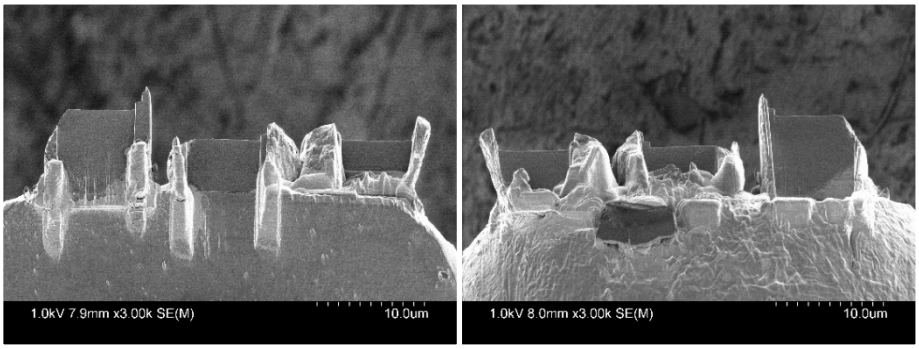

Figure 39 Fe-TiO_2 TEM specimen after milling for 12.0 minutes (total surface polishing time)

Another visible effect of the polishing is the change in the surface texture of the sample. Whereas the initial surface of the wedges' faces was either completely smooth or visibly damaged by the ion beam ("peeling-off" effect), as can be seen in Figure 36, by the end of 12.0 min of polishing the surfaces had acquired a different texture, becoming somewhat homogenously rippled. This effect can be observed in Figure 40, in which the surface details of one of the specimens are shown in higher magnification. This textured state of surface suggests that the broad ion beam is etching the surface in preferential directions. This, in turn, indicates that the amorphous, isotropic damage layer from the FIB milling has been removed and the nano-sized crystallites that compose the polycrystalline sample have been exposed. It is assumed that the amorphous material between grains is etched off preferentially since the highly organized lattice is bonded together more strongly. This rippled texture was the main indicator to stop ion polishing the specimen, as well as the recession of the Cu contamination spots.

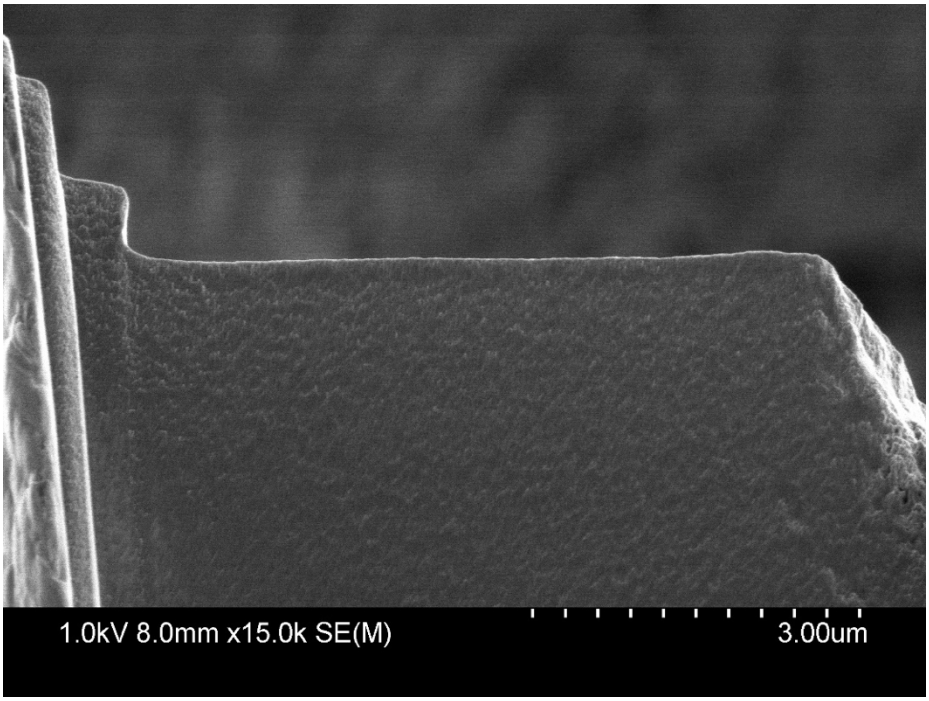

Figure 40 Detail on the surface of a Fe-TiO_2 TEM specimen after milling for 12.0 minutes (total surface polishing time)

3.3.2. High-resolution STEM imaging and EDX

The following figures show images (both SE and BF) of the specimen taken using STEM equipment (Hitachi SU9000) at progressively higher magnification levels. Figure 41 presents the thin edge of the specimen at a magnification of 200k times, Figure 42 at 500k times and Figure 43 at 1000k times. The magnification levels presented here correspond to the capture of the original images, before resizing to fit this document.

The secondary electron images in the Figures reveal details of the surface morphology of the particles, including the complex character of the rippled texture identified before in the low magnification pictures. It can be seen, especially at high magnification levels, that the seemingly straight, sharp edge produced during the specimen preparation protocol is in fact quite irregular.

Due to being obtained by transmission imaging, the bright field images shown in the Figures can yield bulk information on the specimen such as local thickness and density. Near the edge of the specimen, a significant fraction of the electron beam intensity is transmitted through the thinner regions of the material and outlines the crystallites. These transmission images are a valuable first look into the morphology of these nanosized, monocrystalline building blocks that agglomerate to form the larger polycrystalline particles. The high magnification picture (Figure 43) shows that the crystallites are as small as ~10nm, irregular in shape yet approximately round. This agrees with previous results investigating crystallite size by XRD peak broadening at this concentration of Fe dopant [20].

When SE and BF images of the same region are compared side by side, one can verify that the “ripples” and “bumps” on the surface of the specimen, as well as the profile of the specimen’s edge, correspond to the position of crystallites under the surface. This can be most clearly seen in Figure 43: for instance, the specimen’s edge recedes in the spaces in between crystallites, and otherwise closely matches the contour of the crystallites revealed by the BF image. The concavities on the specimen’s surface, seen in the SE images, can also be traced back to the spaces between the outermost monocrystals that form the sample. These observations support the hypothesis that the material in between crystallites (assumed to be mainly amorphous TiO_2, and possibly amorphous iron oxides) was milled preferentially during the surface polishing step.

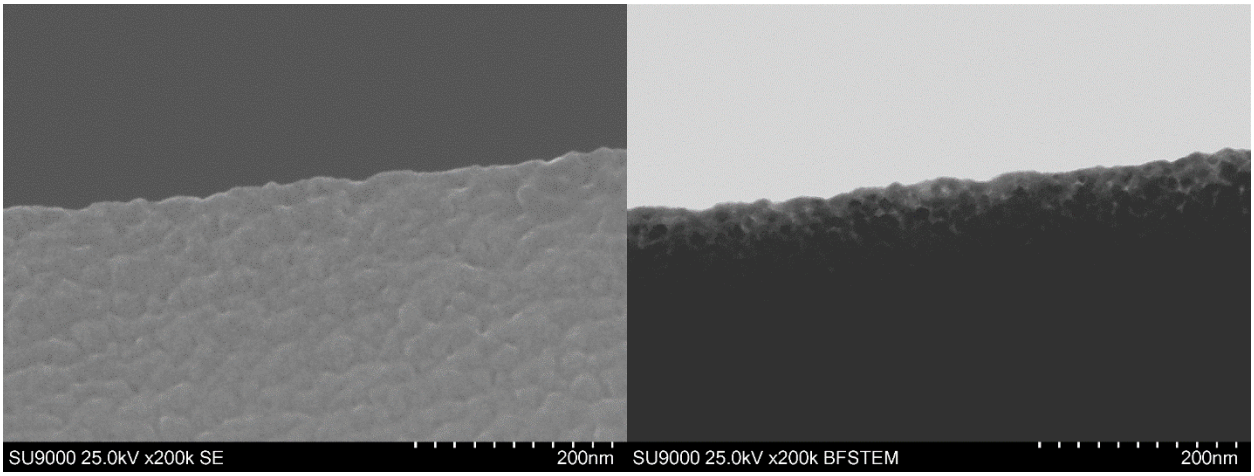

Figure 41 Secondary Electron (left) and Bright Field (right) images of the specimen’s thin edge, taken with a STEM at a magnification of 200kx

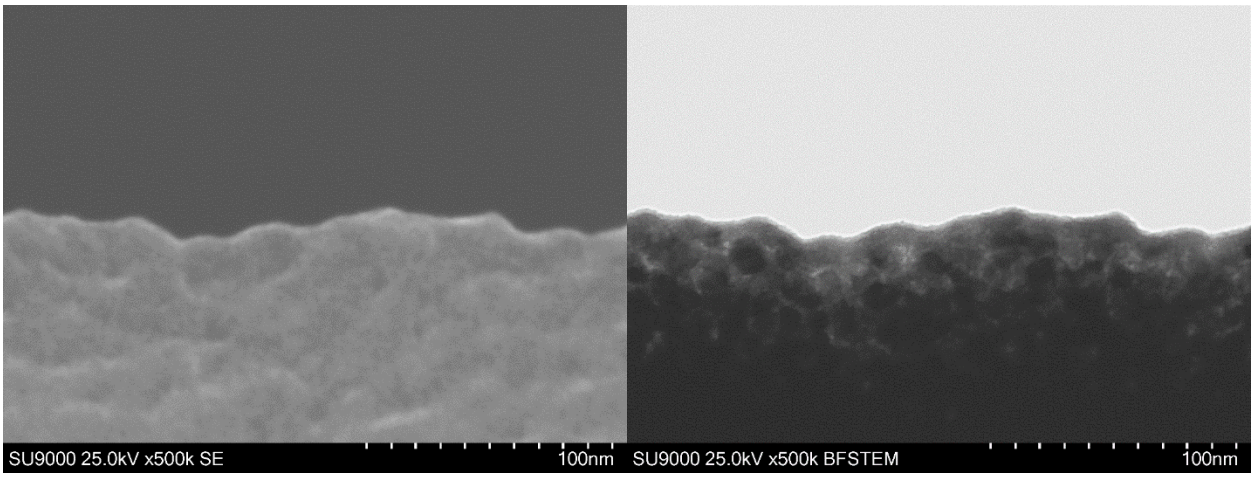

Figure 42 Secondary Electron (left) and Bright Field (right) images of the specimen's thin edge, taken with a STEM at a magnification of 500kx

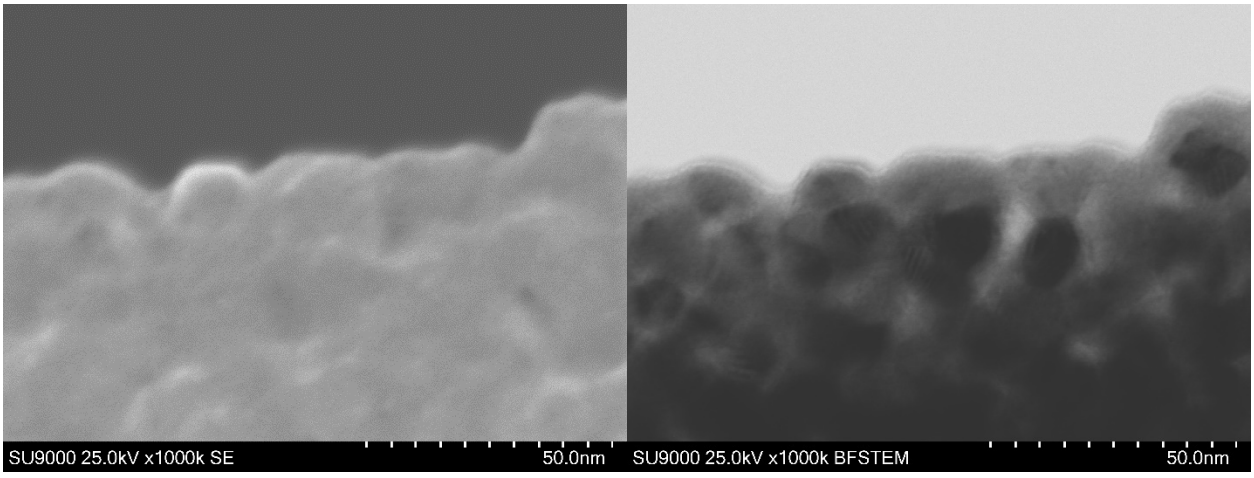

Figure 43 Secondary Electron (left) and Bright Field (right) images of the specimen's thin edge, taken with a STEM at a magnification of 1000kx

Energy Dispersive X-Ray (EDX) compositional analyses were carried in the regions of the specimen's edge indicated in the bright field image shown in Figure 44. Single-point data was collected from the sites labeled as Spectrum 2 and Spectrum 3 (shown in Figure 45 and Figure 46 respectively). The line labeled "Line Data 2" indicates the area where EDX spectra were collected point-by-point to generate a compositional profile along that line (shown in Figure 47).

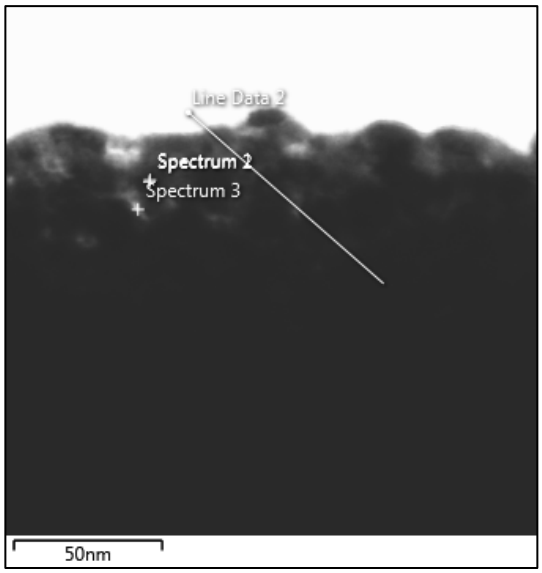

Figure 44 Bright field image of the region of the Fe-TiO_2 specimen's edge where EDX was realized

The single-point spectra were collected in an attempt to verify whether the concentration of Fe in the material in-between crystallites is similar to that inside the crystallites, providing further insight on the possible segregation of Fe as iron oxides inside the particles. The point labeled "Spectrum 2" is centered in a dark circular region of Figure 44, assumed to be a Fe-TiO_2 crystallite. Similarly, the point "Spectrum 3" is centered in a brighter region assumed to be the space between crystallites. The X-ray count data extracted from points "Spectrum 2" and "Spectrum 3" are shown in Figure 45 and Figure 46, respectively.

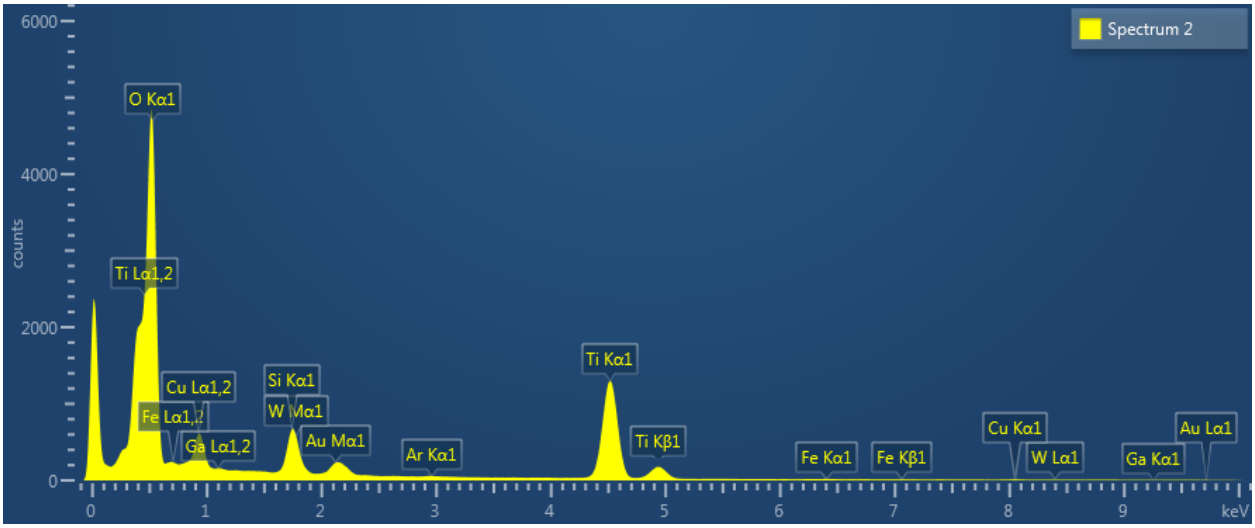

Figure 45 Single-point EDX spectrum of site labeled "Spectrum 2"

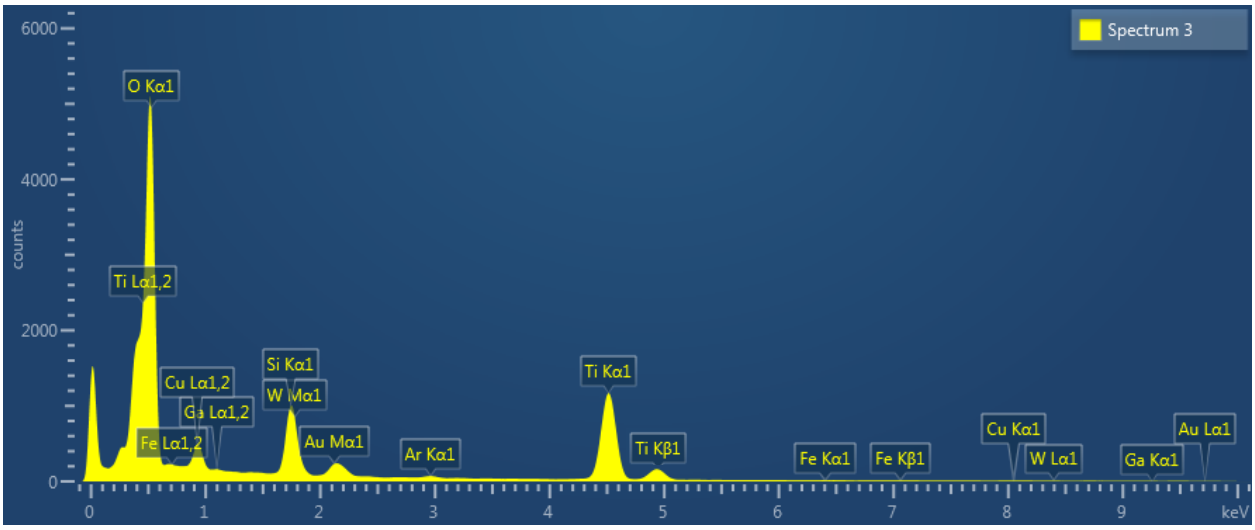

Figure 46 Single-point EDX spectrum of site labeled “Spectrum 3”

Details on different regions of the spectra shown in Figure 45 and Figure 46 are presented in Appendix C (Figure 70 through Figure 77). The peaks that have been labeled correspond to the main elements expected to be found in the specimen: Fe, Ti and O are the components of the photocatalyst that is the object of this study; the TEM half-grid is made of Cu; Ga and W were used in the FIB system to mill and weld the specimen; and an Ar beam was used to polish the surface of the finished specimen. The peaks at approximately 0.11 keV and 1.75 keV may be formed partially by Kα Be and Si emissions, which are elements present in the X-ray detector. As well, it is unclear whether the peak at approximately 2.15 keV is part of the W emissions or if it is partially caused by the electronic transition of specimen holder component component (the Au Mα transition emits at 2.12 keV, for instance).

The relative abundances of each element can be calculated from the ratio of the areas under the respective X-ray emission peaks. For the purpose of finding the relative Fe/Ti ratio present at the surveyed sites, one would integrate the respective Kα emission peaks (Figure 71 and Figure 75 for Ti at 4.50-4.51 keV, and Figure 72 and Figure 76 for Fe at 6.39-6.40 keV) and apply the correction factors corresponding to atomic excitation ratios, self-absorption in the sample and fluorescence of other regions of the specimen. The effects of self-absorption and fluorescence are minimized due to the reduced thickness of the sample. For convenience, Table 9 shows the software-corrected final values of the relative atomic concentrations. The values were normalized for the elements expected to be found in the specimen as a result of the sample preparation method. Table 9 shows data from the single-point analysis of both sites indicated in Figure 44, as well as from the rectangular area shown in Figure 80 (Appendix C) as a reference.

Table 9 Atomic concentrations of elements found in the Fe-TiO_2 specimen in three different regions

Element	*Spectrum 2*	*Spectrum 3*	*Map Sum*
O	72.50%	73.59%	78.21%
Ar	0.06%	0.19%	0.05%
Ti	21.20%	19.21%	15.28%
Fe	0.19%	0.00%	0.16%
Cu	2.74%	2.09%	1.35%
Ga	0.09%	0.08%	0.05%
W	0.22%	0.28%	0.18%
Si	2.55%	4.09%	4.35%
Au	0.45%	0.47%	0.38%
Total	100%	100%	100%

The data presented in Table 9 show that Ar, Ga and W remain in the specimen in trace quantities. As well, the calculated Cu and Si concentrations are significant, but those X-rays are not necessarily generated within the sample: as mentioned before, they originate from the TEM copper half-grid and X-ray detector through weak internal reflections and scattering. The weak concentration of Au can be attributed to the composition of the specimen holder.

Table 9 also indicates that the iron concentration at the site “Spectrum 2” (middle of the crystallite) is slightly higher than at point “Spectrum 3” (between crystallites): 0.19% and 0.00%, respectively. In fact, the calculated concentration of iron at the site “Spectrum 3” falls below the equipment’s detection limit, which explains the apparent absence of this element. In fact, the reduced thickness of the specimen at the “Spectrum 3” point could be the reason why the detector did not capture enough X-ray counts to generate an accurate value for the iron abundance. The lower detection limit for element concentrations is between 0.1 and 0.5% for the equipment used, indicating that the actual iron concentration at “Spectrum 3” is probably around the lower end of that range (0.10%).

The values for iron abundance at sites “Spectrum 2” (0.19%, measured) and “Spectrum 3” (0.10%, assumed) are similar to the average iron concentration surveyed over a larger area, shown under the “Map Sum” column and equal to 0.16%. This initially suggests that Fe atoms are distributed homogenously within the sample. The analysis includes, however, elements that were involved in the sample preparation process and that would not be ordinarily present in the photocatalyst particles. A more accurate value for the iron content can be obtained by normalizing its concentration using Equation 54:

$$Fe\%_{in\ TiO_2} = \frac{Fe\%}{Fe\% + Ti\% + O\%_{stoich}} \qquad \text{Equation 54}$$

which excludes all other elements in the specimen chamber other than those present exclusively in Fe-TiO_2, namely iron, titanium, and oxygen. The oxygen concentration was taken to be the stoichiometric equivalent in TiO_2, that is $O\%_{stoich} = 2 \times Ti\%$, to exclude the contribution of any other native oxides in the system. The non-normalized iron concentration at “Spectrum 3” was

taken to be 0.1%, the assumed lower detection limit for the EDX equipment used. This approach yields the normalized concentrations shown in Table 10.

Table 10 Atomic concentrations of iron found in the Fe-TiO_2 specimen relative to the Fe+Ti content

Collection site	*At% of Fe in Fe-TiO_2*
Spectrum 2	0.298%
Spectrum 3	0.173%
Map Sum	0.348%

These normalized values show that there is little difference in iron concentration between the two points surveyed. Furthermore, the analysis indicates a slight increase in iron within the crystallites, compared to the inter-crystallite region. This result is the opposite of what one would observe if excess iron did segregate as iron oxides towards the inter-crystallite regions.

The EDX point analysis suggests that the regions between crystallites is mainly composed of amorphous TiO_2 and that Fe is homogenously distributed throughout the catalyst's inner structure. However, this preliminary result should be taken with some reservations. The iron concentrations initially calculated in Table 9 fall within the detection limit for this EDX setup, which is around 0.1 to 0.5%. This could significantly increase the errors in this analysis, although one can be certain that the total iron concentration in the regions surveyed does not exceed 0.5%. This result will be further investigated in this study using EDX line analyses and, subsequently, EELS.

The line analysis of the region labeled "Line Data 2" yielded the compositional profile shown in Figure 47. The x-axis represents the position of the data points along the profile line, while the y-axis represents the X-ray counts collected for each element based on their characteristic emissions (4.51 keV for Ti $K\alpha_1$, 0.52 keV for O $K\alpha_1$ and 0.71 keV for Fe $L\alpha_{1,2}$). The direction of the compositional profile was chosen so that the EDX analysis includes dark and bright regions of the specimen, corresponding to the crystallites and spaces between them, respectively. Any differences in the iron content between the dark and bright zones could be an indicator of preferential segregation of iron oxides.

The information presented in Figure 47 does not translate directly to relative element concentrations. Before yielding accurate compositional information, correction factors such as elemental excitation ratios must be considered. Furthermore, the X-ray counts presented refer to the $K\alpha_1$ excitation for Ti and O, while for Fe the $L\alpha_{1,2}$ excitation lines were used. While element ratios cannot be inferred at a first glance, Figure 47 reveals information about the thickness profile of the specimen, not unlike Figure 33 and Figure 35: on thin specimens, the amount of X-ray emissions generated by the electron beam is related to the quantity of material that said beam traverses in the specimen (thickness). It can be observed in the Figure that the overall trend is for the thickness to increase linearly as the data collection advances further towards the base of the specimen, as it is to be expected due to the shape of the sample (wedge with an opening angle of 45°). At this scale, however, it is possible to observe local variations in the overall trend in thickness due to the position of crystallites near the specimen's edge. The specimen thickness clearly increases locally around the center of the crystallites (at 14 nm, 25 nm, 40 nm, etc.) and decreases otherwise (at 18 nm, 32 nm, 48 nm, etc.). This effect is apparently smoothed out after

60 nm into the specimen, as the small crystallite dimensions (around 10 nm) represent an increasingly smaller fraction of the total specimen thickness at the surveyed sites.

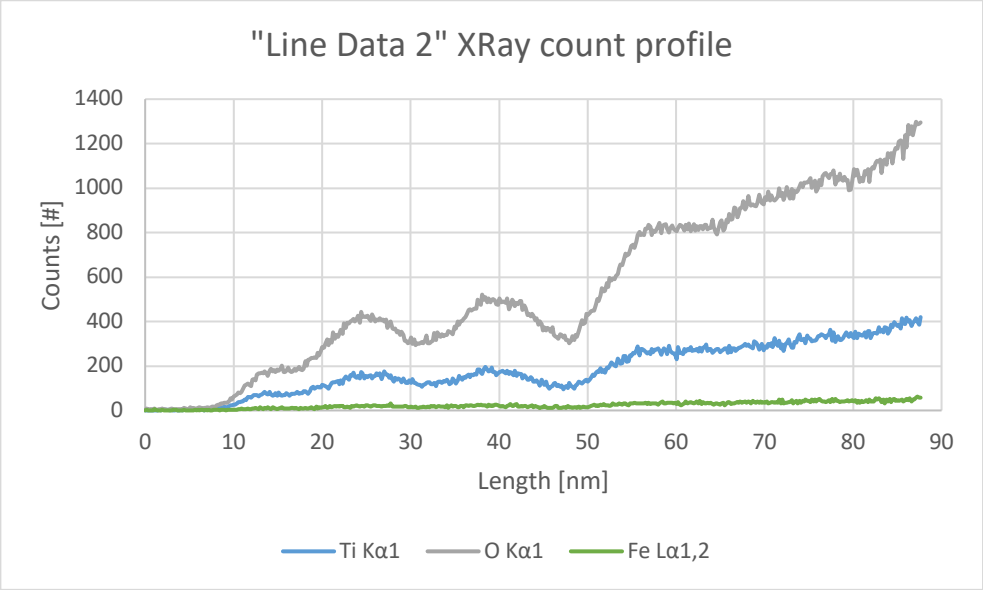

Figure 47 EDX collection profile of Ti, O and Fe along a linear path on the edge of the Fe-TiO_2 specimen

The ratios between X-ray counts for Ti, O and Fe along the linear path “Line Data 2” were plotted in Figure 48. The count ratios are not directly equivalent to the relative concentration of elements in the specimen, as correction factors are required to calculate the latter. However, count ratios are adequate in this situation as the goal of this study is to identify *variations* in the relative abundance of elements in the specimen, without concern for obtaining an accurate measurement of the element concentrations. In Figure 48, the portion of the curves plotted between 0 and 9 nm can be disregarded as that corresponds to background emissions from a region off the edge of the specimen, as seen in Figure 44. The curve representing the Fe/Ti ratio in Figure 48 shows that the relative concentrations of these two elements is quite stable throughout the area surveyed. More importantly, the local variations in the relative abundance of Fe seem to originate from the instrument’s own error since it oscillates rapidly and does not follow the thickness pattern identified in Figure 47. Had Fe segregated to the spaces between crystallites as iron oxides, one would expect to find an increase in iron’s relative count abundance at 18, 32 and 48 nm, which have been identified as regions in-between crystallites. This is yet another indication that iron oxides form only on the surface of Fe-TiO_2 particles during the synthesis process, and not within the particles in the regions between monocrystals.

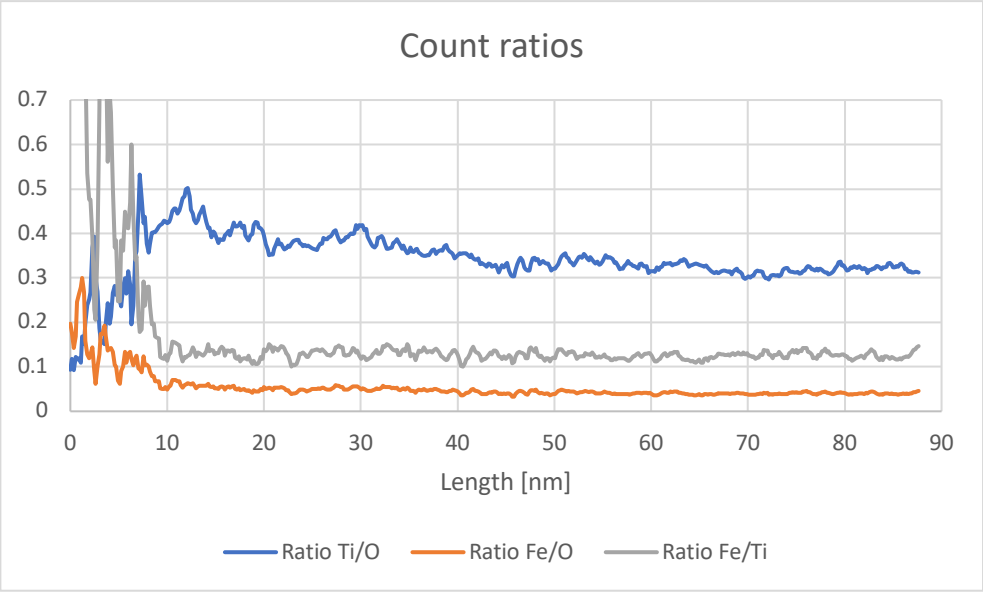

Figure 48 Count ratio profile for the elements investigated by the EDX linear scan shown on Figure 47

As element quantification tools became available later in the duration of this study, actual compositional profiles were generated for the EDX information collected along “Line Data 2”. These profiles are shown in Appendix C. Figure 78 shows the relative atomic concentrations for all elements that could be possibly found in the sample (namely, W, Ga, O, Ar, Ti, Fe and Cu), while Figure 79 shows the normalized atomic concentrations for Ti, O and Fe only. These software-generated compositional profile were left as appended additions to this work because they only support the conclusions drawn from data contained in Figure 47 and Figure 48: that Fe remains at very low atomic concentrations along the direction surveyed by EDX and that its characteristic X-ray emissions do not visibly increase in the inter-crystallite regions of the specimen. This suggests, yet again, that iron oxides do not form preferentially within the inner structure of the polycrystalline Fe-TiO_2 particles.

3.3.3. High-resolution TEM imaging

The following figures (Figure 49 through Figure 51) are high-resolution transmission images of the Fe-TiO_2 specimen at different levels of magnification. They show the material’s structure and morphology in detail, as well as examples of some usual artifacts one may find in transmission images. Figure 49, Figure 50 and Figure 51 were originally magnified 95k times, 200k times and 540k times, respectively, before being resized to fit this document.

Figure 49, shown below, is the least magnified image within this set of transmission images. The thickness contrast in this picture enables the visualization of the Fe-doped anatase crystallites averaging 10 to 20 nm, as well as the brighter gaps between crystallites. This is similar to what was observed in the Bright Field STEM images (Figure 41 through Figure 43), but the higher acceleration voltage used to obtain this image provides much better spatial resolution and contrast. Upon close inspection, one can start observing periodic structures on the crystallites close to the edge, corresponding to the highly organized atomic planes in these monocrystals.

These structures become clearer in the higher magnification images. As indicated in the Figure, one can also observe *Fresnel fringes*. These fringes are formed when part of the electron beam diffracts off an edge and interferes with the direct beam, creating an interference pattern. The large fringes, starting around the periphery of the image and becoming finer towards the center, are Fresnel fringes caused by diffraction off the condenser's aperture edge. There are also Fresnel fringes, although much more subdued, around the edges of all crystallites in the image. This helps visualizing individual crystallites and it can be more clearly seen around those located at the edge of the specimen.

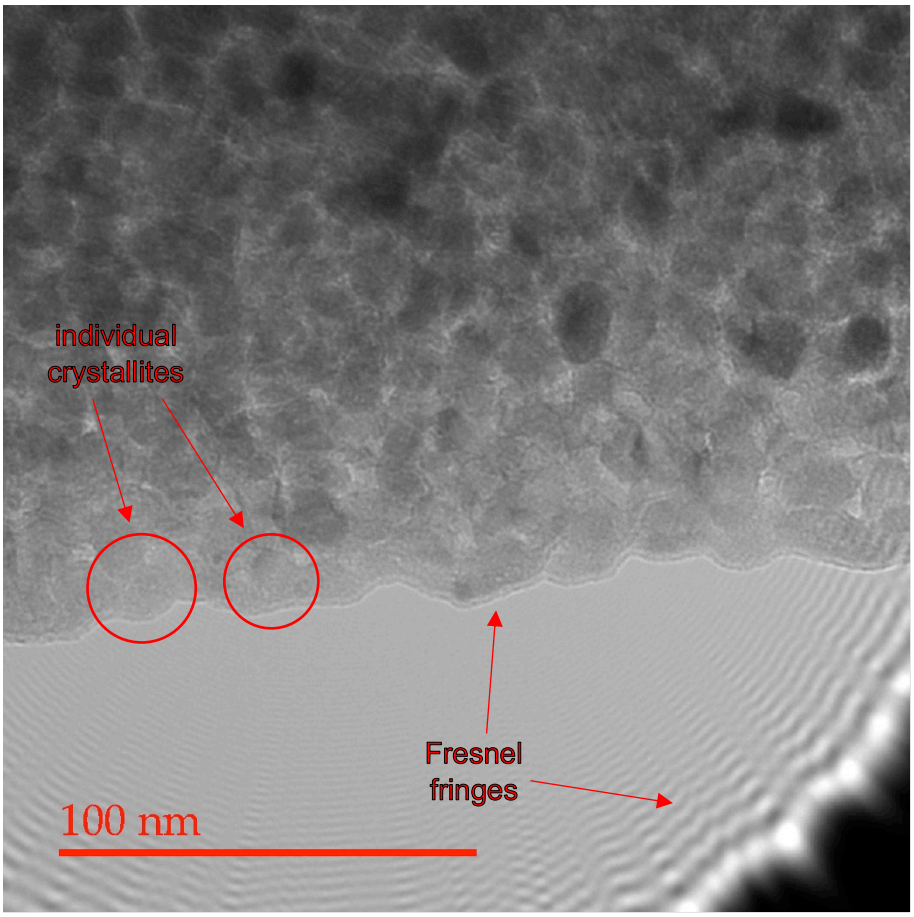

Figure 49 STEHM transmission image of the edge of the Fe-TiO2 specimen (original magnification: 95,000 times)

Figure 50 provides a higher magnification view of the edge of the sample. The periodic structures indicated in the Figure are the atomic planes that can be seen from this lattice orientation (zone axis) of individual monocrystals. At this magnification, this is the main indicator of the bounds of each crystallite, as the image contrast does not outline the crystallite edges as clearly as on previous pictures. The difference between the highly organized crystalline structure of the anatase lattice and the fuzzy, disordered zones in-between starts to become clear. In these spaces between crystalline regions, one observes only short-range order or no organization at all, supporting the assumption that inter-crystallite space is filled with amorphous material that did not crystallize during the crystal growth step. This will be verified later through Fourier and diffraction images of the specimen. Another artifact that can be seen in Figure 50 is a low-frequency periodic

pattern located at the top of the image. These fringes are too far apart to correspond to any of the interplanar spacings of anatase: their period is around 9.3 Å, while for anatase the largest interplanar distance that diffracts is 3.53 Å (for both the {101} and {011} orientations) [111]. Possible explanations for this pattern include Moiré fringes, which can be caused by interference from two overlapping diffracting structures (in this case, the lattice), and thickness fringes, resulting from interference based on the extinction distance of the material associated with varying thickness.

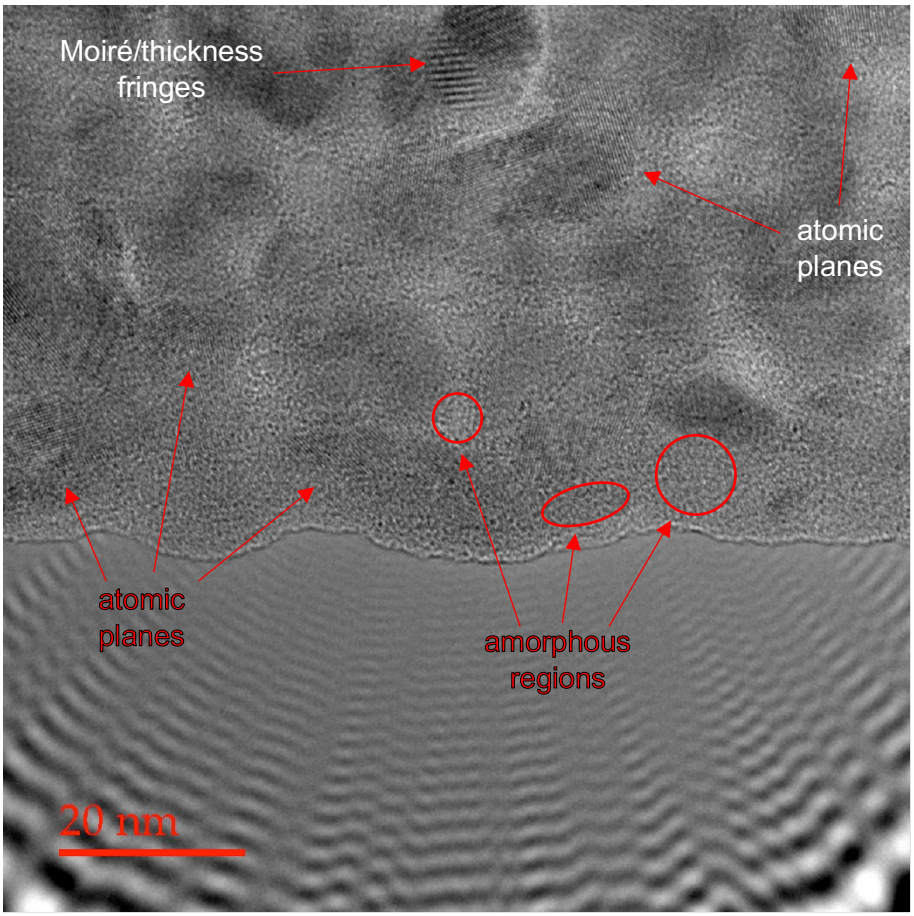

Figure 50 STEHM transmission image of the edge of the Fe-TiO_2 specimen (original magnification: 200,000 times)

Figure 51 reveals, in great detail, the lattice structure of the crystallites in the specimen. Where more than one periodic structure can be identified within the same crystallite, each “direction of repetition” represents a different family of atomic planes. The various sets of planes can be easily identified by generating a Fourier-transformed image of the lattice (a *Fourier image*), which will be done at a later stage. It can be seen, in the Figure, that most of the specimen surface shows some degree of organization into a crystalline lattice. Some areas are clearly and completely crystalline, as indicated in the Figure, but weak periodic structures can be identified even in regions that appear amorphous (“fuzzy”) at a first glance. This observation can have two explanations: it might be a consequence of the specimen fabrication process, where the multiple milling and polishing steps could have damaged the pre-existing lattice; or it might be an indication that the original amorphous TiO_2 in these regions is in the initial steps of crystallization, in which

case a longer calcination time during synthesis would favor the formation of a fully crystallized structure. Another interesting observation from Figure 51 is the presence of two juxtaposed crystallites that might have started merging during specimen preparation, as indicated in the Figure. The grain boundary between the crystallites can be clearly seen as some of the atomic planes on each side of the boundary are misaligned. However, there seems to be some continuity for the set of planes indicated in the Figure by red lines (oriented close to the vertical direction), suggesting that these crystallites have started merging during the calcination step in synthesis. This phenomenon arises from the tendency of crystallites to assume a relative orientation that minimizes the energy of the system by reducing lattice strain and interfaces. Moreover, it has been reported that individual crystals undergo rigid-body rotation, in a process mediated by dislocations, to re-align themselves [112]. The lattice mismatch can be easily calculated from Fourier images, which will be introduced later on.

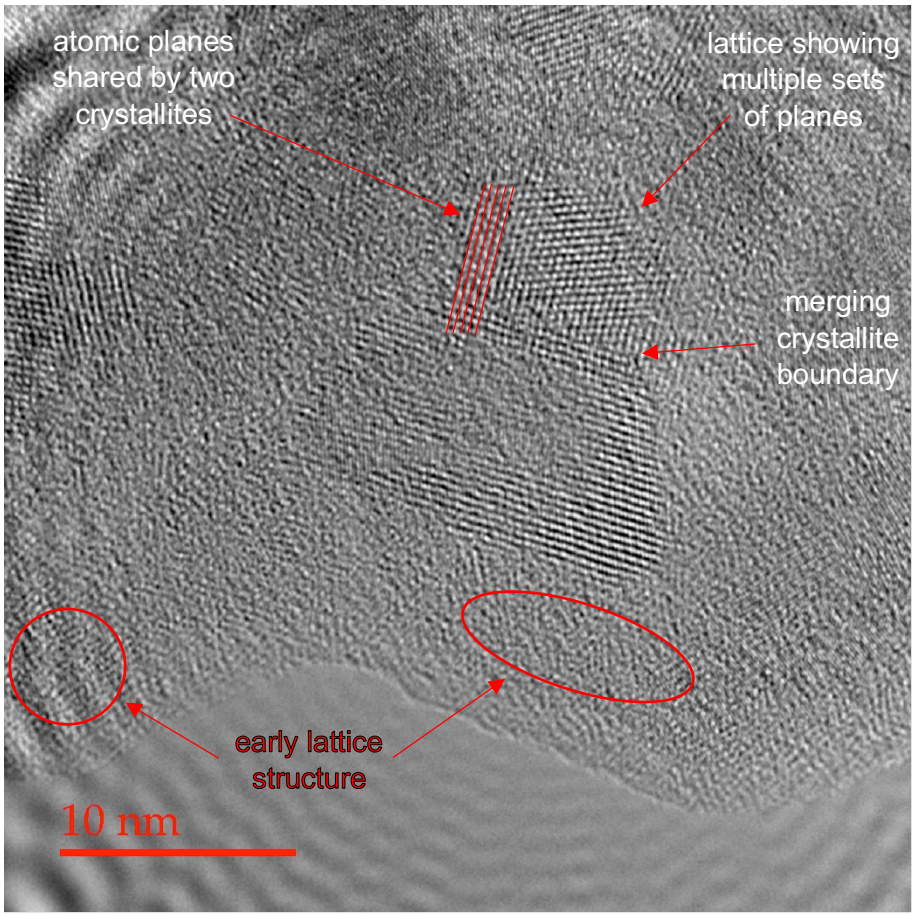

Figure 51 STEHM transmission image of the edge of the Fe-TiO_2 specimen (original magnification: 540,000 times)

The morphology of crystallites can be gleaned from the transmission images presented above, but obtaining an even clearer view of the monocrystals' outline is still possible. This can be done by collecting the electron beam intensity diffracted off certain crystalline planes, while filtering out the rest of the beam intensity. The methodology for this technique is as follows: Figure 52 shows the ring pattern resulting from diffraction of the electron beam through a polycrystalline region of the specimen. Each of the bright dots in the ring pattern is created by intensity diffracted off a

monocrystal, oriented in such a way that a family of its atomic planes fulfills Bragg's diffraction conditions. The rings are formed by the multiple crystals in the specimen, with different orientations, diffracting off the same set of atomic planes according to Bragg's law. By selecting a specific bright spot on the ring diffraction pattern using an objective aperture, and then switching the microscope configuration back to imaging mode, one can visualize the crystals that contribute to the selected diffracted intensity. This procedure is illustrated in Figure 53, where the system's configuration is represented in a simplified way.

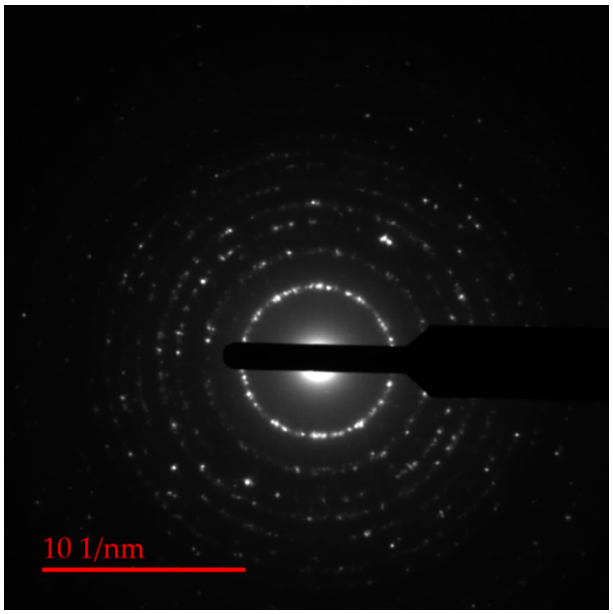

Figure 52 Ring pattern produced from the diffraction of the electron beam through a polycrystalline region of the Fe-TiO_2 specimen. The transmitted beam at the center is partially covered to enable visualization of the weaker, diffracted beams

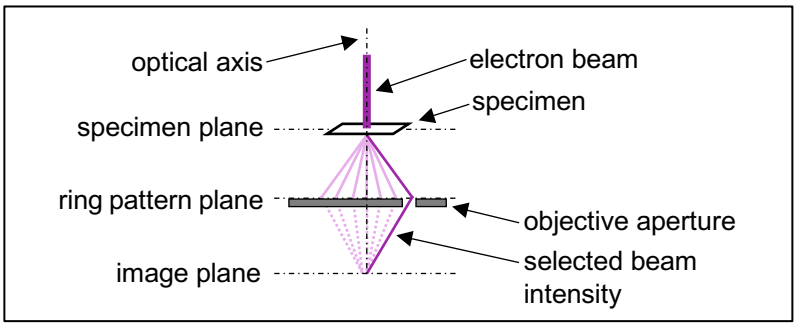

Figure 53 Simplified illustration of the methodology used for selecting diffracted beams with an objective aperture

The result of this technique is shown in Figure 54 through Figure 56. Figure 54(a) and Figure 55(a) show the objective aperture being used to select certain diffracted beams from the ring diffraction pattern shown in Figure 52. Figure 54(b) and Figure 55(b) show how certain crystallites (those whose atomic planes contribute to the diffracted intensities previously selected) are highlighted in "imaging mode" due to the use of the objective aperture. Figure 56 shows the same methodology applied to a larger region of the specimen, without explicitly indicating the diffracted beams selected from the ring pattern.

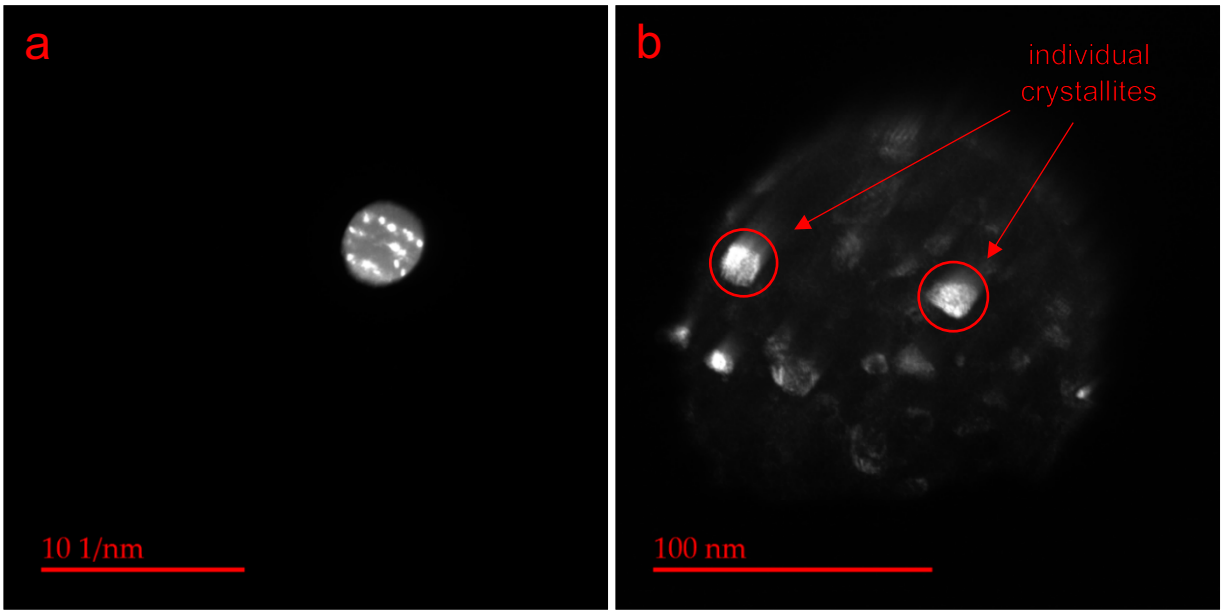

Figure 54 Objective aperture being used on the Fe-TiO_2 specimen to (a) select diffracted beams from a ring diffraction pattern and (b) highlight crystallites contributing to the selected diffracted intensity

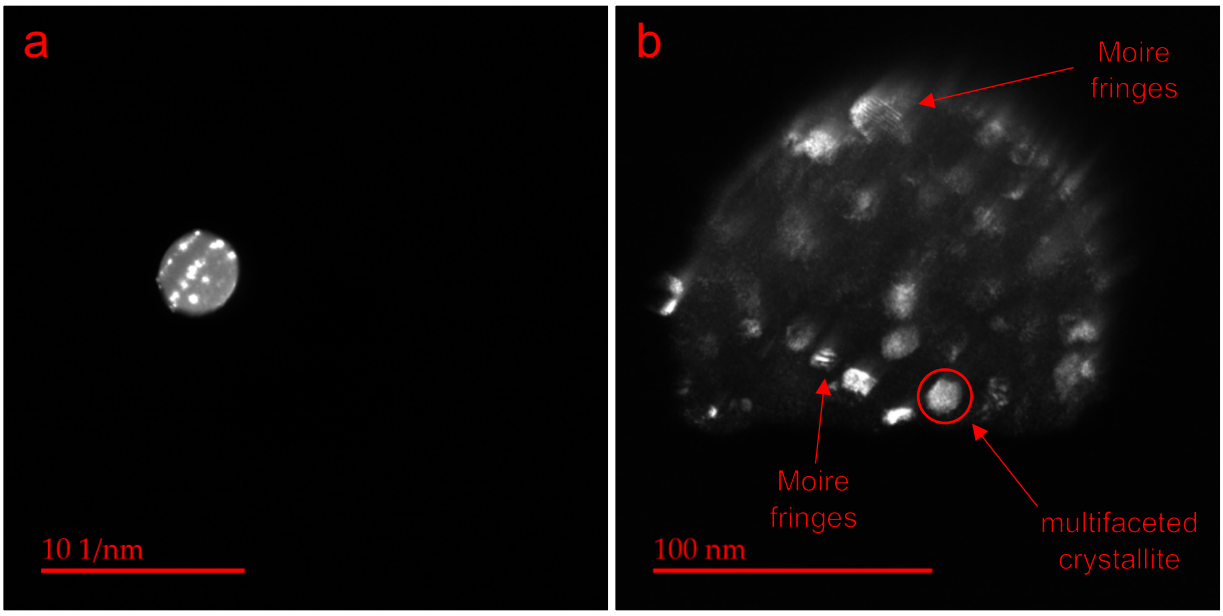

Figure 55 Objective aperture being used on the Fe-TiO_2 specimen to (a) select diffracted beams from a ring diffraction pattern and (b) highlight crystallites contributing to the selected diffracted intensity

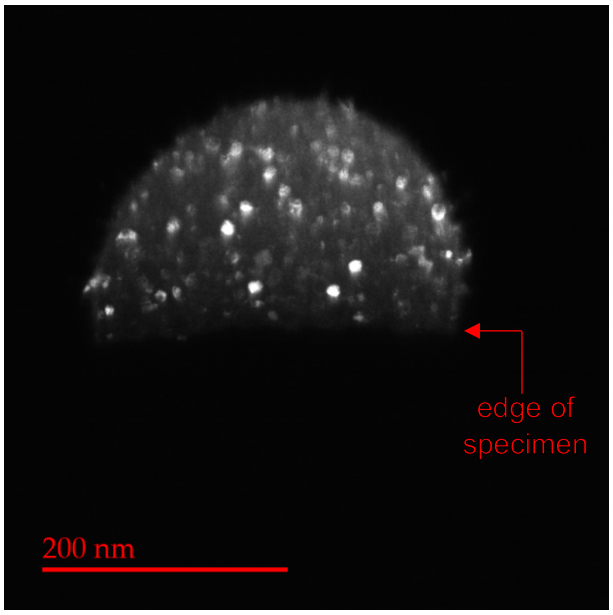

Figure 56 Transmission image of the edge of a Fe-TiO_2 specimen where an objective aperture was used to filter out part of the diffracted beam intensity, highlighting individual crystallites

This use of the objective aperture reveals more details of the outline of the crystallites than previous transmission images. Against a dark background, individual crystallites are seen as multifaceted particles with clearly defined edges. It becomes clear that, despite being approximately circular at a first glance, most of the monocrystals have clean faces and sharp angles as illustrated by the roughly hexagonal crystal indicated on Figure 55(b). Moiré fringes, caused by the overlap of multiple periodic structures (in this case, the lattices from multiple monocrystals), can also be observed in this type of images as seen in Figure 55(c).

Due to the polycrystalline character of the Fe-TiO_2 specimen, obtaining spot diffraction patterns is challenging because one must be sure to focus the electron beam on a predominantly monocrystalline region. This issue can be averted by taking a transmission image of a larger region of the specimen, manually selecting seemingly monocrystalline zones, and digitally applying a Fourier Transform (FT) over the selected area. The image thus generated, a *Fourier image* (FT-image), is equivalent to a spot diffraction pattern as it represents the frequencies of all periodic structures in the original image as individual points, analogous to how a set of repeating atomic planes would generate a single diffracted beam.

Figure 57 shows a transmission image from a polycrystalline region of the specimen (center of the Figure), from which several Fourier images were generated. The green squares indicate the sub-regions where the FT operators were applied. A combination of seemingly crystalline (sub-images a and c), amorphous (sub-image b) and partially crystalline (sub-images d and e) regions were chosen in order to illustrate the range of Fourier images that can be obtained in terms of different crystallinities. The bright dots in the FT-images correspond to periodic features whose frequency (in nm) is the reciprocal of the distance (in 1/nm units) between the dot and the center of the image (which is analogous to the transmitted beam). In the context of crystallography, this spatial frequency is the measure of the lattice's interplanar spacing ("d-spacing"). Bright spots farther from the center of the FT-image arise from atomic planes with smaller d-spacings, and

vice-versa. The magnitude of the beam intensity in the FT-images, both for the bright dots and scattered intensity, indicate the magnitude of the periodicity of the structures represented.

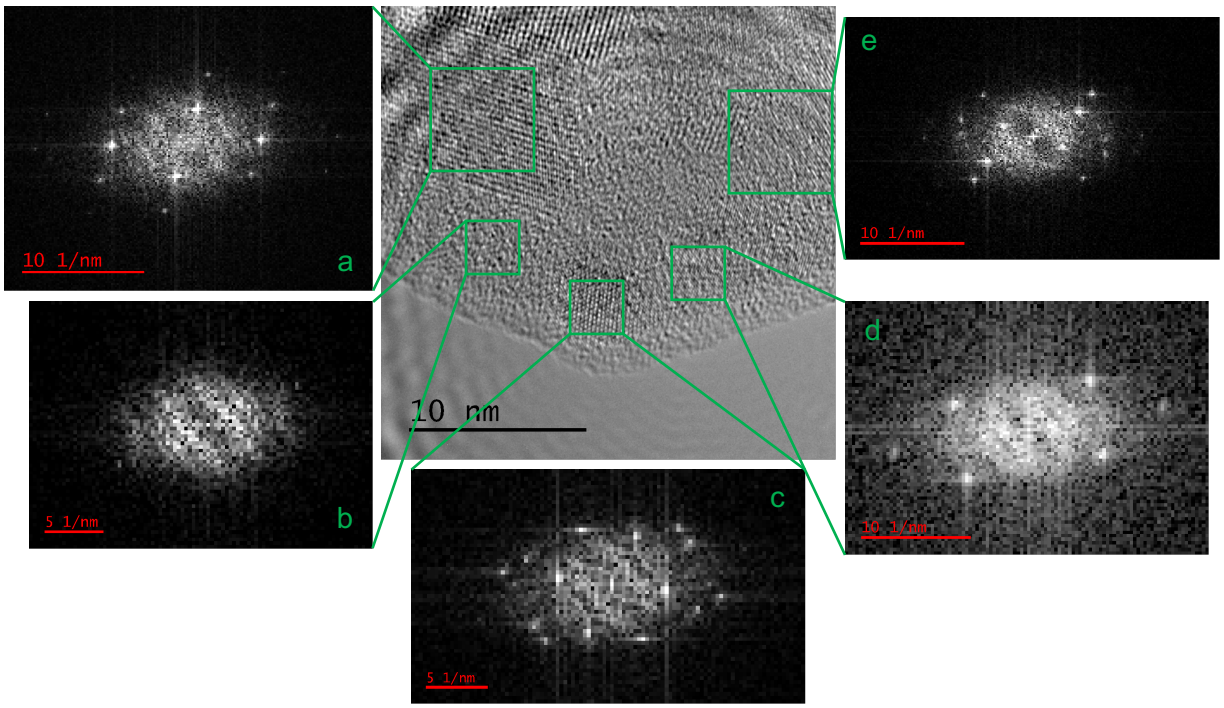

Figure 57 Transmission image of the Fe-TiO_2 specimen (center), surrounded by FT-images of selected regions ((a) through (e), indicated by the green squares)

Figure 57(a) through (e) show very distinct spot diffraction patterns. For some of them, the diffracted spots are organized with a high degree of symmetry, such as in region (a). This indicates that the crystallite is oriented in such a way that the electron beam is aligned along its *zone axis*, which is a direction generally defined by the intersection of two lattice planes with high atomic density. In region (b), on the other hand, there is hardly any organization to the intensity shown in the FT-image, strongly suggesting that region of the specimen is completely amorphous. It might seem counter-intuitive, at first, that amorphous material would appear on FT-images since it does not have periodic structures to diffract the transmitted electron beam. The amorphous regions possess, in fact, *short-range order*: a miscellanea of orientations and atomic planes diffusely scattering the beam. This explains the diffuse, "speckled" intensity present in Figure 57(b). The same "cloudy" noise is present in all other diffraction patterns, reaching out from the center of the images to the main peaks, which indicates that there are "amorphous planes" with varying frequencies that could possibly nucleate crystalline material. The remainder of the FT-images (c through e) are neither completely amorphous nor clearly oriented along one of the lattice's zone axes.

Crystallography information was extracted from Figure 57(a) in order to characterize the specimen. This particular FT-image was chosen because the crystallite is oriented along a zone axis of the lattice, providing a high-symmetry diffraction pattern that is more trivial to interpret. The reciprocal lattice vectors $\vec{g}_{(hkl)}$, connecting the center of the FT-images and the diffracted spots, have the following properties [113]:

1. Its direction is normal to the plane (hkl) of the crystal lattice.
2. Its magnitude is $^1/_{d_{(hkl)}}$, where $d_{(hkl)}$ is the interplanar spacing of the (hkl) family of planes.

Figure 58 is the FT-image from the specimen region shown in Figure 57(a). The annotations show the two first-order diffracted beams present in this image, indicated by $\vec{g}_1$ and $\vec{g}_2$, as well as the angle ϕ between them. All other sets of planes represented by bright spots in Figure 58 stem from the linear combination of $\vec{g}_1$ and $\vec{g}_2$. The exception is the pair of bright spots close to the center (indicated in the image), which are caused by the large Fresnel fringes seen in Figure 57.

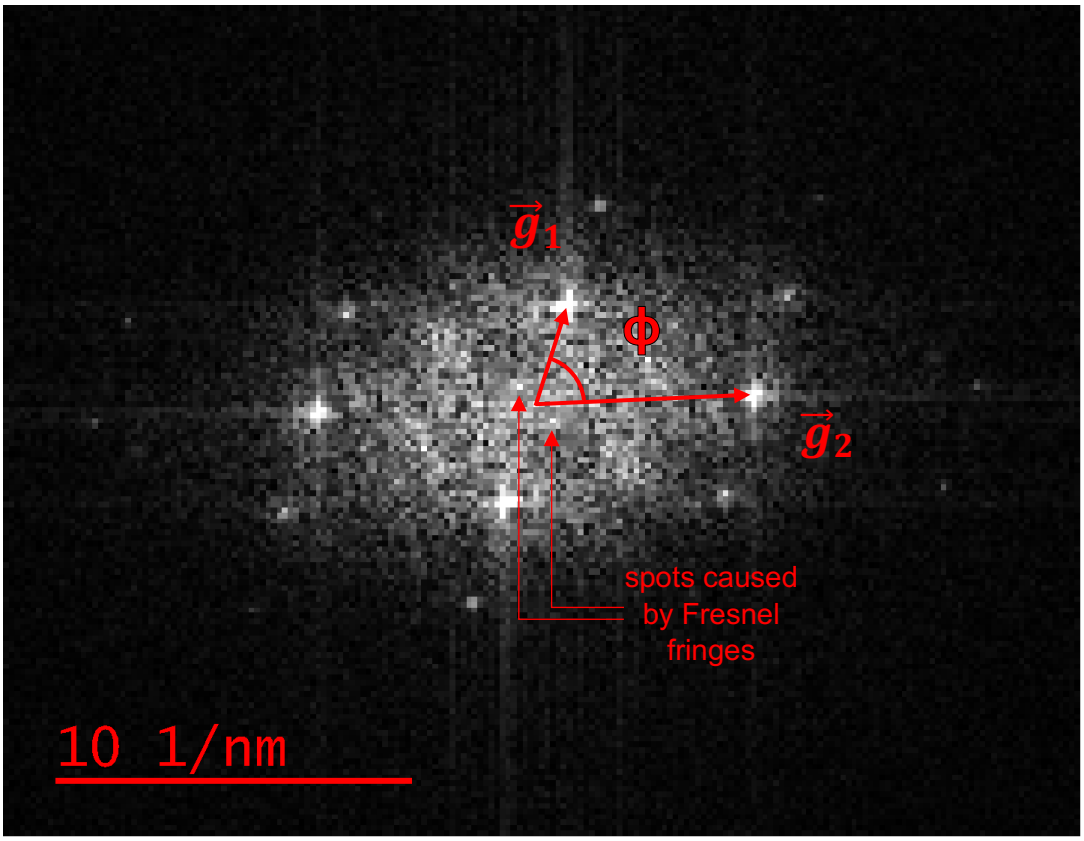

Figure 58 Fourier image of a Fe-TiO_2 crystallite oriented along a zone axis. The reciprocal lattice vectors for first-order diffractions are indicated in the image, as well as the angle between them

Table 11 shows the measured magnitudes of $\vec{g}_1$ and $\vec{g}_2$, as well as the reciprocal of said magnitude and the angle between the two reciprocal lattice vectors. The error in the measurement of the magnitude of $\vec{g}_1$ and $\vec{g}_2$ results from the pixel size, namely $0.16\frac{1}{nm} \times 0.16\frac{1}{nm}$.

Table 11 Measured magnitude of the reciprocal lattice vectors, their reciprocal magnitudes indicating interplanar spacing, and measured angle between them

$\|\vec{g}_1\|$ $[^1/_{nm}]$	$^1/_{\|\vec{g}_1\|}$ [Å]	$\|\vec{g}_2\|$ $[^1/_{nm}]$	$^1/_{\|\vec{g}_2\|}$ [Å]	ϕ [°]
2.86 ± 0.16	3.4965	5.86 ± 0.16	1.7065	70.497

With these values, one can attempt to index the diffracted spots in Figure 58 using crystallographic information for anatase titania found in the literature. Appendix D compiles such information such as main XRD peaks (Figure 86), interplanar spacings for the main diffracting atomic planes (Table 14), and a list of possible interplanar spacings for the anatase lattice with Miller indices and XRD angles (Table 15). XRD peak information is useful because it reveals which atomic planes diffract strongly due to factors such as atomic density within the plane, indicating which planes are likely to be found in diffraction patterns. The theoretical interplanar spacing $d_{(hkl)}$ for a set of planes (hkl) is calculated using Equation 55 shown below, where h, k and l are the Miller indices and a, b and c are the lattice parameters (magnitude of the primitive translation vectors) for the anatase unit cell [113]. Once candidates for the family of atomic planes associated with $\vec{g}_1$ and $\vec{g}_2$ have been selected, one can compare the measured angle between vectors with the theoretical angle between planes, given by Equation 56 also shown below. This equation is a variation of the vectorial relationship $\cos(\vec{x}\angle\vec{y}) = \frac{\vec{x}\cdot\vec{y}}{\|\vec{x}\|\|\vec{y}\|}$, but corrected for the fact that the primitive translation vectors for the anatase unit cell are not orthonormal ($a = b \neq c$). Table 12 shows probable candidates for the orientations represented by $\vec{g}_1$ and $\vec{g}_2$, as well as a comparison between measured and theoretical parameters.

$$\frac{1}{d_{(hkl)}^2} = \frac{h^2 + k^2}{a^2} + \frac{l^2}{c^2} \qquad \text{Equation 55}$$

$$\cos\phi = \frac{\frac{1}{a^2}(h_1h_2 + k_1k_2) + \frac{1}{c^2}l_1l_2}{\left[\left\{\frac{1}{a^2}(h_1^2 + k_1^2) + \frac{1}{c^2}l_1^2\right\}\left\{\frac{1}{a^2}(h_2^2 + k_2^2) + \frac{1}{c^2}l_2^2\right\}\right]^{1/2}} \qquad \text{Equation 56}$$

Table 12 Probable lattice orientations for $\vec{g}_1$ and $\vec{g}_2$ and comparison between experimental and theoretical values

	$\vec{g}_1$	$\vec{g}_2$
Proposed Orientation	(101)	(015)
$\|\vec{g}\|$	$2.86 \pm 0.16\ nm^{-1}$	$5.86 \pm 0.16\ nm^{-1}$
Theoretical $\|\vec{g}\|$	$2.8333\ nm^{-1}$	$5.8655\ nm^{-1}$
$d_{(hkl)}$	3.4965 Å	1.7065 Å
Theoretical $d_{(hkl)}$	3.5394 Å	1.7049 Å
Measured ϕ	$70.497°$	
Theoretical ϕ	$70.692°$	

The candidate crystal orientations for $\vec{g}_1$ and $\vec{g}_2$ shown in Table 12 were chosen based on the information provided in Table 14 and Table 15. The experimental interplanar spacings inferred from $\|\vec{g}_1\|$ and $\|\vec{g}_2\|$ are quite close to the expected theoretical values for the (101) and (015) crystallographic orientations, especially when one considers that the error in those measurements (due to the FT-image pixel size) overlaps the theoretical values for $\left\|\vec{g}_{(101)}\right\|$ and $\left\|\vec{g}_{(015)}\right\|$. The angle between these vectors is also a close match, ensuring that $\vec{g}_1$ and $\vec{g}_2$ are, in fact, $\vec{g}_{(101)}$ and $\vec{g}_{(015)}$ respectively. Other sets of planes with similar interplanar spacings and strong diffractions, such as the (211) orientation with $\boldsymbol{d}_{(211)} = 1.6726\,\text{Å}$, for instance, are ruled out due to the mismatch of angle between $\vec{g}_1$ and $\vec{g}_2$. Another consideration is that both $[(101), (015)]$ and $[(011), (105)]$ are solutions for this data set due to the symmetry of the lattice ($a = b$). However, neither $[(101), (105)]$ nor $[(011), (015)]$ are solutions because the angle between those orientations is $41.62°$, calculated using Equation 56.

With the crystallographic orientations determined, the bright diffraction spots from Figure 57(a) can be indexed. This is shown in Figure 59, where the lattice orientations are annotated next to the diffraction spots in the FT-image, and the reciprocal lattice vectors are not shown for ease of visualization.

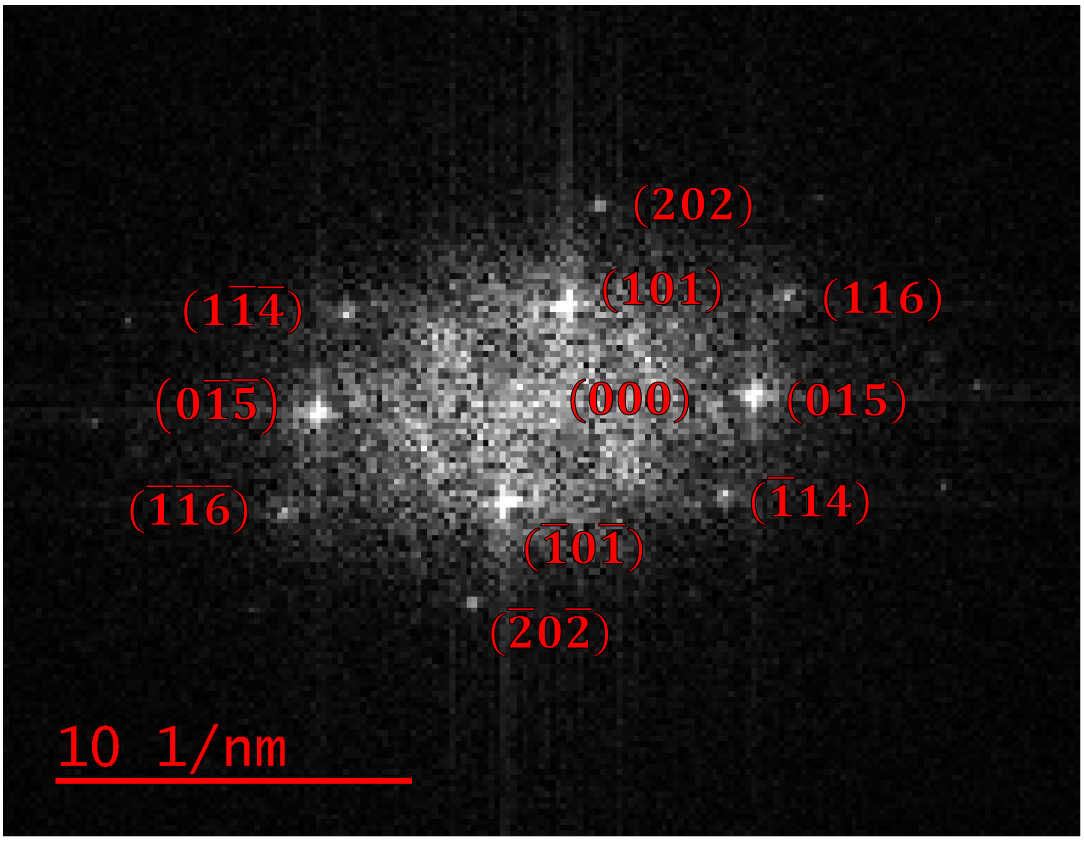

Figure 59 Fourier image of the Fe-TiO_2 specimen, where the diffraction spots have been indexed according to the crystallographic orientation they represent

The zone axis of the crystallite can be calculated using the crystallographic orientations shown in Figure 59. Its direction is indicated by the vector $\vec{B}$, perpendicular to the plane of the Figure. The vector $\vec{B}$ can be calculated by finding the cross product of $\vec{g}_1$ and $\vec{g}_2$, as shown below [113]:

$$\vec{B} = \vec{g}_{(101)} \times \vec{g}_{(015)} = (\bar{1}\bar{5}1)$$

The use of FT-images is a powerful tool to interpret crystallography information that might not be evident at a first glance, such as the crystal misalignment indicated in Figure 51. By applying a Fourier Transform to the individual crystals that seem to be in the process of merging, one can calculate the lattice mismatch in the plane of the Figure. This is shown in Figure 60. The original transmission image is shown on the left (a), with green boxes indicating which areas were used to generate the Fourier images on the right (b and c). Figure 60(b) corresponds to the top crystallite on the transmission image, while Figure 60(c) corresponds to the bottom one. Although some degree of symmetry can be identified in both FT-images (distorted hexagon in (b) and distorted square in (c)), it is safe to assume that the crystallites are not oriented along a zone axis since the diffraction patterns are not *highly symmetrical* as in Figure 57(a). The (101) crystallograpic orientation, indexed through the calculation of $1/\|\vec{g}\|$, is shown on the FT-images. The lattice mismatch between both crystals for this set of atomic planes can then be measured as roughly 15 degrees.

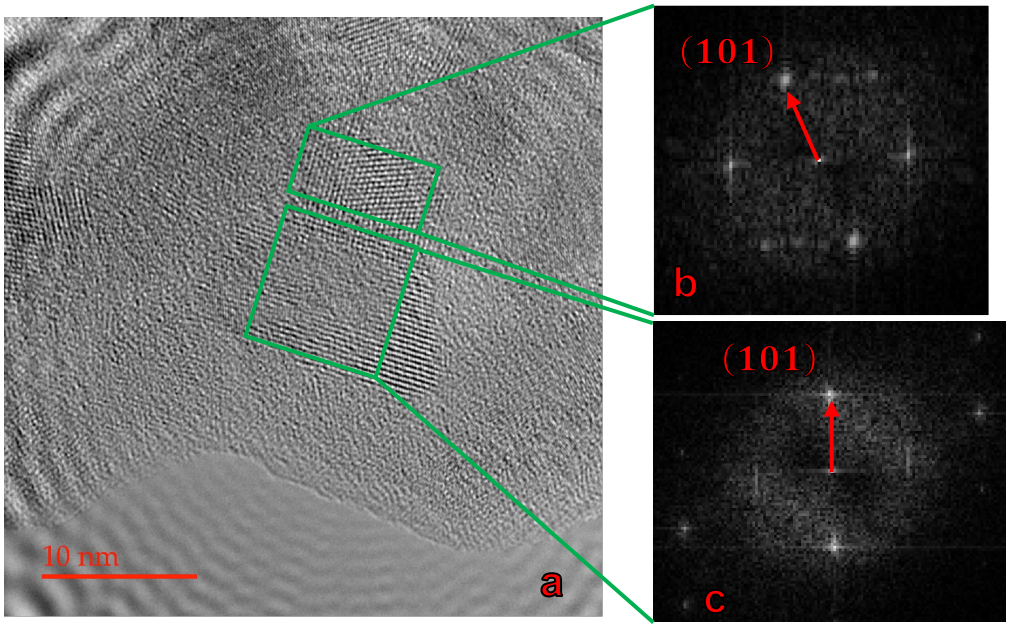

Figure 60 Transmission image (a) of two crystallites seemingly merging, with Fourier images indicating the crystal orientations that allow the calculation of the lattice mismatch (b and c)

It has been said previously that due to the polycrystalline nature of the specimen, diffraction patterns that are generated from the scattering of the electron beam (as opposed to those digitally generated by Fourier Transforms) are likely to be *ring diffraction patterns*. This happens since the electron beam is likely to be diffracted by several crystallites in the specimen, and not by a single monocrystal which would generate a *spot diffraction pattern* equivalent to FT-images. This is, of course, dependant on the size of the electron beam spot and the specimen area surveyed. A ring pattern was show in Figure 52 to aid the contrast imaging of individual crystallites. The same pattern can be used from a crystallography perspective to identify the sets of atomic planes that are diffracting the electron beam. This is done according to the same principle used to index Figure 58: that the distance between the transmitted and diffracted beams, in $1/nm$ units, is the

reciprocal of the interplanar spacing of the family of atomic planes that generated the diffracted beam in question.

Figure 61 shows a ring diffraction pattern (the same one introduced in Figure 52) where the ring diameters have been measured and annotated on DigitalMicrograph. It was found later that the scale bar provided by the STEHM software for images taken in “diffraction mode” was inaccurate at the time of the experiments. While this does not affect any of the results presented in this work so far, it means that the dimensions in Figure 61 cannot be used to calculate interplanar spacings as it was done with the FT-images. However, the *ratios* between the rings’ diameters should still hold true and can be used to accurately index the lattice orientations that they represent.

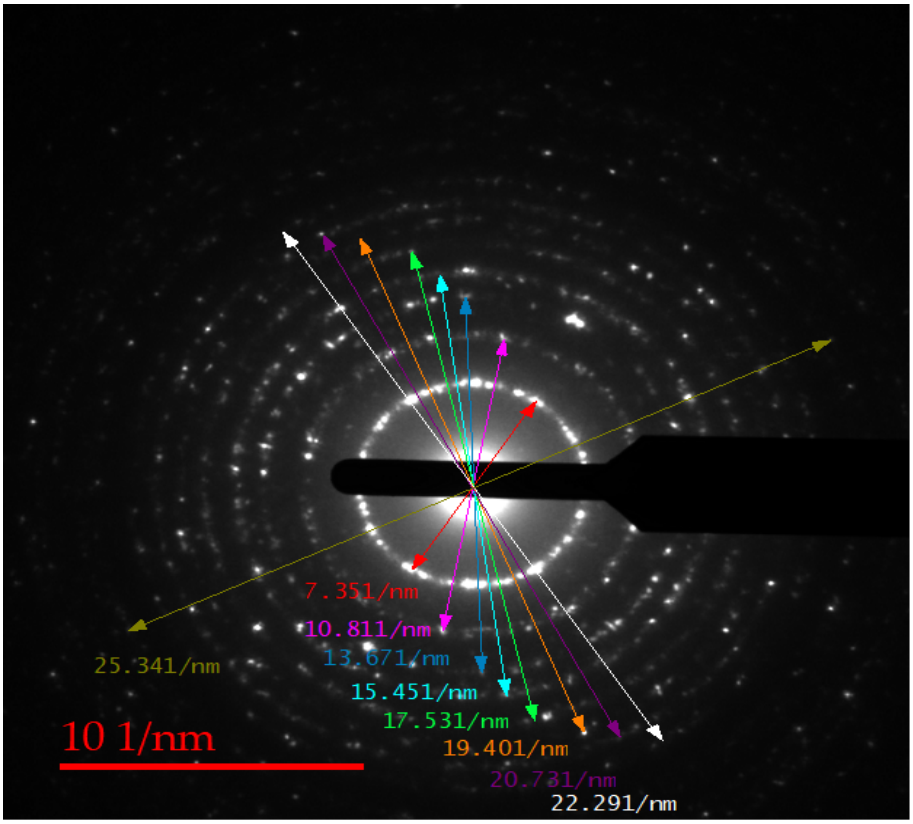

Figure 61 Ring diffraction pattern from the polycrystalline TiO_2 specimen, with ring diameters as measured

Table 13 correlates the diffractions found in Figure 61 to the main diffraction peaks found in XRD spectra of anatase. An illustrative XRD spectrum is shown in Figure 86 of Appendix D. Since the XRD spectrum shows the strongest diffractions for a given material, it is expected that the same crystallographic orientations will be present in the ring diffraction pattern. As it can be seen in the spectrum, some of the diffraction peaks are doublets or triplets due to the similarity of d-spacings between different lattice orientations. In practice, that means that some of the rings visible in Figure 61 are actually composed of multiple overlapping rings diffracted off different sets of planes. That is the case, for instance, of the second ring from the center, which is composed by the electron beam intensity diffracted off the (103), (004) and (112) families of atomic planes. In fact, one can verify that along this ring there are multiple bright spots at different distances from

the center of the diffraction pattern, indicating that they are caused by diffraction off distinct lattice orientations.

Table 13 Comparison between theoretical ring diameters for lattice orientations found in the XRD spectrum of anatase and those measured experimentally

XRD peaks	Theoretical d-spacing [Å]	Theoretical $D_{ring}\ [1/nm]$	Theoretical D^i/D^1	Experimental $D_{ring}\ [1/nm]$	Experimental D^i/D^1
(101)	3.5294	5.67	1.00	7.35 ± 0.16	1.00
(103)	2.4383	8.20	1.45	10.81 ± 0.16	1.47
(004)	2.3847	8.39	1.48		
(112)	2.3406	8.54	1.51		
(200)	1.8995	10.53	1.86	13.67 ± 0.16	1.86
(105)	1.7049	11.73	2.07	15.45 ± 0.16	2.10
(211)	1.6726	11.96	2.11		
(213)	1.4985	13.35	2.36	17.53 ± 0.16	2.39
(204)	1.4858	13.46	2.38		
(116)	1.3682	14.62	2.58	19.40 ± 0.16	2.64
(220)	1.3431	14.89	2.63		
(215)	1.2688	15.76	2.78	20.73 ± 0.16	2.82
(301)	1.2553	15.93	2.81		
(224)	1.1703	17.09	3.02	22.29 ± 0.16	3.03
(312)	1.1650	17.17	3.03		
Weak diffraction	N/A	N/A	N/A	25.34 ± 0.16	3.45

The data shown in Table 13 reveals a tight correspondence between the theoretical and experimental values. As expected, the experimentally measured ring diameters do not match those calculated from anatase XRD data due to the lack of proper calibration of the scale bar. However, the ratios between ring diameters are a very close match, as demonstrated by the columns highlighted in green. This leads to the conclusion that the first order diffraction (first ring from the center) in Figure 61 is a result of the (101) plane singlet, the second ring is a result of the $[(103), (004), (112)]$ triplet, the third ring a result of the (200) singlet, and so on. One can infer, based on the analysis of the spot and ring diffraction patterns, that the Fe-TiO_2 crystallites have a lattice structure that is indistinguishable from that of pure anatase TiO_2. The addition of iron as a doping agent, at the low concentrations used in this study, did not have an appreciable effect on the microstructure of the material.

3.3.4. EELS

Electron Energy Loss Spectrometry was carried along the edge of the Fe-TiO_2 specimen to collect spectra yielding compositional information. The electron beam was accelerated at 200 kV, producing a magnification of 160,000 times for the spectrum collection. The spectrometer used for this analysis possessed the following configuration: a convergence semi-angle of 18.0 mrad, a collection semi-angle of 45.0 mrad, and an entrance aperture of 2.5 mm. The EELS data collection was done in the microscope's STEM mode, which is favourable for creating *spectrum*

images where a full spectrum is stored in each pixel [106]. Figure 62a shows an spectrum image where the pixel size is $20nm \times 20nm$, while Figure 62b shows the analog image corresponding to the sampled edge surroundings. The acquisition of a spectrum image enables the analysis of individual spectra stored in each pixel, or the sum of spectra over a larger area. In Figure 62a, the 7x7 area enveloped by the red square labeled “1” was used to generate the Sum Spectrum shown in Figure 63. The remaining pixels were excluded from the Sum Spectrum due to the low signal-to-noise ratio, likely due to the excessive thickness of the wedge specimen in that region.

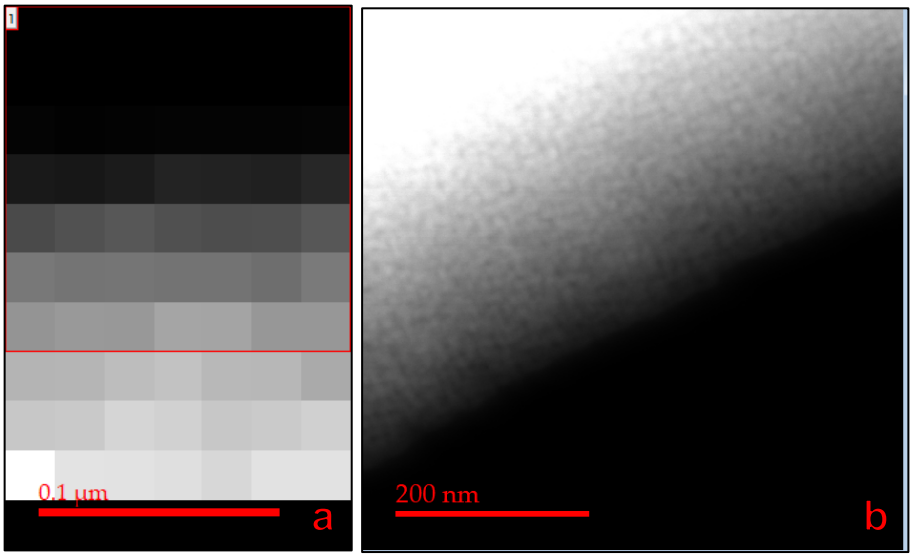

Figure 62 Spectrum image of the edge of the Fe-TiO2 specimen (a) and analog image of the edge region where the spectra were acquired (b)

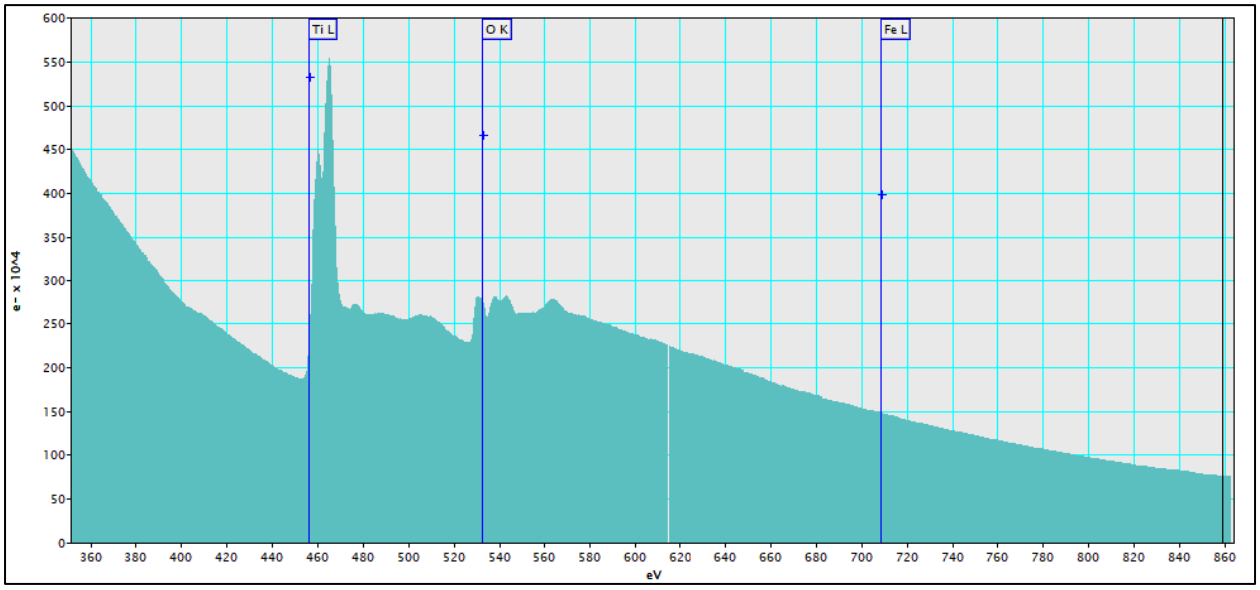

Figure 63 EELS spectrum of an area at the edge of the Fe-TiO2 specimen, with the partial ionization edges for O, Ti and Fe indicated

Figure 63 clearly shows some of the characteristic features of the high-loss region of EELS spectra, between 350 and 860 eV. One can observe the partial ionization edges for Ti (L transition

at 456 eV), O (K transition at 532 eV) and Fe (L transition at 708 eV) against an exponentially decreasing plural scattering background. The L edges actually contain multiple transitions (corresponding to the ionization energies for different orbitals), which will be highlighted in a subsequent step. The ionization edges shown here can be used to infer element-specific information such as relative abundances, however it is clear that they differ from an ideal, saw-toothed hydrogenic edge as shown in Figure 11a. The fine structure seen after the main peak of the edges (ELNES, or *Energy-Loss Near-Edge Structure*) is caused by the plural scattering of the electrons participating in the partial ionization of the respective edge atoms. This results in an increased total energy loss, usually due to bonding effects and plasmonic interactions, which translate into smaller, higher-energy peaks extending up to 50 eV past the edge onset. The intensity of the edges, at a first glance, indicates a much lower abundance of iron compared to oxygen and titanium. However, the edge intensities must be corrected by an ionization cross-section coefficient before compositional ratios can be quantified.

Calculating the relative element ratios from EELS spectra is traditionally done using the relationship described by Equation 57, where N is the number of atoms per unit area of the specimen contributing to the edge intensity, $I_K(\beta\Delta)$ is the K-edge intensity under a collection angle β and integrated over an energy range Δ after the the edge's critical ionization energy ε, and $\sigma_K(\beta\Delta)$ is the partial ionization cross-section for the same β and Δ values. The equation is written in terms of intensity and ionization cross-section for the K-edge, but the same basic approach can be used for other edges [106].

$$\frac{N_A}{N_B} = \frac{I_K^A(\beta\Delta) \times \sigma_K^B(\beta\Delta)}{I_K^B(\beta\Delta) \times \sigma_K^A(\beta\Delta)} \qquad \text{Equation 57}$$

Accurately quantifying elements using EELS presents several challenges. Equation 57 carries with it the assumption that the electrons in the spectrum undergo a single scattering event when traversing the specimen, which is a strong hypothesis that can introduce up to 10-20% error into the final composition results. Given the small concentrations of iron in the Fe-TiO_2 specimen used for this study, this error margin is clearly unacceptable. Removing the effects of plural scattering can be done through a process of *deconvolution*, which extracts the single-scattering contributions from the total intensity in the spectrum. Another challenge involves subtracting the background accurately to obtain the edge intensity I_K (or I_L, I_M, etc) for each element. While this can be straightforward using a power-law model, the varying thickness of our wedge-shaped specimen makes this approach unreliable. In this case, a more complex analysis is required to remove the background, such as a first-difference approach. Lastly, the determination of the partial ionization cross-section σ_K (or σ_L, σ_M, etc) using the usual, simple hydrogenic model becomes less reliable as the atomic number of the elements involved increases, requiring a more complex model and finer control of experimental conditions for heavier elements [106]. All of these challenges, combined with the fact that EDX is a simpler, yet sufficiently accurate, quantification technique for heavy elements, has led the EELS analysis in this study to remain *qualitative*.

Figure 64 through Figure 67 show in detail the ionization edges for the Ti, O and Fe electronic transitions. Moreover, the stretch of the spectrum before the onset of the ionization edges was used to model the background scattering using a Power Law, and then extrapolated to beyond the edges in order to obtain the assumed single-scattering intensity for the electronic transitions. Figure 64 shows this process for the Ti edges (L1, L2 and L3 transitions), and Figure 65 shows it

for the single O edge (K transition). The presence of Ti and O in the specimen is clearly verified by the presence of a strong initial edge onset (a high *jump ratio*) at every possible edge transition within this energy range, followed by the characteristic fine structure caused by plasmonic transitions.

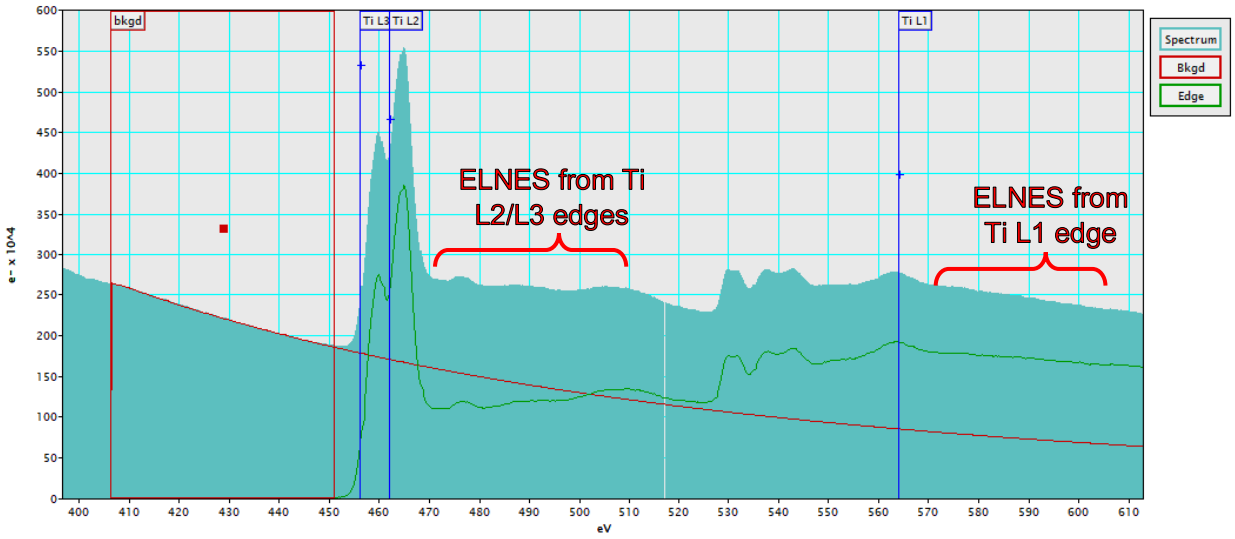

Figure 64 Detail on the EELS spectrum showing the edges caused by Ti electronic transitions (L1, L2 and L3), and the process of extracting the single-scattering intensity through background subtraction

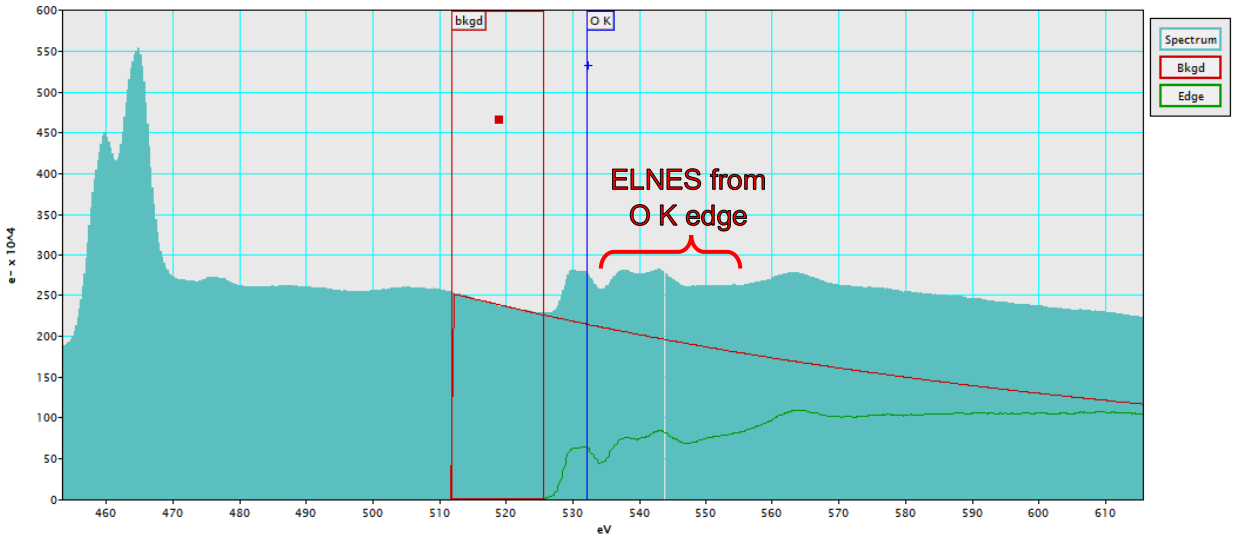

Figure 65 Detail on the EELS spectrum showing the edge caused by the O electronic transition (K), and the process of extracting the single-scattering intensity through background subtraction

Whereas the Ti and O edges are quite evident in the EELS analysis of the Fe-TiO_2 specimen, the Fe signal is not as obvious. Figure 66 and Figure 67 both show the partial ionization edges caused by the Fe electronic transitions, but the former shows the background subtraction from the L2 and L3 transitions, while the latter shows it for L1. As it can be seen indicated by the annotations in the Figures, the Fe signal is extremely weak above the background intensity, close to the noise level for this spectrum. The presence of trace iron in the sample is not in question due to the

observations made in this study so far: sufficient Fe precursor was added to the sol-gel synthesis process, the Fe-TiO_2 particles showed increased photocatalytic activity compared to non-doped TiO_2 particles, and the EDX analyses detected Fe in the specimen. Moreover, the individual spectra stored in each pixel (as opposed to the *Sum Spectra* over a large area, shown in this section) did not exhibit more prominent Fe edges compared to the Sum spectrum. This indicates that there is no iron accumulation at any given position relative to the others, as that would be verified by an increase in the iron edge intensity.

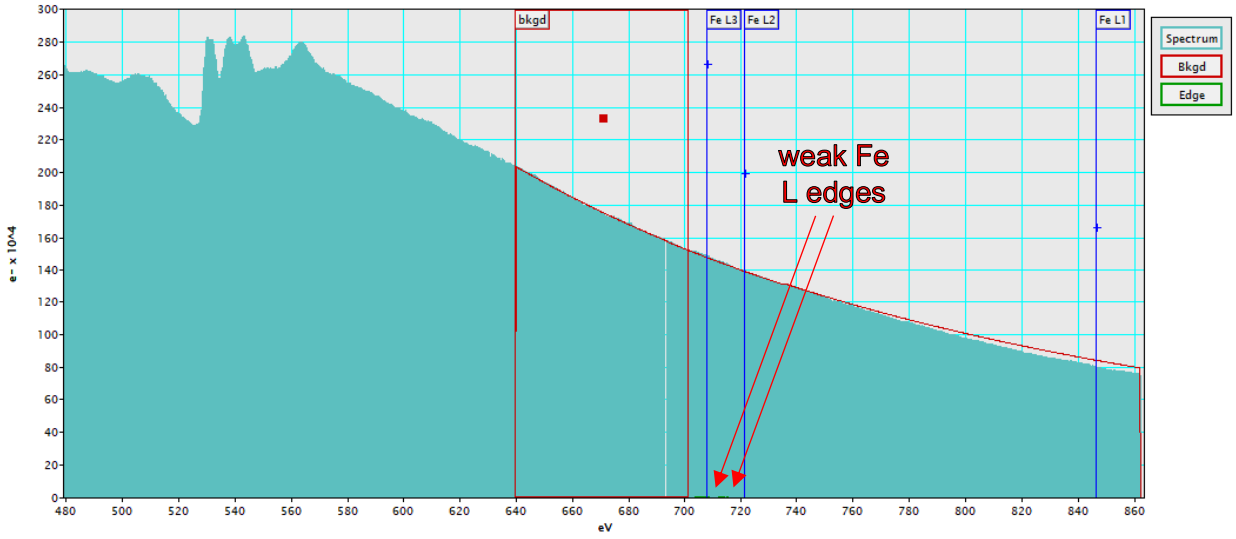

Figure 66 Background scattering subtraction for the L2 and L3 transition edges of Fe, in the EELS spectrum of the Fe-TiO_2 specimen

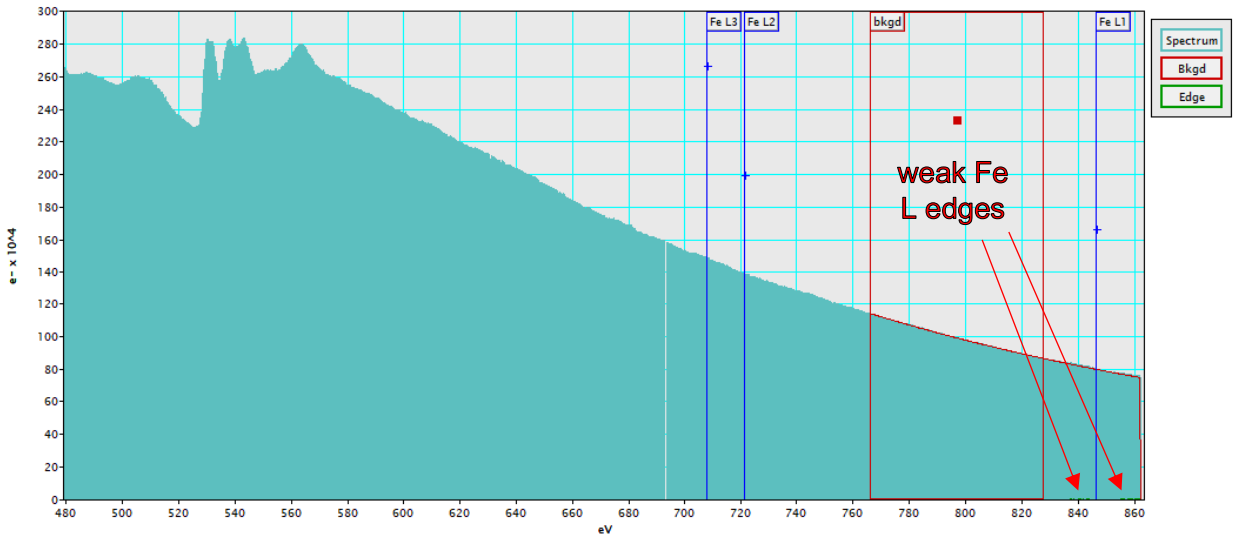

Figure 67 Background scattering subtraction for the L1 transition edge of Fe, in the EELS spectrum of the Fe-TiO_2 specimen

The EELS analysis of the specimen qualitatively supports the conclusions reached during previous analyses such as EDX and diffraction patterns: that the iron content in the photocatalyst is homogeneously distributed across the crystalline and amorphous phases, without significantly altering the original lattice structure of anatase TiO_2.

3.4. Conclusion

The following insights can be drawn from the experimental results of this study:

- The Fe-TiO_2 photocatalyst particles are amenable to all steps of the specimen preparation protocol, namely lift-off, welding, milling and polishing. The particles maintained structural integrity even during transfer between substrates using a microprobe, or during milling using a Ga focused ion beam.
- The FIB milling step during sample preparation produced an undesirable damage layer on the surface of the wedge specimen, theoretically composed of implanted Ga ions from the FIB, back-sputtered W and Cu, and native material (anatase Fe-TiO_2) turned amorphous due to the impact of heavy Ga ions. Further inspection using EDX showed that the surface damage layer was mostly amorphous native material, as Ga, W and Cu were only present in trace amounts.
- Polishing the wedge specimen with a mild BIB system is an effective way to clear the amorphous damage layer created during the milling step. The change in surface texture also indicated that the polishing system etches the specimen in preferential directions. This anisotropy is theorized to result from the presence of amorphous Fe-TiO_2 between monocrystalline crystallites.
- The sample preparation protocol yielded a wedge-shaped specimen whose edge is a single Fe-TiO_2 crystallyte thick (10-20 nm), therefore adequate for transmission microscopy. Secondary-electron and bright-field images revealed the morphology of individual crystallites (as small as 10nm, irregular in shape but approximately round) and confirmed that the material between crystallites was milled preferentially by the FIB.
- EDX analyses of the specimen found only elements that were present in the original particles, in the specimen holder, in the microscope's electronics or involved in the fabrication protocol.
- Comparative point and line-scan analyses found the atomic concentration of Fe in the specimen to fluctuate between 0.173% and 0.348% but without significant differences between crystallites and the material between them. This indicates that the Fe precursor added during synthesis probably did not segregate to the inter-crystallite space as iron oxide.
- The Fe quantification from EDX might not be accurate due to its low concentration, close to the equipment's detection limit (0.1% - 0.5%). However, one can be sure that the Fe concentration in the regions surveyed does not exceed 0.5%. As well, the EDX line-scans demonstrated that the Fe/Ti signal ratio in the sample remains constant across several crystallites, supporting the conclusion that its concentration is relatively homogeneous inside Fe-TiO_2 particles.
- High-magnification transmission images elucidated the microstructure of the Fe-TiO_2 crystallites at increasing level of details with increasing magnification. The outline and periodic structures (atomic planes) of the crystallites could be observed, as well as the seemingly amorphous material between crystallites and common transmission imaging artifacts (Fresnel fringes, Moiré fringes).
- The amorphous material in-between crystallites appears on transmission images as "fuzzy", poorly defined features without any visible long-range periodicity. These amorphous regions may have been a consequence of the fabrication process where the

pre-existing lattice was damaged, or they may be residual amorphous TiO_2 that did not fully crystallyze during the calcination step of the synthesis process.

- The incomplete merging of two crystallites was verified in one of the transmission images due the continuity of some of the atomic planes between crystallites. It has been reported that the crystallites may undergo dislocation-mediated rigid-body rotation in order to realign themselves and merge.
- An objective aperture was used to select the electron beam intensity diffracted off certain atomic planes and highlight the crystallites from where the selected intensity is being diffracted. This technique allowed the observation of the morphology of individual crystallytes against a dark background, revealing them as multifaceted particles with clean faces and sharp angles.
- Fourier images were generated by applying a Fourier Transform operator over seemingly monocrystalline regions of the specimen. These digitally-generated images are equivalent to diffraction patterns obtained by centering the electron beam spot on a monocrystal.
- The Fourier images were used to successfully index the crystallographic orientations of monocrystalline anatase titania. The images also provided information on interplanar spacings, zone axes, angles between atomic planes, amorphous material in the sample, and Fresnel fringes in the original transmission image.
- Ring diffraction patterns were obtained by acquiring a diffraction image with an electron beam spot size covering a large, polycrystalline region of the specimen. The ring diameter ratios correspond to those found in anatase TiO_2.
- The crystallographic analyses, both using Fourier Images and Ring Diffraction Patterns, indicate that the lattice structure of the Fe-TiO_2 specimen is indistinguishable from that of pure anatase titania. The addition of an iron precursor in trace amounts as a doping agent, occupying interstitial sites, did not have an appreciable effect on the samples microstructure in terms of lattice strain or interplanar spacings.
- Electron Energy Loss Spectrometry (EELS) was used to qualitatively investigate the segregation of iron near the edge of the specimen. The spectra collected showed prominent Ti and O partial ionization edges, but only a weak Fe signal comparable to noise levels once the background signal was extracted. This indicates that Fe is present in trace amounts, close to the lower detection limits of the technique (0.1% - 0.5%), and distributed homogeneously across the specimen.

The research goals outlined at the beginning of this study were successfully achieved. The microfabrication protocol using a Focused Ion Beam, although labor-intensive, yielded an adequate wedge-shaped specimen whose decreasing thickness (towards the edge) and state-of-surface were ideal for advanced microscopy analyses. The microstructure of the Fe-TiO_2 photocatalyst particles was elucidaded through Secondary Electron and Bright Field imaging. Crystallographic information was extracted from Fourier images, ring diffraction patterns and high-resolution transmission imaging. Finally, compositional profiles of the specimen were obtained by EDX and EELS, addressing the differences between the monocrystalline units (crystallites) and the amorphous material in-between them.

The results from the crystallographic analyses seem to indicate that adding small amounts of iron impurities as a doping agent did not significantly alter the lattice structure of pure titania. It is known that the similar atomic ratio of Ti^{4+} and Fe^{3+} favours the incorporation of iron atom impurities at substitution sites within the anatase TiO_2 lattice, however this substitution could still produce

significant lattice strain. It was verified that, possibly due to the low Fe/Ti atomic ratio (below 0.5%), the original anatase structure remained unchanged in terms of interplanar spacings and angles between crystallographic orientations. As well, the presence of amorphous material in between crystallites was observed, although at this point it is unclear whether it originates from damage to the pre-existing lattice during specimen fabrication, non-crystallized residue from the sol-gel synthesis process, or a combination of both.

The compositional analyses of the specimen showed that the concentration of iron is uniform across the sample, and as low as the detection limits of the techniques employed. These low concentrations were expected from the beginning, since the Fe precursor was added at an atomic ratio of 0.5% during the synthesis step, and a fraction of it is bound to be lost as iron oxide when the contamination layer is acid-washed off the particles' surface. Comparative analyses between different regions of the specimen indicated that there was no iron oxide build-up in the space between crystallites, which would be recognized by an increase in the Fe signal (either characteristic X-rays or energy-loss signal) in those regions. One can conclude, therefore, that the amorphous material filling the spaces between crystallites must be uncrystallized Ti, O and Fe at equivalent atomic concentrations as the rest of the sample. Although these analyses cannot completely rule out the presence of iron oxides within the catalyst particles due to the weak Fe concentrations (comparable to the detection limits), they did not find any evidence that the oxide contamination layer is formed anywhere but on the external surface of the catalyst particles.

The aforementioned results are promising and provide enough information to allow one to speculate about the origins of the external iron oxide contamination layer. As reported in Section 2.2.1, the iron precursor ($Fe(NO_3)_2.9H_2O$) is added to the sol-gel solution at the very beginning of the synthesis process, such that Fe^{3+} ions are present throughout the entire synthesis. As the sol reticulates, forming the $(-Ti-O-Ti-)_n$ network, it seems that a fraction of the iron (III) ions in the solution is incorporated into the gel. This could take place via two mechanisms: substitution of Ti by Fe in the newly formed $(-Ti-O-Ti-)_n$ network, or trapping of solubilized Fe^{3+} ions in isolated "pockets" of this expanding network. The former seems more likely, as the latter could result in localized increases in Fe concentration within the particles and this was not observed during this study. As for the excess iron content that was not incorporated into the gel network, it is reasonable to assume that it precipitates as iron oxides on the external surface of the newly formed Fe-TiO_2 particles during the drying step, thus forming the unconspicuous oxide contamination layer that so hindered the photocatalytic activity of iron-doped titania in the past. As the crystallites nucleate and grow during the calcination step, iron oxide remains on the outer surface of particles. The uniformly distributed Fe content inside the particles does not segregate preferentially to the amorphous interfaces between crystallites. Although more in-depth studies would be required to completely elucidate the mechanism through which iron oxides accumulate on certain regions of the photocatalyst, this initial proposition for a mechanism explains why iron oxide is found exclusively on the outer surface of the photocatalyst particles, but not within or in-between crystallites.

Future work following the conclusion of this study will include an in-depth analysis of the synthesis process to elucidate the formation of the iron oxide contamination layer in more detail. As well, the mobility of charge carriers in amorphous anatase has to be analyzed in order to verify whether e^-/h^+ pairs generated deep within the photocatalyst particles are able to cross crystallite boundaries and reach the surface to participate in oxidation reactions. Efforts will also be directed

towards optimizing the EELS quantitative compositional analysis, which can be highly sensitive given the right operation conditions and a thin specimen of constant thickness.

Chapter 4 Concluding Remarks

This chapter summarizes the work done over the course of this thesis and lists future research that can be carried to build on the results that this work has yielded. It opens with a thesis overview, highlighting the rationale fueling research endeavors and the results obtained (4.1). It then closes with a description of follow-up work which could not be included in this thesis, exhorting future researchers to follow the leads unveiled by the experiments described herein (4.2).

4.1. Thesis overview

The novel iron-doped TiO_2 particles studied in this work, synthesized through a method that exposes the particles' reactive surface by removing an iron oxide contamination layer, represent a significant advancement in the fields of photocatalysis, wastewater treatment, and Advanced Oxidation Processes. Considering its high reaction rates and ability to produce Reactive Oxidation Species using cheap, visible light, it is clear that this novel photocatalyst is a powerful resource to address the current treatment plant limitations and the upcoming global water crisis. However, as with any other novel material, it must be fully characterized and understood before large-scale applications can be developed. Special concern has been voiced about the size distribution of the catalyst particles, since it is known that the monocrystalline sub-units of this material (crystallites) are in the nanometer scale. If the current synthetic method produces a significant fraction of the catalyst as nanoparticles, it could have adverse effects on human and environmental health. As well, the inner structure of the Fe-TiO_2 catalyst is not fully understood. In particular, one wishes to know whether iron oxides could be present inside the particle and, if so, whether it poses an obstacle to the photo-generated charge carriers percolating to the surface of the catalyst. These questions form the rationale guiding the electron microscopy studies presented in this work.

Results from the particle size distribution analysis using a scanning electron microscope (SEM) showed that the novel synthetic method (including an acid-wash step to remove surface iron oxides) does indeed produce a significant fraction (31.55%) of the catalyst particles with dimensions below 100 nm. However, these nanoparticles represent a negligible fraction of the total catalyst mass (0.00015%) and also a very small percentage of the total catalyst area available for oxidation reactions (0.03%). This indicates that, were this fraction of the particles to be removed through an additional separation step, the photocatalyst powder would be considered safe for use without significant losses of total sample mass or reactive surface. On the other hand, the size distribution analysis revealed that bigger particles concentrate most of the sample's mass and chemical activity. This represents another area of improvement in the synthesis protocol, as breaking down big particles to safe, intermediate sizes (between 500 nm and a few μm) could potentially increase photocatalytic activity due to the increase in the surface-to-volume ratio of the catalyst.

The transmission electron microscopy (TEM) study revealed the inner morphology and composition of the Fe-TiO_2 photocatalyst particles. The catalyst particles are composed of nanosized monocrystals (crystallites) joined together by amorphous material. These crystallites are supposedly formed during the calcination synthesis step, when they nucleate in amorphous Fe-TiO_2 and grow until they reach the neighbouring crystallites. The lattice strain keeps the material at the interfaces amorphous. The composition of the catalyst particles seems to be

homogenous over crystalline and amorphous regions, indicating that the doping agent does not segregate preferentially to either region inside the particle. The excess iron content forming the iron oxide contamination layer on the surface of particles is theorized to not have been integrated into the $(-Ti-O-Ti-)_n$ gel network during the sol-gel synthesis, resulting in precipitation as iron oxide upon drying of the gel. This mechanism explains why iron oxide is not found inside the catalyst particles. Diffraction analyses also showed that the crystallographic structure of iron-doped anatase titania is indistinguishable from pure anatase TiO_2, indicating that introducing Fe^{3+} impurities at Ti^{4+} substitution sites at trace concentrations did not create significant lattice strain in the crystalline structure.

This thesis provided answers to several of the questions surrounding the novel Fe-TiO_2 catalyst particles, especially regarding its macro- and microstructures. A complete understanding of the phenomena taking place on both scales is required in order to model the desired reactions and design applications for this photocatalyst. The results contained herein, relevant as they are, are no more than pieces of a bigger puzzle: several other mechanisms play a role in determining the final efficiency of the catalyst, such as mass/energy transfers, quantum yield of the semiconductor, porosity of the particles, design of the oxidation reactor, geometry and nature of the substrate, etc. The next section of this chapter (4.2), wrapping up this work, outlines some of the future research avenues arising from the results of this thesis. These electron microscopy analyses were essential to understand some of the fundamental characteristics of this promising novel material, as well as to guide subsequent research. The novel Fe-TiO2 photocatalyst might yet prove to be a powerful tool to face the increasing challenges involved in supplying clean water to those in need.

4.2. Future work

Although efforts were made to make this work as comprehensive as possible, experiments often uncover more questions and there is always further research that can be done. As the scope of this thesis was limited to simply exploring the novel photocatalyst particles under different electron microscopes, we will indicate some future research avenues that either arose from the results contained herein, or that could not be followed at the time of writing due to time and equipment limitations.

The synthesis protocol currently used to produce Fe-TiO_2 particles has been the object of discussion in the experimental chapters of this thesis. It has been argued that fully understanding and improving the synthesis steps could result in relevant gains in terms of photocatalytic efficiency. It is recommended that future researchers optimize the particle size distribution of the final product by reducing the abundance of particles bigger than a couple μm and by designing an additional separation step to remove particles smaller than 100 nm. The former could be achieved by increasing the duration and power of the grinding steps, for instance, in order to shift the size distribution to intermediate particle sizes. The latter can be addressed by any separation unit adequate for this size range, such as a cyclone separator as it has been explained in Section 2.4.

Another avenue for future work could be the fine-tuning of the experiments done in this thesis, which would in turn improve the quality and accuracy of results. As previously said, the scope of these studies was to provide a first look into the macro- and microstructure of the novel

photocatalyst using the techniques and equipment available at hand. It follows that these results can be improved and expanded by building on the experience acquired over this first batch of experiments. Several refinements can be applied to the particle size distribution analysis in order to improve the quality of results, such as sonicating the catalyst sample to separate small particles from bigger ones, optimizing the thickness of the carbon coating conductive layer to avoid smoothing out nanoparticles, and employing a higher acceleration voltage to detect titania particles that might be covered by the amorphous carbon coating. As well, the transmission microscopy results could be improved by fabricating a thin specimen of constant thickness this time around, opposed to the wedge-shaped specimen used in this study. Milling a sample of constant thickness presents further challenges but could significantly improve diffraction results and the resolution of quantitative EELS analysis.

Finally, several avenues could be explored in order to understand the mechanisms behind the iron oxide contamination layer formation and the photocatalytic reactions. The iron oxide layer is ostensibly formed during synthesis due to the residual iron ions in solution after the gel has formed. It is advised that the sol-gel process used to precipitate Fe-TiO_2 be studied closer, with samples of the solution after each wash (either with water or acid) run through a sensitive analytical instrument (such as a HPLC, High Performance Liquid Chromatograph) to draw information about the evolving composition of the system. As well, tracking variables such as the pH and reduction potential of the solution might be helpful in pinpointing the step in which iron oxide tends to form. Pourbaix diagrams, which contain phase information plotted against solution pH and reduction potential, are widely available. Lastly, the reaction rate constants for the oxidation reactions have to be accurately measured in a finely controlled system. It is recommended that some sort of microstructured reactor be used for this study, as the increased surface-to-volume ratio of small reaction spaces removes mass and heat transfer limitations, allowing the precise measurement of reaction rates under very controlled conditions. This, added to theoretical research of the charge carriers' mobility in amorphous anatase TiO_2, should provide a better understanding of the photocatalytic efficiency of this novel semiconductor, also referred to as the quantum yield.

With a complete picture of the mechanisms ruling the photoactivation of iron-doped anatase titania, one is able to conceive and design engineering applications for this novel material. The photocatalyst is extremely versatile due to its assumed biocompatibility (at proper particle sizes), non-selectivity and affinity with a number of substrates. The Fe-TiO_2 particles can be implemented in slurry reactors, immobilized onto substrates, as part of a fluidized bed reactors to clean gas streams, etc.. Recently, this research group has observed that the photocatalyst also shows enhanced activation when exposed to an external electric potential (unpublished). The possibilities are endless, and will increase the competitivity of photocatalysis among current cleaning technologies focused on eliminating persistent, harmful organic molecules.

References

[1] "Water and Sanitation - United Nations Sustainable Development," United Nations, [Online]. Available: https://www.un.org/sustainabledevelopment/water-and-sanitation/.

[2] "Water, sanitation and hygiene (WASH)," World Health Organization, [Online]. Available: https://www.who.int/health-topics/water-sanitation-and-hygiene-wash.

[3] D. Mantzavinos, R. Hellenbrand, A. G. Livingston and I. S. Metcalfe, "Reaction mechanisms and kinetics of chemical pretreatment of bioresistant organic molecules by wet air oxidation," *Water Science & Technology,* vol. 35, no. 4, pp. 119-127, 1997.

[4] M. Hassanshahian, M. Abarian and S. Cappello, "Biodegradation of Aromatic Compounds," in *Bioderadation and Bioremediation of Polluted Systems*, R. Chamy and F. Rosenkranz, Eds., IntechOpen, 2015.

[5] Ö. Kerkez-Kuyumcu, E. Kibar, D. Kübra, F. Gedik, A. N. Akin and S. Özkara-Aydinoglu, "A comparative study for removal of different dyes over M/TiO2 (M = Cu, Ni, Co, Fe, Mn, Cr) photocatalysts under visible light irradiation," *Journal of Photochemistry and Photobiology A: Chemistry,* vol. 311, pp. 176-185, 2015.

[6] P. R. Gogate and A. B. Pandit, "A review of imperative technologies for wastewater treatment I: oxidation technologies at ambient conditions," *Advances in Environmental Research,* vol. 8, pp. 501-551, 2004.

[7] L. Theodore, P. S. Farber, K. N. Weiss, M. K. Heerman, R. D'Aquino, J. D. McKenna, R. R. Sharp and S. A. Thorneloe, "Section 22: Waste Management," in *Perry's Chemical Engineers' Handbook*, McGraw-Hill Education, 2019.

[8] T. Oppenländer, Photochemical Purification of Water and Air, Wiley, 2007.

[9] M. Cheng, G. Zeng, D. Huang, C. Lai, P. Xu, C. Zhang and Y. Liu, "Hydroxyl radicals based advanced oxidation processes (AOPs) for remediation of soils contaminated with organic compounds: a review," *Chemical Engineering Journal,* vol. 284, pp. 582-598, 2016.

[10] T. Ali, P. Tripathi, A. Azam, W. Raza, A. S. Ahmed, A. Ahmed and M. Muneer, "Photocatalytic performance of Fe-doped TiO2 nanoparticles under visible-light irradiation," *Materials Research Express,* vol. 4, p. 015022, 2017.

[11] V. Augugliaro, V. Loddo, M. Pagliaro, G. Palmisano and L. Palmisano, Clean by Light Irradiation: Practical Applications of Supported TiO2, Cambridge: Royal Society of Chemistry, 2010.

[12] R. L. Pozzo, J. L. Giombi, M. A. Baltanás and A. E. Cassano, "Performance in a fluidized bed reactor of photocatalysts immobilized onto inert supports," *Catalysis Today,* vol. 62, no. 2, pp. 175-187, 2000.

[13] M. Shokri, G. Isapour, M. A. Behnajady and S. Dorosti, "A comparative study of photocatalytic degradation of the antibiotic cefazolin by suspended and immobilized TiO2," *Desalinization and Water Treatment,* vol. 57, no. 27, pp. 12874-12881, 2016.

[14] J. Schneider, M. Matsuoka, M. Takeuchi, J. Zhang, Y. Horiuchi, M. Anpo and D. W. Bahnemann, "Understanding TiO2 Photocatalysis: Mechanisms and Materials," *Chemical Reviews,* vol. 114, no. 19, pp. 9979-9986, 2014.

[15] B. Ramos, *Intensification of photo-induced oxidation processes by using micro-structured reaction spaces,* Tokyo Institute of Technology, 2014.

[16] M. Sidheswaran and L. L. Tavlarides, "Characterization and Visible Light Photocatalytic Activity of Cerium- and Iron-Doped Titanium Dioxide Sol-Gel Materials," *Industrial & Engineering Chemical Research,* vol. 48, no. 23, pp. 10292-10306, 2008.

[17] R. d. S. Santos, G. A. Faria, C. Giles, C. A. P. Leite, H. d. S. Barbosa and M. A. Z. Arruda, "Iron Insertion and Hematite Segregation on Fe-Doped TiO2 Nanoparticles Obtained from Sol-Gel and Hydrothermal Methods," *Applied Materials & Interfaces,* vol. 4, no. 10, pp. 5555-5561, 2012.

[18] S. Zhu, T. Shi, W. Liu, S. Wei, Y. Xie, C. Fan and Y. Li, "Direct determination of local structure around Fe in anatase TiO2," *Physica B: Condensed Matter,* vol. 396, no. 1-2, pp. 177-180, 2007.

[19] W. Choi, A. Termin and M. R. Hoffmann, "The Role of Metal Ion Dopants in Quantum-Sized TiO2: Correlation between Photoreactivity and Charge Carrier Recombination Dynamics," *Journal of Physical Chemistry,* vol. 98, no. 51, pp. 13669-13679, 1994.

[20] V. Moradi, M. B. G. Jun, A. Blackburn and R. A. Herring, "Significant improvement in visible light photocatalytic activity of Fe doped TiO2 using an acid treatment process," *Applied Surface Science,* vol. 427, no. B, pp. 791-799, 2018.

[21] N. Negishi, S. Matsuzawa, K. Takeuchi and P. Pichat, "Transparent Micrometer-Thick TiO2 Films on SiO2-Coated Glass Prepared by Repeated Dip-Coating/Calcination: Characteristics and Photocatalytic Activities for Removing Acetaldehyde or Toluene in Air," *Chemistry of Materials,* vol. 19, no. 15, pp. 3808-3814, 2007.

[22] P. R. Gogate, S. Mujumdar and A. B. Pandit, "A Sonophotochemical Reactor for the Removal of Formic Acid from Wastewater," *Industrial & Engineering Chemistry Research,* vol. 41, no. 14, pp. 3370-3378, 2002.

[23] W. H. Glaze, F. Beltran, T. Tuhkanen and J. W. Kang, "Chemical models of advanced oxidation processes," *Water pollution research journal of Canada,* vol. 27, no. 1, pp. 23-42, 1992.

[24] O. Legrini, E. Oliveros and A. M. Braun, "Photochemical processes for water treatment," *Chemical Reviews,* vol. 93, no. 2, pp. 671-698, 1993.

[25] M. R. Hoffman, S. T. Martin, W. Choi and D. W. Bahnemann, "Environmental Applications of Semiconductor Photocatalysis," *Chemical Reviews,* vol. 95, no. 1, pp. 69-96, 1995.

[26] J. Hoffmann, H. Tauchnits and H. Vanselow, "Catalytic oxidation - a new method for the degradation of pollutants in wastewater," *Chemical Engineering & Technology,* vol. 23, pp. 125-127, 2000.

[27] N. N. Mahamuni and Y. Adewuyi, "Advanced oxidation processes (AOPs) involving ultrasound for waste water treatment: A review with emphasis on cost estimation," *Ultrasonics Sonochemistry,* vol. 17, no. 6, pp. 990-1003, 2010.

[28] G. Chen, "Electrochemical technologies in wastewater treatment," *Separation and Purification Technology,* vol. 15, no. 1, pp. 11-41, 2004.

[29] C. Ferradini and J.-P. Jay-Gerin, "La radiolyse de l'eau et des solutions aqueuses: historique et actualité," *Canadian Journal of Chemistry,* vol. 77, no. 9, 1999.

[30] A. G. Chmielewski, Y. Sun, A. Pawelec, J. Licki, A. Dobrowolski, Z. Zimek and S. Witman, "Treatment of off-gases containing NOx by electron beam," *Catalysis Today,* vol. 191, no. 1, pp. 159-164, 2012.

[31] M. A. Rauf and S. S. Ashraf, "Radiation-induced degradation of dyes -- an overview," *Journal of Hazardous Materials,* vol. 166, no. 1, pp. 6-19, 2009.

[32] P. A. Marrone, "Supercritical water oxidation - Current status of full-scale commercial activity for waste destruction," *The Journal of Supercritical Fluids,* vol. 79, pp. 283-288, 2013.

[33] K. K. Rohatgi-Mukherjee, Fundamentals of Photochemistry, Kolkata: New Age International, 1986.

[34] G. R. Peyton, "Oxidative treatment methods for removal of organic compounds from drinking water supplies," in *Significance and treatment of VOCs in water supplies*, Chelsea, Lewis Publishers, Inc, 1996.

[35] H. J. H. Fenton, "Oxidation of certain organic acids in the presence of ferrous salts," *Proceedings of the Chemical Society,* vol. 15, p. 224, 1899.

[36] T. A. Kurniawan, W.-H. Lo and G. Y. S. Chan, "Radicals-catalyzed oxidation reactions for degradation of recalcitrant compounds from landfill leachate," *Chemical Engineering Journal,* vol. 125, no. 1, pp. 35-57, 2006.

[37] R. S. Mulliken, "Spectroscopy, molecular orbitals and chemical bonding," *Science,* vol. 157, pp. 13-24, 1967.

[38] C. J. Cramer, Essentials of Computational Chemistry: Theory and Models, Chinchester: Wiley, 2004.

[39] M. A. Rauf, M. A. Meetani and S. Hisaindee, "An overview on the photocatalytic degradation of azo dyes in the presence of TiO2 doped with selective transition metals," *Desalination,* vol. 276, no. 1, pp. 13-27, 2011.

[40] P. Wardman, "Reduction potentials of one-electron couples involving free radicals in aqueous solutions," *The Journal of Physical Chemistry: Reference Data,* vol. 18, pp. 1637-1755, 1989.

[41] F. A. Cotton and G. Wilkinson, Inorganic Chemistry, Weinheim: Verlag-Chemie, 1974.

[42] J. March and M. B. Smith, March's Advanced Organic Chemistry, New York: John Wiley & Sons, Inc, 2007.

[43] J. Hoigné, "Chemistry of aqueous ozone and transformation of pollutants by ozonation and Advanced Oxidation Processes," in *The handbook of Environmental Chemistry*, vol. 5, O. Hutzinger, Ed., Berlin, Springer-Verlag, 1998, pp. 83-141.

[44] C. V. Sonntag and H. P. Schuchmann, "Peroxyl radicals in aqueous solutions," in *Peroxyl radicals*, Z. Alfassi, Ed., New York, John Wiley & Sons, Inc, 1997.

[45] "Titanium Statistics and Information | U.S. Geological Survey," U.S. Department of the Interior, [Online]. Available: https://www.usgs.gov/centers/national-minerals-information-center/titanium-statistics-and-information. [Accessed 1 November 2021].

[46] H. A. MacLeod, Thin film optical filters, New York: MacMillan, 1986.

[47] N. O. Savage, S. A. Akbar and P. K. Dutta, "Titanium dioxide-based high temperature carbon monoxide selective sensor," *Sensors and Actuators B: Chemical,* vol. 72, pp. 239-248, 2001.

[48] J. A. Disegi and H. Wyss, "Implant materials for fracture fixation: a clinical perspective," *Orthopedics,* vol. 12, pp. 75-79, 1989.

[49] M. Landmann, E. Rauls and W. G. Schmidt, "The electronic structure and optical response of rutile, anatase and brookite TiO2," *Journal of Physics: Condensed Matter,* vol. 24, pp. 1-6, 2012.

[50] O. Carp, C. L. Huisman and A. Reller, "Photoinduced reactivity of titanium dioxide," *Progress in Solid State Chemistry,* vol. 32, pp. 33-177, 2004.

[51] T. L. Villarreal, R. Gómez, M. González and P. Salvador, "A kinetic model for distinguishing between direct and indirect interfacial hole transfer in the heterogenous photooxidation of dissolved organics on TiO2 nanoparticle suspensions," *The Journal of Physical Chemistry B,* vol. 108, pp. 20278-20290, 2004.

[52] V. Moradi, *Synthesis of Iron Doped Titania and its Applications in Degradation of Organic Pollution in Water,* University of Victoria, 2017.

[53] A. Sclafani and J. M. Herrmann, "Comparison of the photoelectronic and photocatalytic activities of various anatase and rutile forms of titania in pure liquid organic phases and in aqueous solutions," *The Journal of Physical Chemistry,* vol. 100, pp. 13655-13661, 1996.

[54] D. Reyes-Coronado, G. Rodríguez-Gattorno, M. E. Espinosa-Pesqueira, C. Cab, R. de Coss and G. Oskam, "Phase-pure TiO2 nanoparticles: anatase, brookite and rutile," *Nanotechnology,* vol. 19, p. 145605, 2008.

[55] U. I. Gaya and A. H. Abdullah, "Heterogeneous photocatalytic degradation of organic contaminants over titanium dioxide: A review of fundamentals, progress and problems," *Journal of Photochemistry and Photobiology C: Photochemistry Reviews,* vol. 9, pp. 1-12, 2008.

[56] K. V. Kumar, K. Porkodi and F. Rocha, "Langmuir-Hinshelwood kinetics - A theoretical study," *Catalysis Communications,* vol. 9, no. 1, pp. 82-84, 2008.

[57] J. R. H. Ross, "The Kinetics and Mechanisms of Catalytic Reactions," in *Contemporary Catalysis: Fundamentals and Current Applications*, Limerick, Elsevier, 2019, pp. 161-186.

[58] R. Molinari, P. Argurio, M. Bellardita and L. Palmisano, "Photocatalytic Processes in Membrane Reactors," in *Comprehensive Membrane Science and Engineering*, vol. 3, Elsevier, 2017, pp. 101-138.

[59] X.-N. Wei, H.-L. Wang, X.-K. Wang and W.-F. Jiang, "Facile synthesis of tunable carbon modified mesoporous TiO2 for visible light photocatalytic application," *Applied Surface Science,* vol. 412, pp. 357-365, 2017.

[60] M. Sun, G. Chen, Y. Zhang, Q. Wei, Z. Ma and B. Du, "Efficient Degradation of Azo Dyes over Sb2S3/TiO2 Heterojunction under Visible Light Irradiation," *Industrial & Engineering Chemistry Research,* vol. 51, no. 7, pp. 2897-2903, 2012.

[61] I.-C. Kang, Q. Zhang, S. Yin, T. Sato and F. Saito, "Improvement in Photocatalytic Activity of TiO2 under Visible Irradiation through Addition of N-TiO2," *Environmental Science & Technology,* vol. 42, no. 10, pp. 3622-3626, 2008.

[62] T. Kemp and R. McIntyre, "Transition metal-doped titanium(IV) dioxide: Characterisation and influence on photodegradation of poly(vynil chloride)," *Polymer Degradation and Stability,* vol. 91, no. 1, pp. 165-194, 2006.

[63] M. Asilturk and F. Sayilkan, "Effect of Fe3+ Ion Doping to TiO2 on the Photocatalytic Degradation of Malachite Green Dye under UV and Vis-Irradiation," *Journal of Photochemistry and Photobiology A: Chemistry,* vol. 203, no. 1, pp. 64-71, 2009.

[64] C. Quiñones, J. Ayala and W. Vallejo, "Methylene blue photoelectrodegradation under UV irradiation on Au/Pd-modified TiO2 films," *Applied Surface Science,* vol. 257, no. 2, pp. 367-371, 2010.

[65] T. Sreethawong, S. Laehsalee and S. Chavadej, "Use of Pt/N-doped mesoporous-assembled nanocrystalline TiO2 for photocatalytic H2 production under visible light irradiation," *Catalysis Communications,* vol. 10, no. 5, pp. 538-543, 2009.

[66] L. G. Devi, N. Kottam, B. N. Murthy and S. G. Kumar, "Enhanced photocatalytic activity of transition metal ions Mn2+, Ni2+ and Zn2+ doped polycristalline titania for the degradation of Aniline Blue under UV/solar light," *Molecular Catalysis,* vol. 382, no. 1-2, pp. 44-52, 2010.

[67] A. M. Shough, D. J. Doren and B. A. Ogunnaike, "Transition metal substitution in ETS10: DFT calculations and a simple model for electronic structure prediction," *Chemistry of Materials,* vol. 21, no. 7, pp. 1232-1241, 2009.

[68] M. Zhou, J. Yu and B. Cheng, "Effects of Fe-doping on the photocatalytic activity of mesoporous TiO2 powders prepared by an ultrasonic method," *Journal of Hazardous Materials,* vol. 137, no. 3, pp. 1838-1847, 2006.

[69] F. Grande and P. Tucci, "Titanium dioxide nanoparticles: a risk for human health?," *Mini Reviews in Medicinal Chemistry,* vol. 16, no. 9, pp. 762-769, 2016.

[70] F. López-Huerta, B. Cervantes, O. González, J. Hernández-Torres, L. García-González, R. Vega, A. L. Herrera-May and E. Soto, "Biocompatibility and surface properties of TiO2 thin films deposited by DC magnetron sputtering," *Materials,* vol. 7, no. 6, pp. 4105-4117, 2014.

[71] R. Sabetrasekh, H. Tiainen, S. P. Lyngstadaas, J. Reseland and H. Haugen, "A novel ultra-porous titanium dioxide ceramic with excellent biocompatibility," *Journal of Biomaterials Applications,* vol. 25, no. 6, pp. 559-580, 2010.

[72] G. Giavaresi, R. Giardino, L. Ambrosio, G. Battiston, R. Gerbasi, M. Fini, L. Rimondini and P. Torricelli, "In vitro biocompatibility of titanium dioxide for prosthetic devices nanostructured by low pressure metal-organic chemical vapor deposition," *The International Journal of Artificial Organs,* vol. 26, no. 8, pp. 774-780, 2003.

[73] U. Diebold, "The surface science of titanium dioxide," *Surface Science Reports,* vol. 48, no. 5-8, pp. 53-229, 2003.

[74] W. Souza, S. G. Piperni, P. Laviola, A. L. Rossi, M. I. D. Rossi, B. S. Archanjo, P. E. Leite, M. H. Fernandes, L. A. Rocha, J. M. Granjeiro and A. R. Ribeiro, "The two faces of titanium dioxide nanoparticles bio-camouflage in 3D bone spheroids," *Scientific Reports,* vol. 9, p. 9309, 2019.

[75] A. M. Schrand, M. F. Rahman, S. M. Hussain, J. J. Schlager, D. A. Smith and A. F. Syed, "Metal-based nanoparticles and their toxicity assessment," *WIREs Nanomedicine and Nanobiotechnology,* vol. 2, no. 5, pp. 544-568, 2010.

[76] L. K. Braydich-Stolle, N. M. Schaeublin, R. C. Murdock, J. Jiang, P. Biswas, J. J. Schlager and S. M. Hussain, "Crystal structure mediates mode of cell death in TiO2 toxicity," *Journal of Nanoparticle Research,* vol. 11, no. 6, pp. 1361-1374, 2009.

[77] Z. E. Allouni, P. J. Hol, M. A. Cauqui, N. R. Gjerdet and M. R. Cimpan, "Role of physicochemical characteristics in the uptake of TiO2 nanoparticles by fibroblasts," *Toxicology in Vitro,* vol. 26, pp. 469-479, 2012.

[78] A. Elsaesser and C. V. Howard, "Toxicology of nanoparticles," *Advanced Drug Delivery Reviews,* vol. 64, pp. 129-137, 2012.

[79] J. Wang, G. Zhou, C. Chen, H. Yu, T. Wang, Y. Ma, G. Jia, Y. Gao, B. Li, J. Sun, Y. Li, F. Jian, Y. Zhao and Z. Chai, "Acute toxicity and biodistribution of different sized titanium dioxide particles in mice after oral administration," *Toxicology Letters,* vol. 168, no. 2, pp. 176-185, 2007.

[80] K. Donaldson, D. Brown, A. Clouter, R. Duffin, W. MacNee, L. Renwick, L. Tran and V. Stone, "The pulmonary toxicology of ultrafine particles," *Journal of Aerosol Medicine,* vol. 15, no. 2, pp. 213-220, 2004.

[81] H. S. Choi, Y. Ashitate, J. H. Lee, S. H. Kim, A. Matsui, N. Insin, M. G. Bawendi, M. Semmler-Behnke, J. V. Frangioni and A. Tsuda, "Rapid translocation of nanoparticles from the lung airspaces to the body," *Nature Biotechnology,* vol. 28, no. 12, pp. 1300-1303, 2010.

[82] J. Wu, W. Liu, C. Xue, S. Zhou, F. Lan, L. Bi, H. Xu, X. Yang and F.-D. Zeng, "Toxicity and penetration of TiO2 nanoparticles in hairless mice and porcine skin after subchronic dermal exposure," *Toxicology Letters,* vol. 191, pp. 1-8, 2009.

[83] S. Linse, C. Cabaleiro-Lago, W.-F. Xue, I. Lynch, S. Lindman, E. Thulin, S. E. Radford and K. A. Dawson, "Nucleation of protein fibrillation by nanoparticles," *Proceedings of the National Academy of Sciences of the United States of America,* vol. 104, no. 21, pp. 8691-8696, 2007.

[84] G. Oberdorster, "Toxicokinetics and effects of fibrous and nonfibrous particles," *Inhalation Toxicology,* vol. 14, no. 1, pp. 29-56, 2002.

[85] P. K. Myllynen, M. J. Loughran, C. V. Howard, R. Sormunen, A. A. Walsh and K. H. Vähäkangas, "Kinetics of gold nanoparticles in the human placenta," *Reproductive Toxicology,* vol. 26, no. 2, pp. 130-137, 2008.

[86] T. Tsuchiya, I. Oguri, Y. N. Yamakoshi and N. Miyata, "Novel harmful effects of [60]fullerene on mouse embryos in vitro and in vivo," *FEBS Letters,* vol. 393, no. 1, pp. 139-145, 1996.

[87] M. Z. Rizk, S. A. Ali, M. A. Hamed, N. S. El-Rigal, H. F. Aly and H. H. Salah, "Toxicity of titanium dioxide nanoparticles: effect of dose and time on biochemical disturbance, oxidative stress and genotoxicity in mice," *Biomedicine & Pharmacotherapy,* vol. 90, pp. 466-472, 2017.

[88] M. Czajka, K. Sawicki, K. Sikorska, S. Popek, M. Kruszewski and L. Kapka-Skrzypczak, "Toxicity of titanium dioxide nanoparticles in central nervous system," *Toxicology in Vitro,* vol. 29, no. 5, pp. 1042-1052, 2015.

[89] K. L. Choy, "Chemical vapour deposition of coatings," *Progress in Materials Science,* vol. 48, no. 2, pp. 57-170, 2003.

[90] R. van de Krol, A. Goossens and J. Schoonman, "Mott-Schottky Analysis of Nanometer-Scale Thin-Film Anatase TiO2," *Journal of The Electrochemical Society,* vol. 144, p. 1723, 1997.

[91] P. Veluchamy, M. Tsuji, T. Nishio, T. Aramoto, H. Higuchi, S. Kumazawa, S. Shibutani, J. Nakajima, T. Arita, H. Ohyama, A. Hanafusa, T. Hibino and K. Omura, "A pyrosol process to deposit large-area SnO2:F thin films and its use as a transparent conducting substrate for CdTe solar cells," *Solare Energy Materials and Solar Cells,* vol. 67, no. 1-4, pp. 179-185, 2001.

[92] P. P. Ahonen, E. I. Kauppinen, J. C. Joubert, J. L. Deschanvres and G. van Tendeloo, "Preparation of nanocrystalline titania powder via aerosol pyrolysis of titanium tetrabutoxide," *Journal of Materials Research,* vol. 14, pp. 3938-3948, 1999.

[93] J. Rodríguez, M. Gómez, J. Ederth, G. A. Niklasson and C. G. Granqvist, "Thickness dependence of the optical properties of sputter deposited Ti oxide films," *Thin Solid Films,* vol. 265, no. 1, pp. 119-125, 2000.

[94] G. S. Herman and Y. Gao, "Growth of epitaxial anatase (001) and (101) films," *Thin Solid Films,* vol. 397, no. 1-2, pp. 157-161, 2001.

[95] R. Fromknecht, I. Khubeis, S. Massing and O. Meyer, "Ion implantation in TiO2: damage production and recovery, lattice site location and electrical conductivity," *Nuclear Instruments and Methods in Physics Research Section B: Beam Interactions with Materials and Atoms,* vol. 147, no. 1-4, pp. 191-201, 1999.

[96] S. Miyake, T. Kobayashi and M. Satou, "Titanium oxide formation by dynamic ion beam mixing," *Journal of Vacuum Science and Surface Technology A: Vacuum, Surfaces and Films,* vol. 9, no. 6, pp. 3036-3040, 1991.

[97] F. Pedraza and A. Vazquez, "Obtention of TiO2 rutile at room temperature through direct oxidation of TiCl3," *Journal of Physics and Chemistry of Solids,* vol. 60, no. 4, pp. 445-448, 1999.

[98] Y. V. Kolen'ko, A. A. Burukhin, B. R. Churagulov and N. N. Oleynikov, "Synthesis of nanocrystalline TiO2 powders from aqueous TiOSO4 solutions under hydrothermal conditions," *Materials Letters,* vol. 57, no. 5-6, pp. 1124-1129, 2003.

[99] S. Yin, Y. Fujishiro, J. Wu, M. Aki and T. Sato, "Synthesis and photocatalytic properties of fibrous titania by solvothermal reactions," *Journal of Materials Processing Technology,* vol. 137, no. 1-3, pp. 45-48, 2003.

[100] R. Zhang and L. Gao, "Preparation of nanosized titania by hydrolysis of alkoxide titanium in micelles," *Materials Research Bulletin,* vol. 37, no. 9, pp. 1659-1666, 2002.

[101] K. Nagaveni, G. Sivalingam, M. S. Hegde and G. Madras, "Solar photocatalytic degradation of dyes: high activity combustion synthesized nano TiO2," *Applied Catalysis B: Environmental,* vol. 48, no. 2, pp. 83-93, 2004.

[102] Y. Ishikawa and Y. Matsumoto, "Electrodeposition of TiO2 photocatalyst into nano-pores of hard alumite," *Electrochimica Acta,* vol. 46, no. 18, pp. 2819-2824, 2001.

[103] S. Sivakumar, P. K. Pillai, P. Mukundan and K. G. K. Warrier, "Sol-gel synthesis of nanosized anatase from titanyl sulfate," *Materials Letters,* vol. 57, no. 2, pp. 330-335, 2002.

[104] S. M. Gupta and M. Tripathi, "A review on the synthesis of TiO2 nanoparticles by solution route," *Central European Journal of Chemistry,* vol. 10, no. 2, pp. 279-294, 2011.

[105] Y.-F. Chen, C.-Y. Lee, M.-Y. Yeng and H.-T. Chiu, "The effect of calcination temperature on the crystallinity of TiO2 nanopowders," *Journal of Crystal Growth,* vol. 247, no. 3, pp. 363-370, 2003.

[106] D. B. Williams and C. B. Carter, Transmission Electron Microscopy, New York: Springer, 2009.

[107] Hitachi High-Technologies Corporation, Let's Familiarize Ourselves with the SEM!, Tokyo, 2016.

[108] C. Chen, W. Cai, M. Long, J. Zhang, B. Zhou, Y. Wu and D. Wu, "Template-free sol-gel preparation and characterization of free-standing visible light responsive C,N-modified porous monolithic TiO2," *Journal of hazardous materials,* vol. 178, no. 1-3, pp. 560-565, 2010.

[109] T. M. Knowlton and S. Dhodapkar, "Section 17: Gas-Solid Operations and Equipment," in *Perry's Chemical Engineers' Handbook*, McGraw-Hill Education, 2019.

[110] F. Ahmed, *Synthesis and characterization of Fe-doped TiO2 on fiberglass cloth for the wastewater treatment reactor,* Victoria: University of Victoria, 2020.

[111] "Anatase R060277 - RRUFF Database: Raman, X-ray, Infrared and Chemistry," [Online]. Available: http://rruff.info/Anatase/R060277. [Accessed 1 March 2022].

[112] A. P. Lange, A. Samanta, H. Majidi, S. Mahajan, J. Ging, T. Y. Olson, K. van Benthem and S. Elhadj, "Dislocation mediated alignment during metal nanoparticle coalescence," *Acta Materialia,* vol. 120, pp. 364-378, 2016.

[113] J. W. Edington, *Monograph Two: Electron Diffraction in the Electron Microscope,* Cambridge: The MacMillan Press Ltd, 1975.

[114] S. Bagheri, K. Shameli and S. B. A. Hamid, "Synthesis and Characterization of Anatase Titanium Dioxide Nanoparticles Using Egg White Solution via Sol-Gel Method," *Journal of Chemistry,* vol. 6, 2013.

[115] S. Sood, A. Umar, S. K. Mehta and S. Kansal, "Highly effective Fe-doped TiO2 nanoparticles photocatalysts for visible-light driven photocatalytic degradation of toxic organic compounds," *Journal of Colloid and Interface Science,* vol. 450, pp. 213-223, 2015.

Appendix A

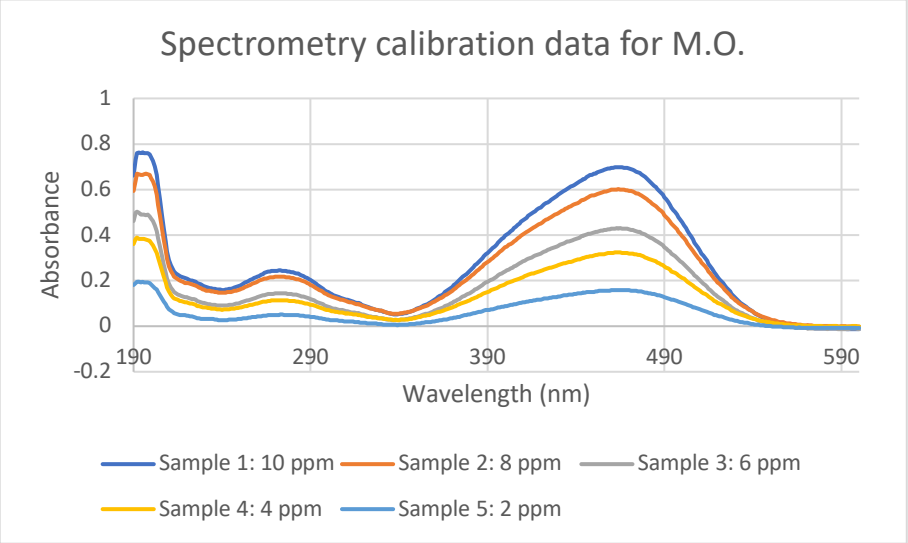

Figure 68 Absorbance measurements of standard solutions of Methyl Orange (M.O.), for a range of wavelengths

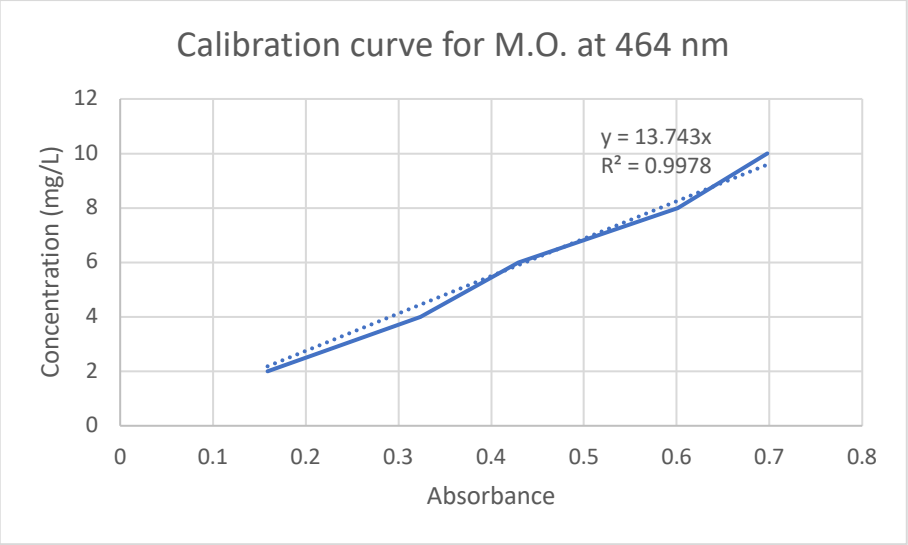

Figure 69 Calibration curve extracted from spectrometry data of Methyl Orange standard solutions

Appendix B

- Secondary electron pictures taken at 700x magnification

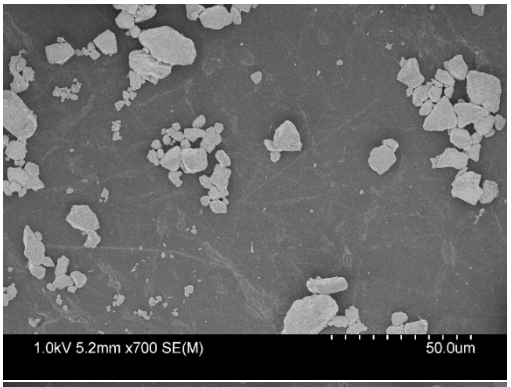

Size (µm)	Count	Volume (µm^3)	Surface (µm^2)
0	0	0	0
0.1	0	0	0
0.5	2	0.052186	0.849729
1	30	8.021426	58.57762
5	174	2134.3	3746.296
10	63	13253.78	10362.24
50	15	32961.87	11423.52

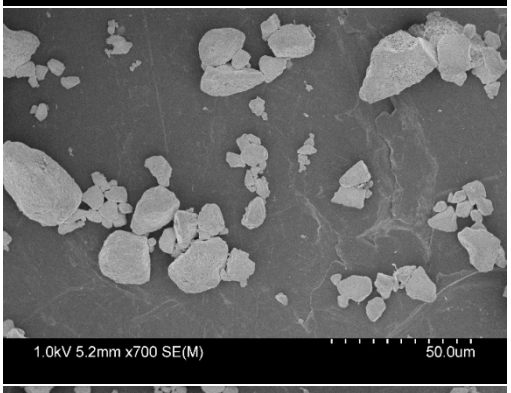

Size (µm)	Count	Volume (µm^3)	Surface (µm^2)
0	0	0	0
0.1	0	0	0
0.5	0	0	0
1	0	0	0
5	58	1290.625	2048.269
10	39	7074.165	5857.272
50	22	80138.77	21778.81

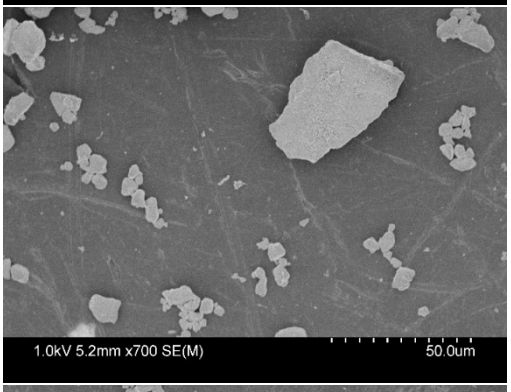

Size (µm)	Count	Volume (µm^3)	Surface (µm^2)
0	0	0	0
0.1	0	0	0
0.5	0	0	0
1	0	0	0
5	69	1138.355	1998.074
10	30	5820.831	4665.878
50	9	9783.209	4544.905

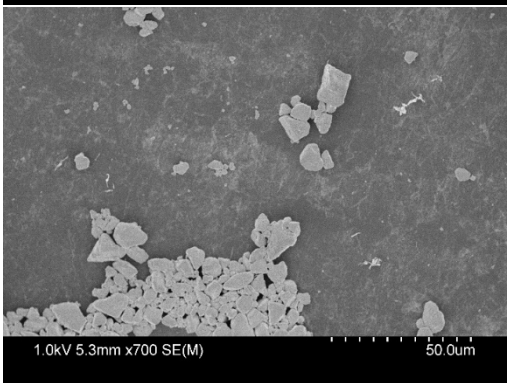

Size (µm)	Count	Volume (µm^3)	Surface (µm^2)
0	0	0	0
0.1	0	0	0
0.5	0	0	0
1	4	1.102527	8.009883
5	187	2637.932	4649.724
10	54	7466.149	6852.425
50	14	11787.24	5968.405

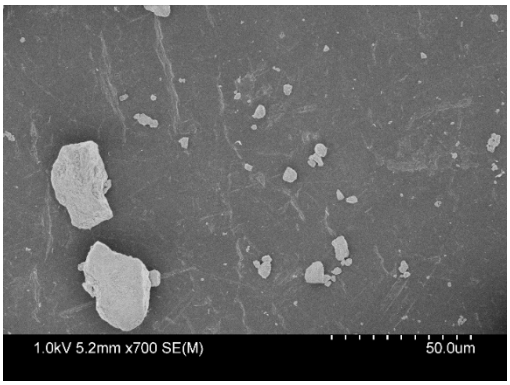

Size (µm)	Count	Volume ($µm^3$)	Surface ($µm^2$)
0	0	0	0
0.1	0	0	0
0.5	1	0.040194	0.56745
1	8	3.035449	19.93037
5	89	984.1148	1811.403
10	9	1991.277	1525.504
50	2	34201.58	6412.36

- Secondary electron pictures taken at 3000x magnification

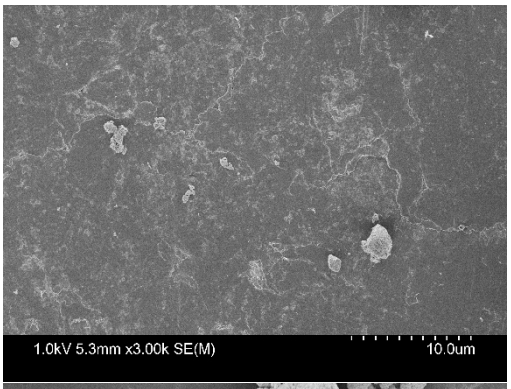

Size (µm)	Count	Volume (μm^3)	Surface (μm^2)
0	0	0	0
0.1	3	0.000583	0.04812
0.5	19	0.29201	5.092782
1	11	2.763649	20.53013
5	3	12.34368	34.60493
10	0	0	0
50	0	0	0

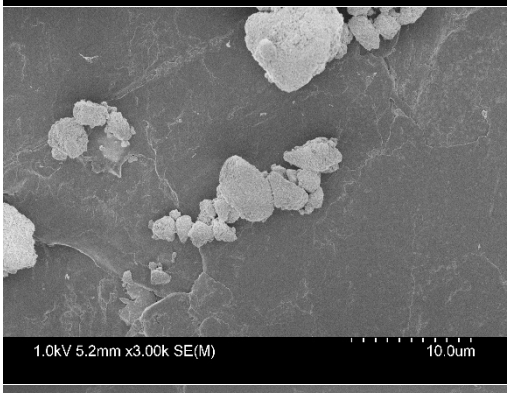

Size (µm)	Count	Volume (μm^3)	Surface (μm^2)
0	0	0	0
0.1	0	0	0
0.5	26	0.628713	9.424552
1	14	2.20425	19.36434
5	24	211.4059	425.2757
10	3	431.8405	388.452
50	0	0	0

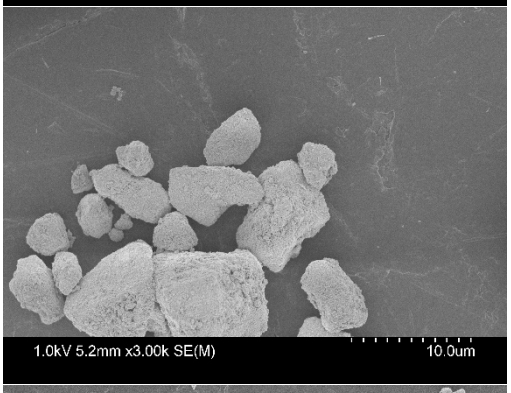

Size (µm)	Count	Volume (μm^3)	Surface (μm^2)
0	0	0	0
0.1	0	0	0
0.5	18	0.369295	5.956117
1	8	1.263228	11.05998
5	10	192.098	322.2968
10	7	1098.051	964.1302
50	1	751.4947	399.7312

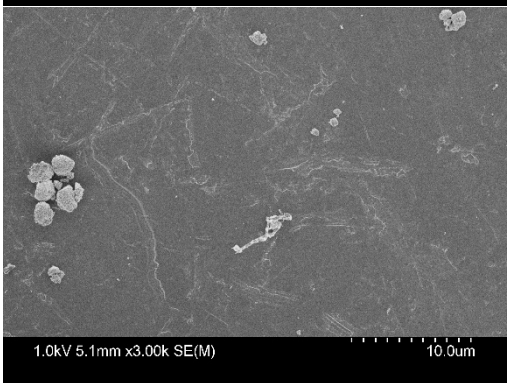

Size (µm)	Count	Volume (μm^3)	Surface (μm^2)
0	0	0	0
0.1	2	0.00061	0.04381
0.5	25	0.341195	6.07301
1	6	1.200954	9.708822
5	10	24.12807	83.39009
10	0	0	0
50	0	0	0

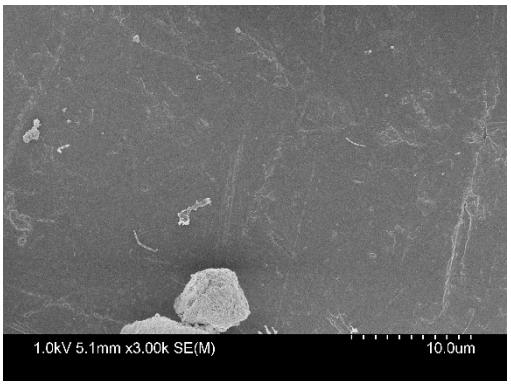

Size (µm)	Count	Volume (μm^3)	Surface (μm^2)
0	0	0	0
0.1	1	0.000508	0.030791
0.5	11	0.232722	3.660757
1	4	0.889373	6.975806
5	0	0	0
10	2	383.7902	309.5305
50	0	0	0

- Secondary electron pictures taken at 6000x magnification

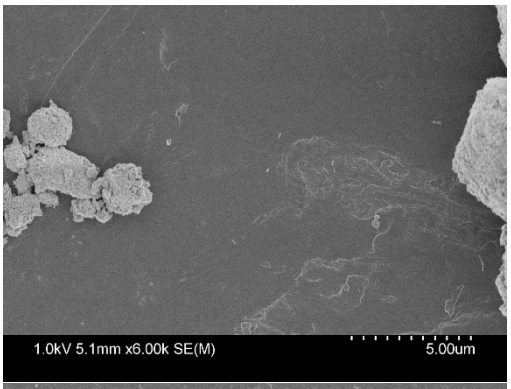

Size (µm)	Count	Volume (μm^3)	Surface (μm^2)
0	0	0	0
0.1	1	0.00018	0.015394
0.5	26	0.350997	6.574037
1	5	1.625612	11.25135
5	8	23.73195	71.10017
10	1	112.3638	112.6078
50	0	0	0

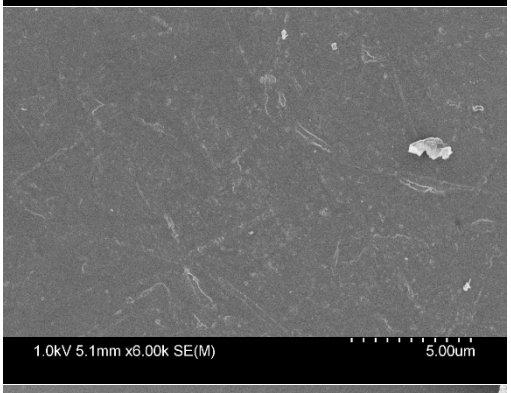

Size (µm)	Count	Volume (μm^3)	Surface (μm^2)
0	0	0	0
0.1	5	0.001072	0.0816
0.5	7	0.068251	1.278063
1	0	0	0
5	0	0	0
10	0	0	0
50	0	0	0

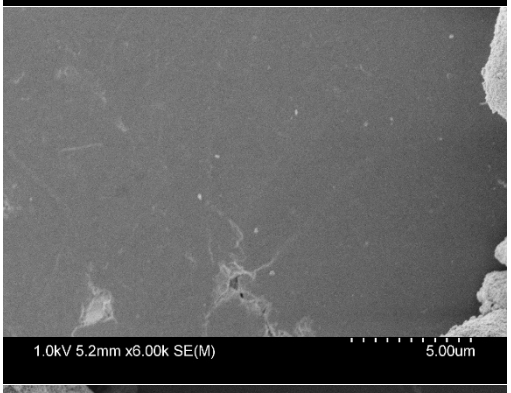

Size (µm)	Count	Volume (μm^3)	Surface (μm^2)
0	0	0	0
0.1	1	0.000369	0.024885
0.5	8	0.040264	1.075719
1	0	0	0
5	0	0	0
10	0	0	0
50	0	0	0

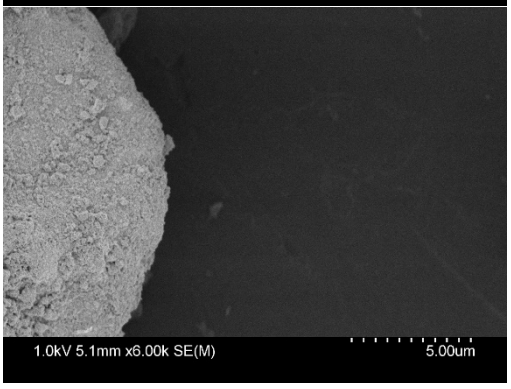

The particles in this picture were not counted as small particles resting on top of a bigger particle cannot be distinguished from surface features of the bigger particle.

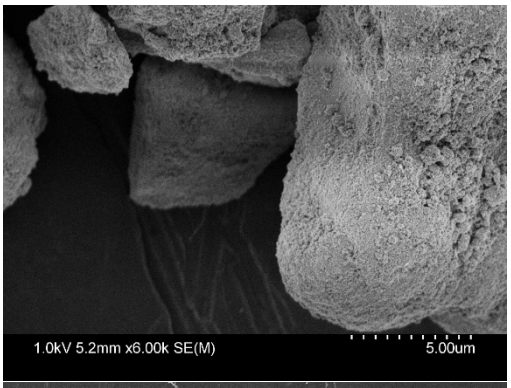

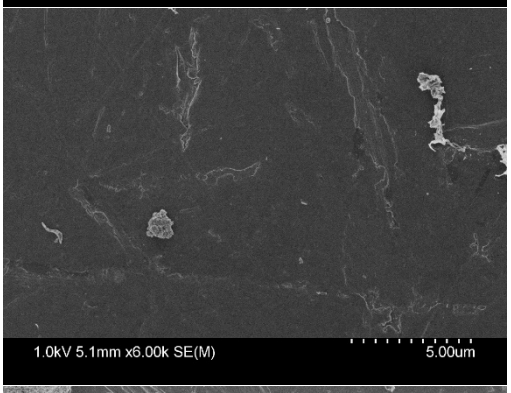

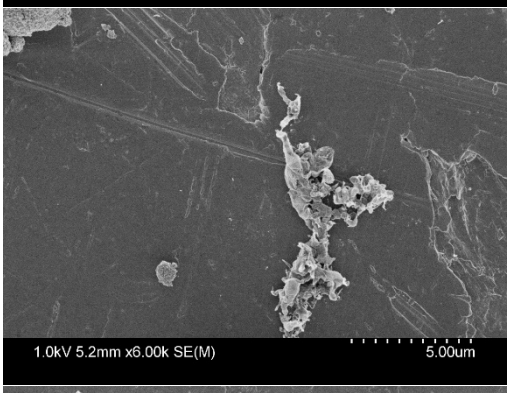

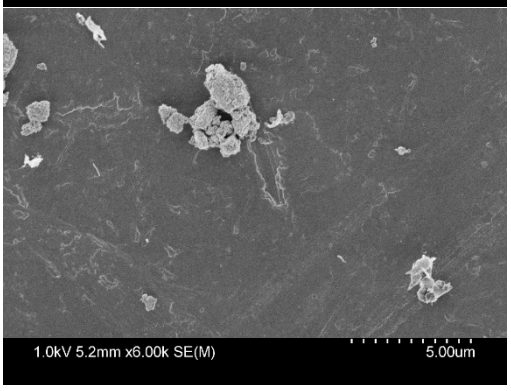

The particles in this picture were not counted as small particles resting on top of a bigger particle cannot be distinguished from surface features of the bigger particle.

Size (µm)	Count	Volume (μm^3)	Surface (μm^2)
0	0	0	0
0.1	14	0.002679	0.208341
0.5	3	0.012702	0.366413
1	0	0	0
5	1	0.668787	3.698361
10	0	0	0
50	0	0	0

Size (µm)	Count	Volume (μm^3)	Surface (μm^2)
0	0	0	0
0.1	10	0.001038	0.102479
0.5	9	0.102939	1.758547
1	1	0.165364	1.456948
5	1	0.630701	3.556584
10	0	0	0
50	0	0	0

Size (µm)	Count	Volume (μm^3)	Surface (μm^2)
0	0	0	0
0.1	2	0.000597	0.039911
0.5	8	0.273622	3.963892
1	9	2.487441	18.0734
5	2	5.617819	18.19409
10	0	0	0
50	0	0	0

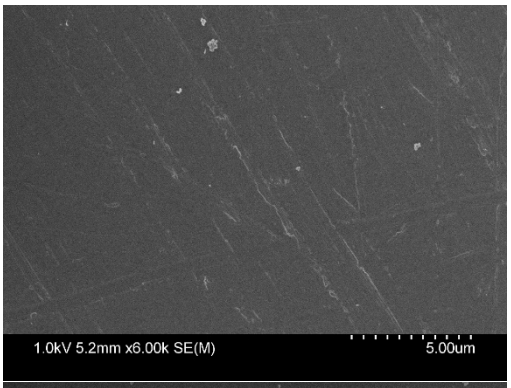

Size (µm)	Count	Volume (µm^3)	Surface (µm^2)
0	0	0	0
0.1	15	0.002636	0.223977
0.5	7	0.076189	1.398643
1	0	0	0
5	0	0	0
10	0	0	0
50	0	0	0

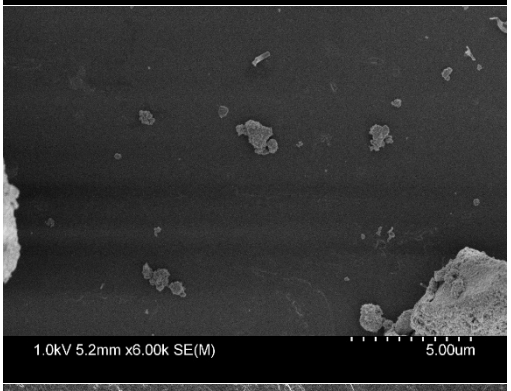

Size (µm)	Count	Volume (µm^3)	Surface (µm^2)
0	0	0	0
0.1	13	0.002886	0.217207
0.5	26	0.434552	7.306836
1	8	1.562464	12.59792
5	4	61.27861	86.41464
10	0	0	0
50	0	0	0

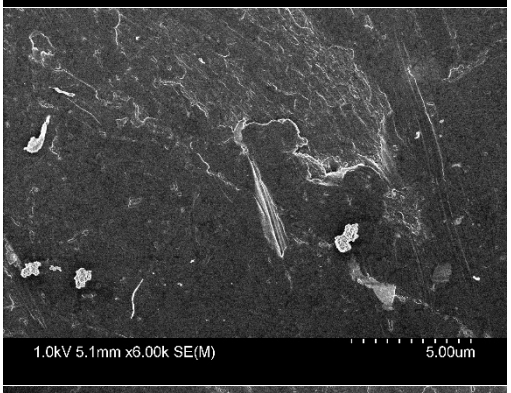

Size (µm)	Count	Volume (µm^3)	Surface (µm^2)
0	0	0	0
0.1	5	0.001698	0.113672
0.5	7	0.039716	0.978506
1	3	0.841126	6.189308
5	1	0.607864	3.470206
10	0	0	0
50	0	0	0

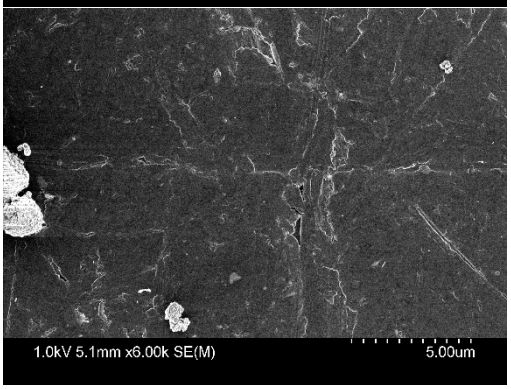

Size (µm)	Count	Volume (µm^3)	Surface (µm^2)
0	0	0	0
0.1	3	0.000524	0.043687
0.5	1	0.031059	0.477836
1	2	0.160373	1.798461
5	2	3.960879	14.86161
10	0	0	0
50	0	0	0

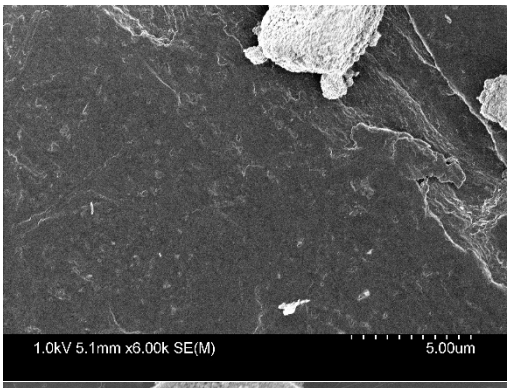

Size (µm)	Count	Volume (µm^3)	Surface (µm^2)
0	0	0	0
0.1	9	0.000947	0.090487
0.5	1	0.005964	0.159043
1	2	0.645952	4.532995
5	1	0.792181	4.140318
10	1	92.79229	99.11941
50	0	0	0

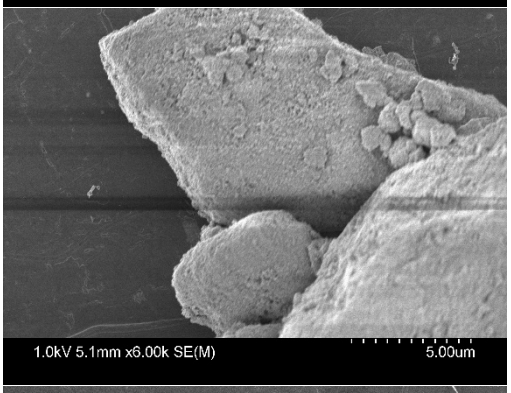

Size (µm)	Count	Volume (µm^3)	Surface (µm^2)
0	0	0	0
0.1	0	0	0
0.5	0	0	0
1	0	0	0
5	0	0	0
10	0	0	0
50	0	0	0

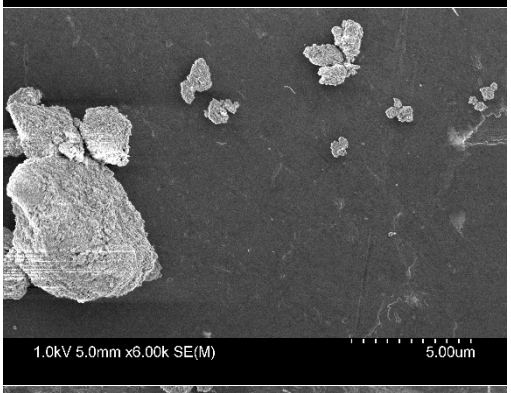

Size (µm)	Count	Volume (µm^3)	Surface (µm^2)
0	0	0	0
0.1	3	0.000925	0.063627
0.5	4	0.061011	1.04922
1	3	0.495368	4.351568
5	10	43.58532	112.3958
10	1	175.5458	151.6158
50	0	0	0

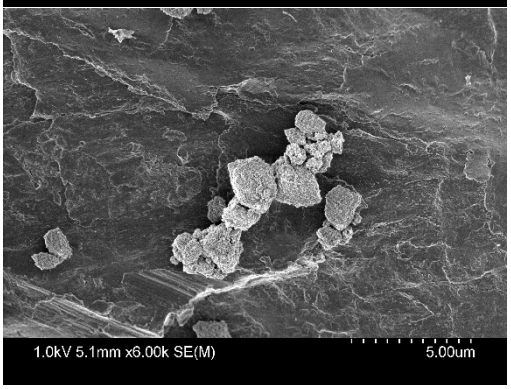

Size (µm)	Count	Volume (µm^3)	Surface (µm^2)
0	0	0	0
0.1	0	0	0
0.5	0	0	0
1	7	2.59149	17.0578
5	8	21.96909	71.32867
10	0	0	0
50	0	0	0

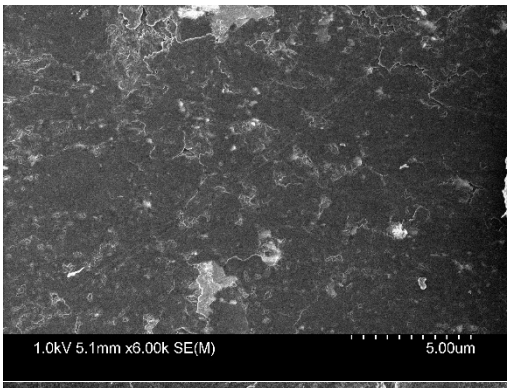

Size (µm)	Count	Volume (µm^3)	Surface (µm^2)
0	0	0	0
0.1	1	0.000102	0.010568
0.5	2	0.038556	0.580268
1	0	0	0
5	0	0	0
10	0	0	0
50	0	0	0

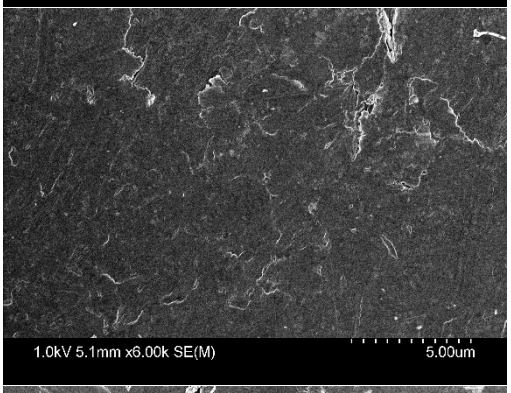

Size (µm)	Count	Volume (µm^3)	Surface (µm^2)
0	0	0	0
0.1	7	0.001024	0.090827
0.5	7	0.016856	0.590497
1	0	0	0
5	0	0	0
10	0	0	0
50	0	0	0

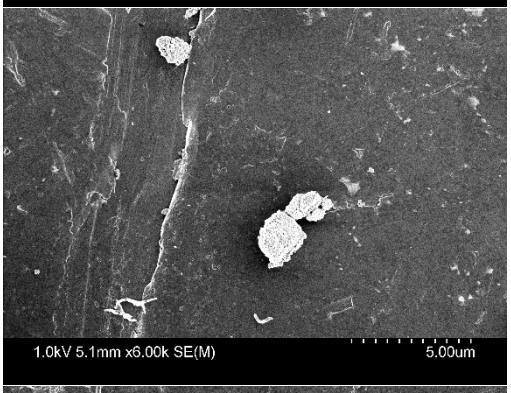

Size (µm)	Count	Volume (µm^3)	Surface (µm^2)
0	0	0	0
0.1	5	0.001162	0.08798
0.5	12	0.105613	2.063828
1	2	0.412805	3.372336
5	3	6.616959	24.23272
10	0	0	0
50	0	0	0

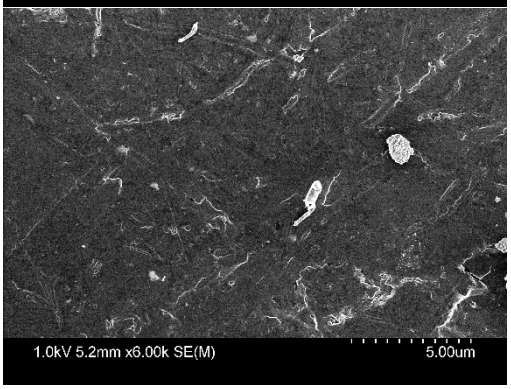

Size (µm)	Count	Volume (µm^3)	Surface (µm^2)
0	0	0	0
0.1	4	0.000636	0.056159
0.5	5	0.059511	1.114559
1	1	0.078838	0.889146
5	1	0.568824	3.319985
10	0	0	0
50	0	0	0

- Secondary electron pictures taken at 18000x magnification

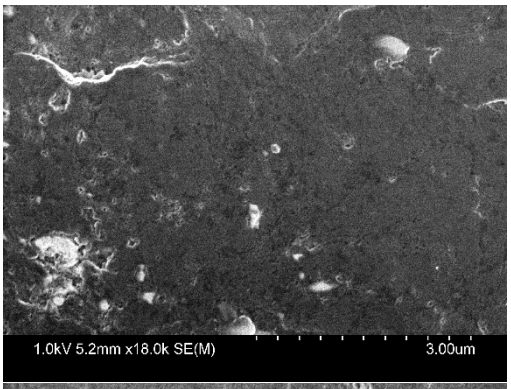

Size (µm)	Count	Volume (µm^3)	Surface (µm^2)
0	0	0	0
0.1	1	4.46E-05	0.006082
0.5	0	0	0
1	0	0	0
5	0	0	0
10	0	0	0
50	0	0	0

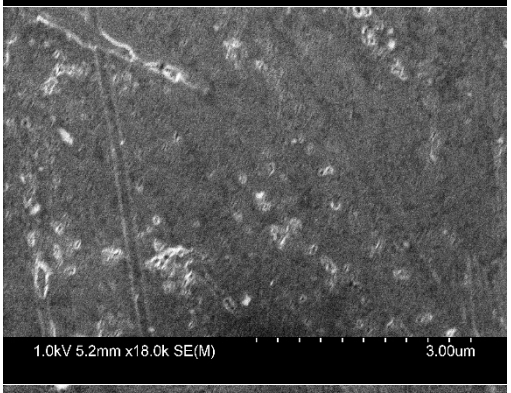

Size (µm)	Count	Volume (µm^3)	Surface (µm^2)
0	0	0	0
0.1	0	0	0
0.5	0	0	0
1	0	0	0
5	0	0	0
10	0	0	0
50	0	0	0

Size (µm)	Count	Volume (µm^3)	Surface (µm^2)
0	0	0	0
0.1	2	3.92E-05	0.006742
0.5	1	0.003648	0.114608
1	0	0	0
5	0	0	0
10	0	0	0
50	0	0	0

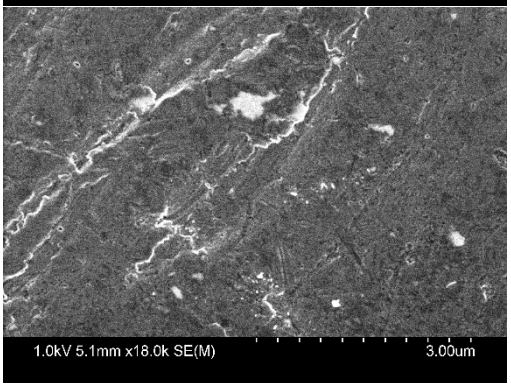

Size (µm)	Count	Volume (µm^3)	Surface (µm^2)
0	0	0	0
0.1	0	0	0
0.5	1	0.001124	0.052279
1	0	0	0
5	0	0	0
10	0	0	0
50	0	0	0

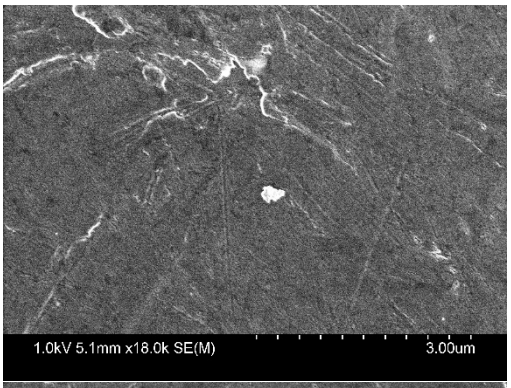

Size (µm)	Count	Volume (µm^3)	Surface (µm^2)
0	0	0	0
0.1	1	4.16E-05	0.005809
0.5	1	0.018141	0.333876
1	0	0	0
5	0	0	0
10	0	0	0
50	0	0	0

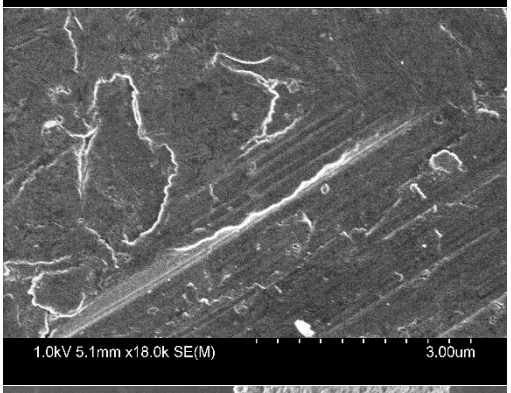

Size (µm)	Count	Volume (µm^3)	Surface (µm^2)
0	0	0	0
0.1	2	6.48E-05	0.009817
0.5	1	0.012903	0.266033
1	0	0	0
5	0	0	0
10	0	0	0
50	0	0	0

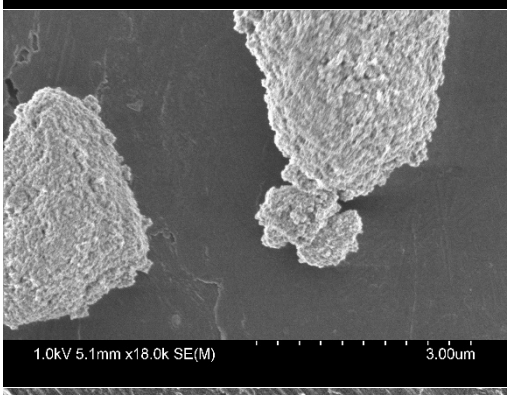

Size (µm)	Count	Volume (µm^3)	Surface (µm^2)
0	0	0	0
0.1	0	0	0
0.5	0	0	0
1	0	0	0
5	3	38.74269	74.23205
10	0	0	0
50	0	0	0

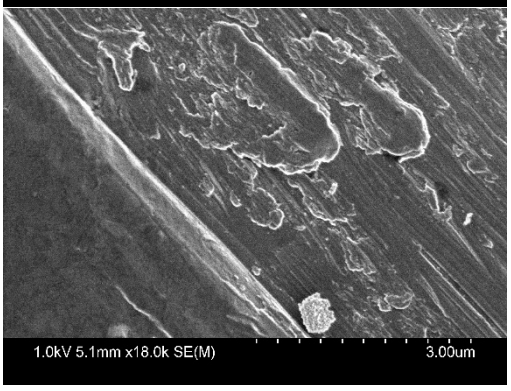

Size (µm)	Count	Volume (µm^3)	Surface (µm^2)
0	0	0	0
0.1	0	0	0
0.5	2	0.004921	0.176284
1	1	0.073622	0.849487
5	0	0	0
10	0	0	0
50	0	0	0

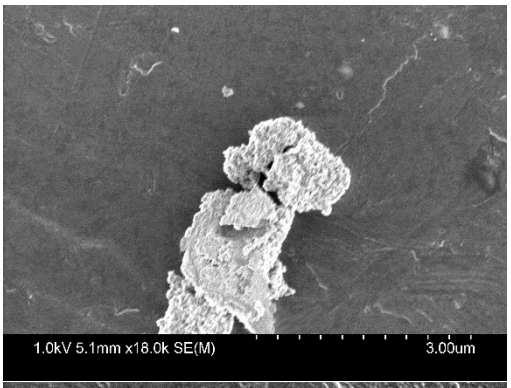

Size (µm)	Count	Volume (µm^3)	Surface (µm^2)
0	0	0	0
0.1	1	0.000435	0.027759
0.5	1	0.001468	0.062458
1	0	0	0
5	3	6.100748	22.13074
10	0	0	0
50	0	0	0

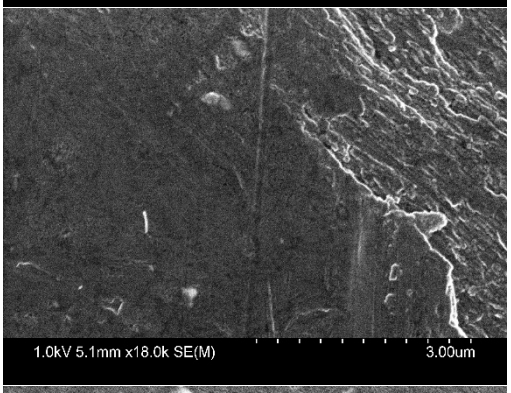

Size (µm)	Count	Volume (µm^3)	Surface (µm^2)
0	0	0	0
0.1	0	0	0
0.5	0	0	0
1	0	0	0
5	0	0	0
10	0	0	0
50	0	0	0

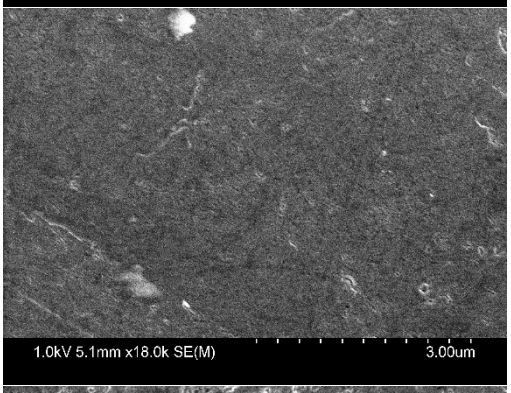

Size (µm)	Count	Volume (µm^3)	Surface (µm^2)
0	0	0	0
0.1	1	0.000137	0.012868
0.5	1	0.001232	0.055572
1	0	0	0
5	0	0	0
10	0	0	0
50	0	0	0

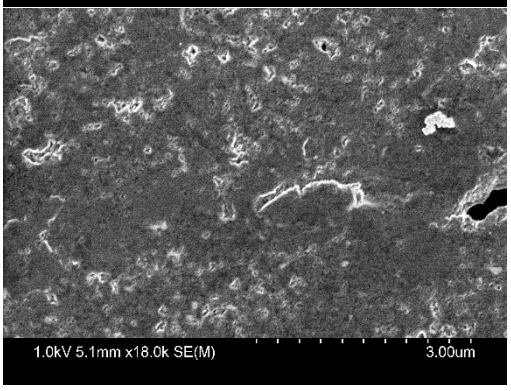

Size (µm)	Count	Volume (µm^3)	Surface (µm^2)
0	0	0	0
0.1	0	0	0
0.5	1	0.026737	0.432412
1	0	0	0
5	0	0	0
10	0	0	0
50	0	0	0

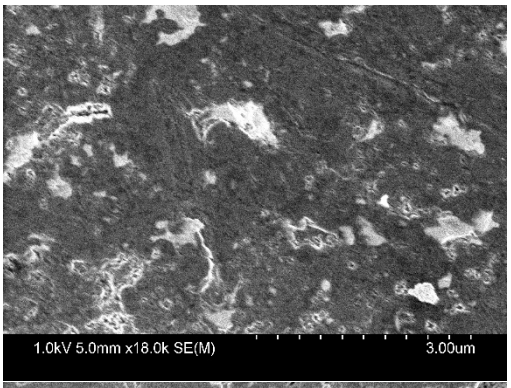

Size (µm)	Count	Volume (µm^3)	Surface (µm^2)
0	0	0	0
0.1	0	0	0
0.5	2	0.034998	0.574095
1	0	0	0
5	0	0	0
10	0	0	0
50	0	0	0

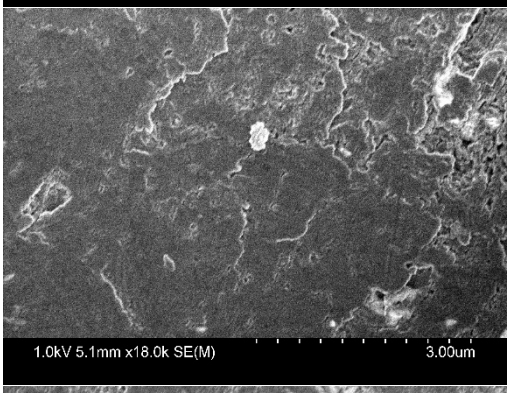

Size (µm)	Count	Volume (µm^3)	Surface (µm^2)
0	0	0	0
0.1	0	0	0
0.5	1	0.026522	0.430084
1	0	0	0
5	0	0	0
10	0	0	0
50	0	0	0

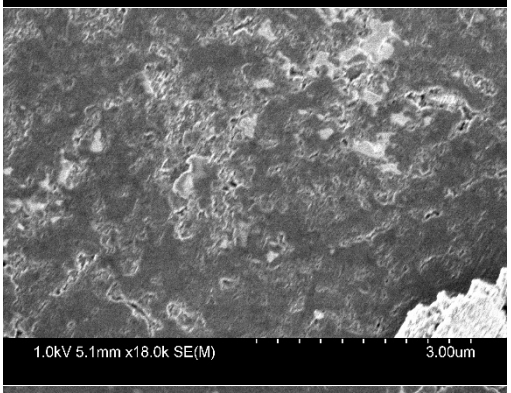

Size (µm)	Count	Volume (µm^3)	Surface (µm^2)
0	0	0	0
0.1	0	0	0
0.5	1	0.001177	0.053913
1	0	0	0
5	0	0	0
10	0	0	0
50	0	0	0

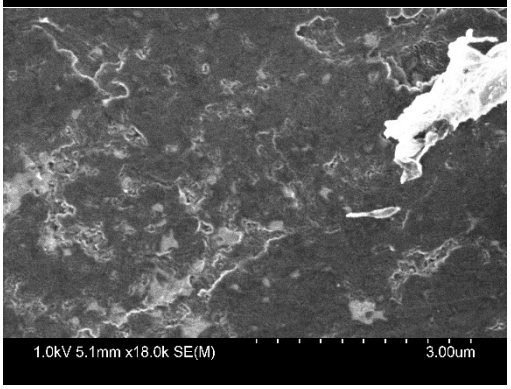

Size (µm)	Count	Volume (µm^3)	Surface (µm^2)
0	0	0	0
0.1	0	0	0
0.5	0	0	0
1	0	0	0
5	0	0	0
10	0	0	0
50	0	0	0

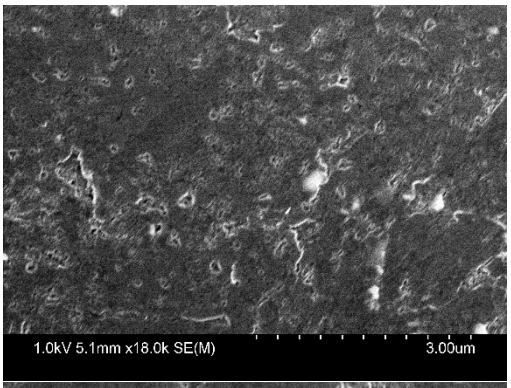

Size (µm)	Count	Volume (µm^3)	Surface (µm^2)
0	0	0	0
0.1	0	0	0
0.5	0	0	0
1	0	0	0
5	0	0	0
10	0	0	0
50	0	0	0

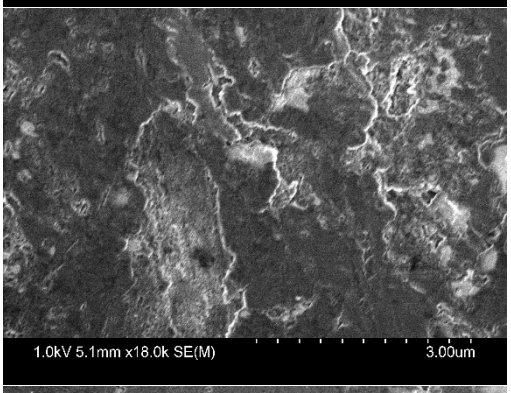

Size (µm)	Count	Volume (µm^3)	Surface (µm^2)
0	0	0	0
0.1	0	0	0
0.5	0	0	0
1	0	0	0
5	0	0	0
10	0	0	0
50	0	0	0

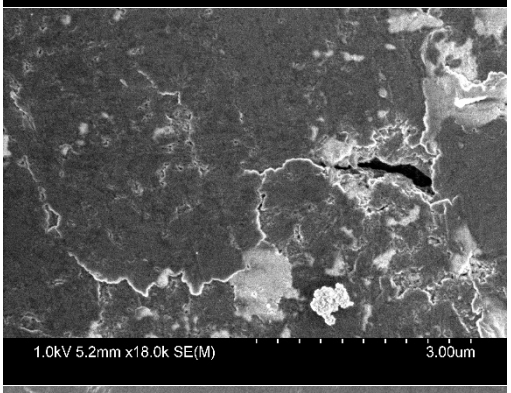

Size (µm)	Count	Volume (µm^3)	Surface (µm^2)
0	0	0	0
0.1	2	0.000108	0.01267
0.5	0	0	0
1	1	0.08759	0.953791
5	0	0	0
10	0	0	0
50	0	0	0

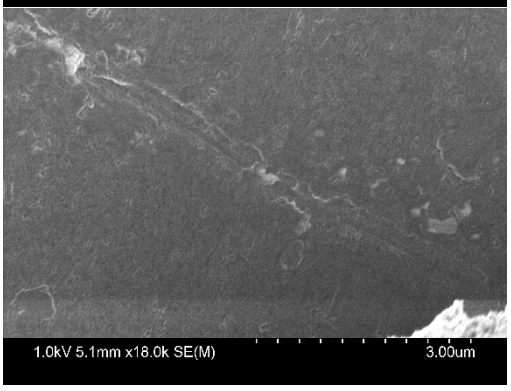

Size (µm)	Count	Volume (µm^3)	Surface (µm^2)
0	0	0	0
0.1	0	0	0
0.5	0	0	0
1	0	0	0
5	0	0	0
10	0	0	0
50	0	0	0

- Secondary electron pictures taken at 30000x magnification

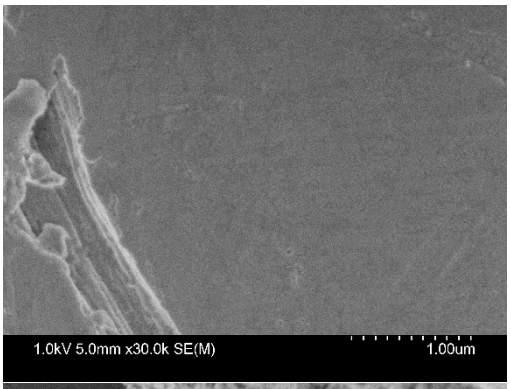

Size (µm)	Count	Volume (µm^3)	Surface (µm^2)
0	0	0	0
0.1	1	2.87E-05	0.004536
0.5	0	0	0
1	0	0	0
5	0	0	0
10	0	0	0
50	0	0	0

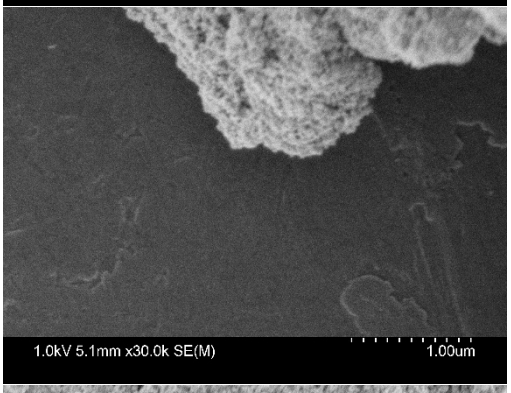

Size (µm)	Count	Volume (µm^3)	Surface (µm^2)
0	0	0	0
0.1	0	0	0
0.5	0	0	0
1	0	0	0
5	0	0	0
10	0	0	0
50	0	0	0

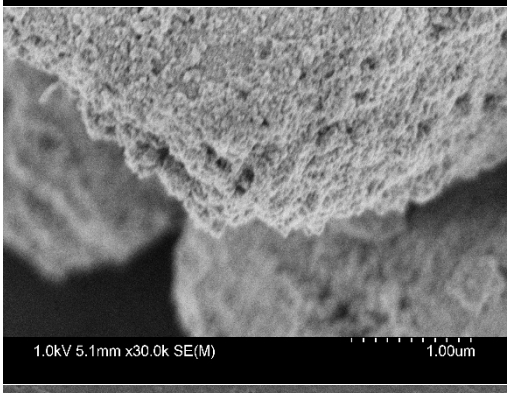

Size (µm)	Count	Volume (µm^3)	Surface (µm^2)
0	0	0	0
0.1	0	0	0
0.5	0	0	0
1	0	0	0
5	0	0	0
10	0	0	0
50	0	0	0

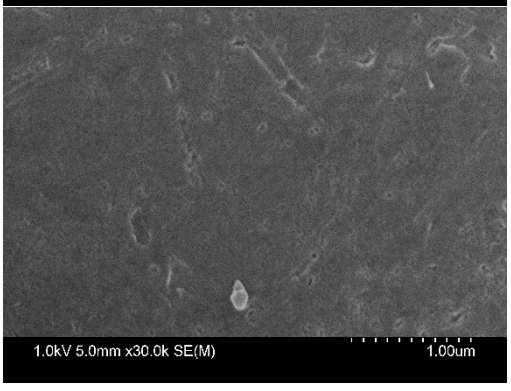

Size (µm)	Count	Volume (µm^3)	Surface (µm^2)
0	0	0	0
0.1	0	0	0
0.5	1	0.004064	0.123163
1	0	0	0
5	0	0	0
10	0	0	0
50	0	0	0

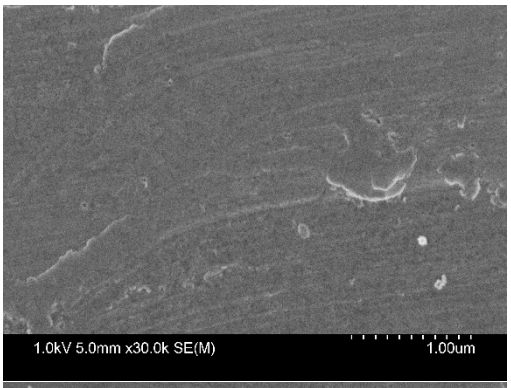

Size (µm)	Count	Volume ($µm^3$)	Surface ($µm^2$)
0	0	0	0
0.1	3	0.000591	0.048767
0.5	0	0	0
1	0	0	0
5	0	0	0
10	0	0	0
50	0	0	0

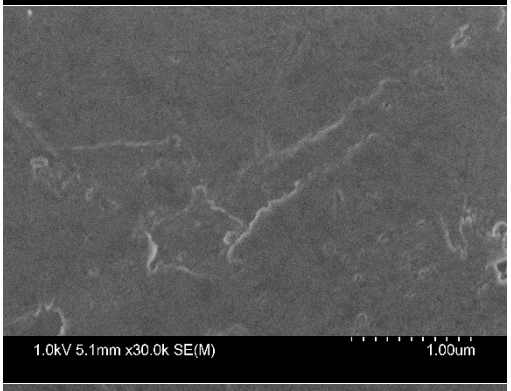

Size (µm)	Count	Volume ($µm^3$)	Surface ($µm^2$)
0	0	0	0
0.1	1	4.46E-05	0.006082
0.5	0	0	0
1	0	0	0
5	0	0	0
10	0	0	0
50	0	0	0

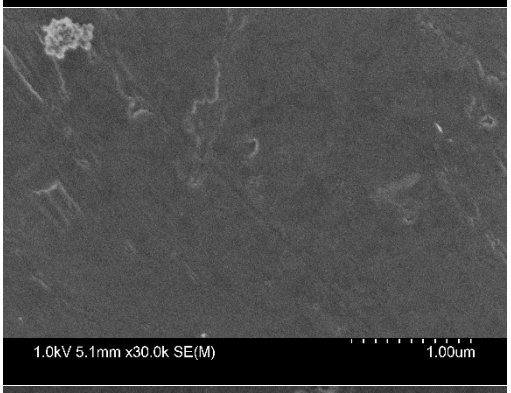

Size (µm)	Count	Volume ($µm^3$)	Surface ($µm^2$)
0	0	0	0
0.1	1	3.11E-05	0.004778
0.5	1	0.017481	0.325733
1	0	0	0
5	0	0	0
10	0	0	0
50	0	0	0

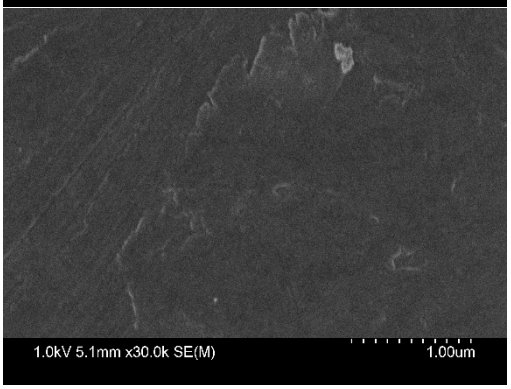

Size (µm)	Count	Volume ($µm^3$)	Surface ($µm^2$)
0	0	0	0
0.1	1	1.56E-05	0.003019
0.5	1	0.003535	0.112221
1	0	0	0
5	0	0	0
10	0	0	0
50	0	0	0

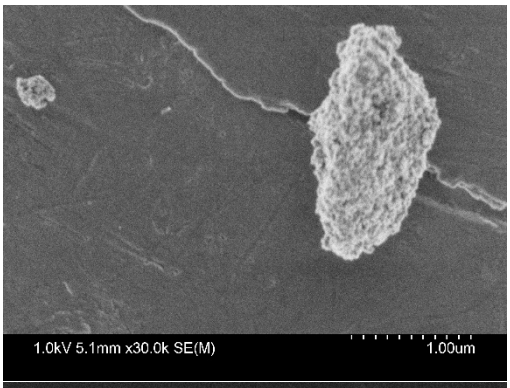

Size (µm)	Count	Volume (µm^3)	Surface (µm^2)
0	0	0	0
0.1	0	0	0
0.5	1	0.015599	0.301907
1	0	0	0
5	1	1.784876	7.115786
10	0	0	0
50	0	0	0

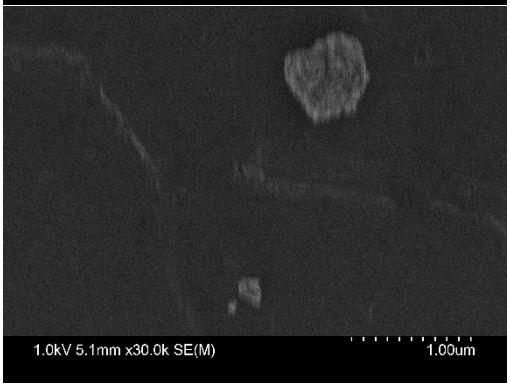

Size (µm)	Count	Volume (µm^3)	Surface (µm^2)
0	0	0	0
0.1	1	0.000268	0.020106
0.5	1	0.004989	0.141196
1	1	0.214766	1.734313
5	0	0	0
10	0	0	0
50	0	0	0

Appendix C

- Selected details of the EDX spectrum collected at “Point 2”

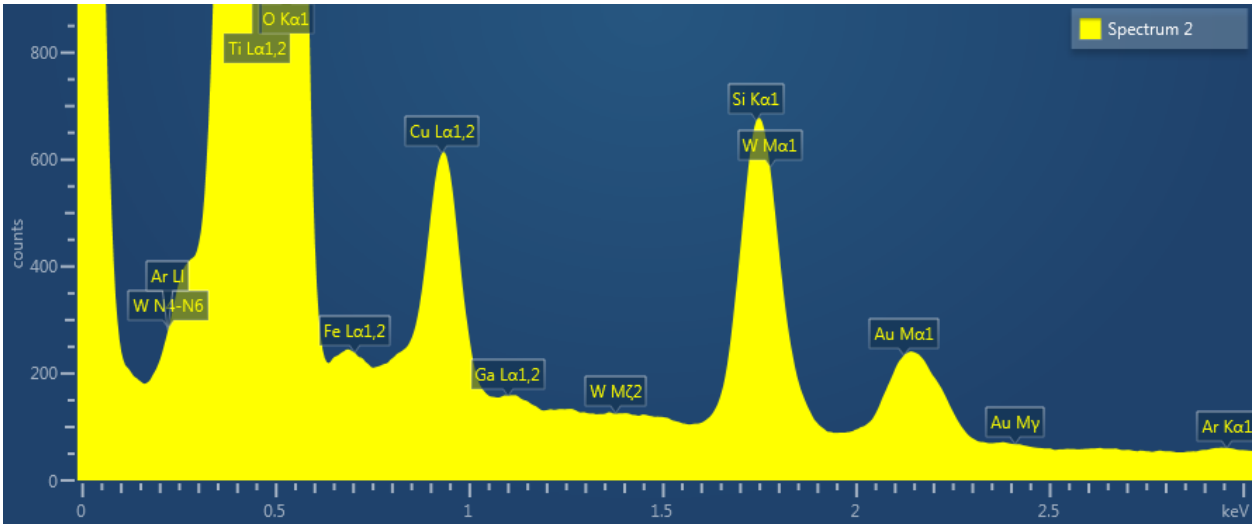

Figure 70 Zoomed-in detail of the EDX spectrum for Point 2 (0 to 3 keV)

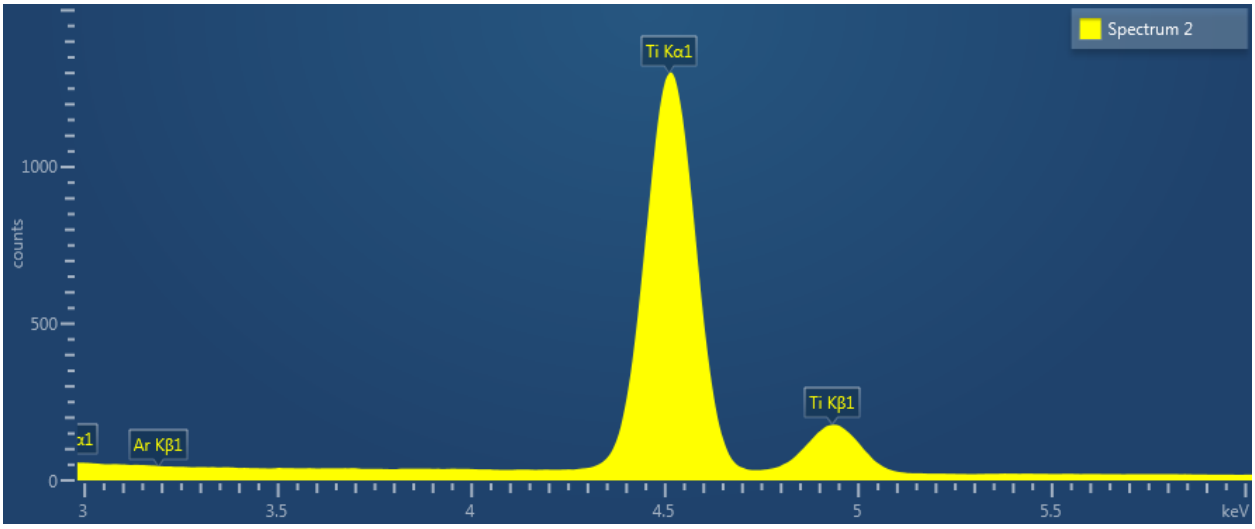

Figure 71 Zoomed-in detail of the EDX spectrum for Point 2 (3 to 6 keV)

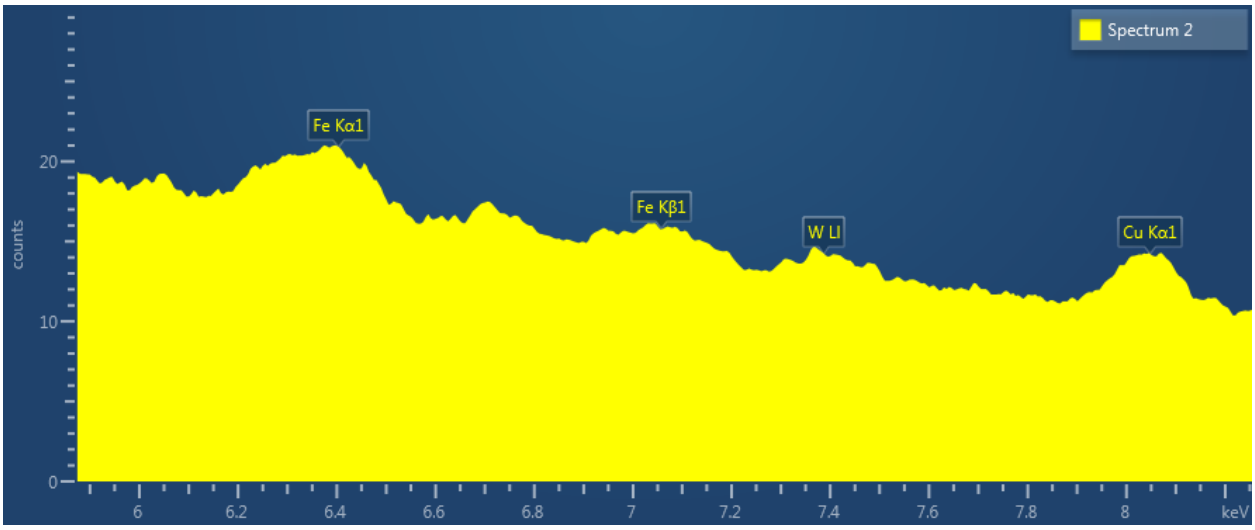

Figure 72 Zoomed-in detail of the EDX spectrum for Point 2 (6 to 8 keV)

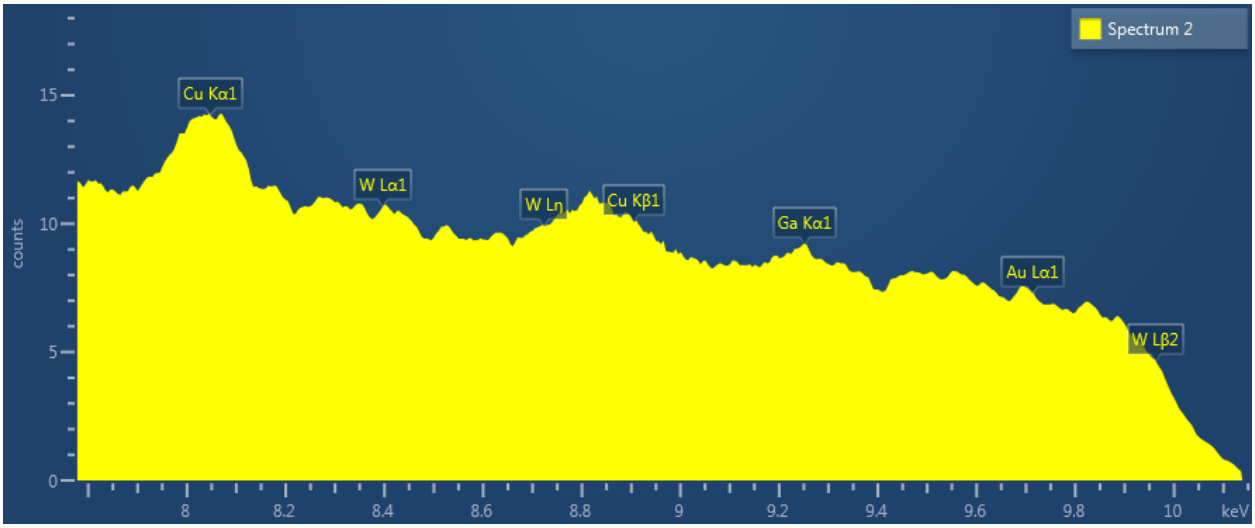

Figure 73 Zoomed-in detail of the EDX spectrum for Point 2 (8 to 10 keV)

- Selected details of the EDX spectrum collected at “Point 3”

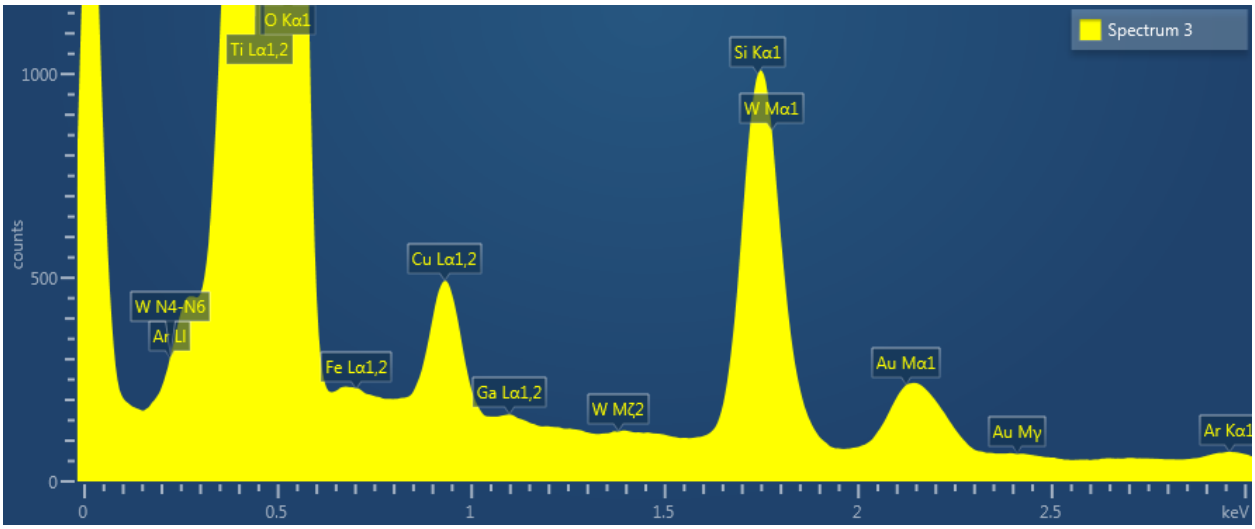

Figure 74 Zoomed-in detail of the EDX spectrum for Point 3 (0 to 3 keV)

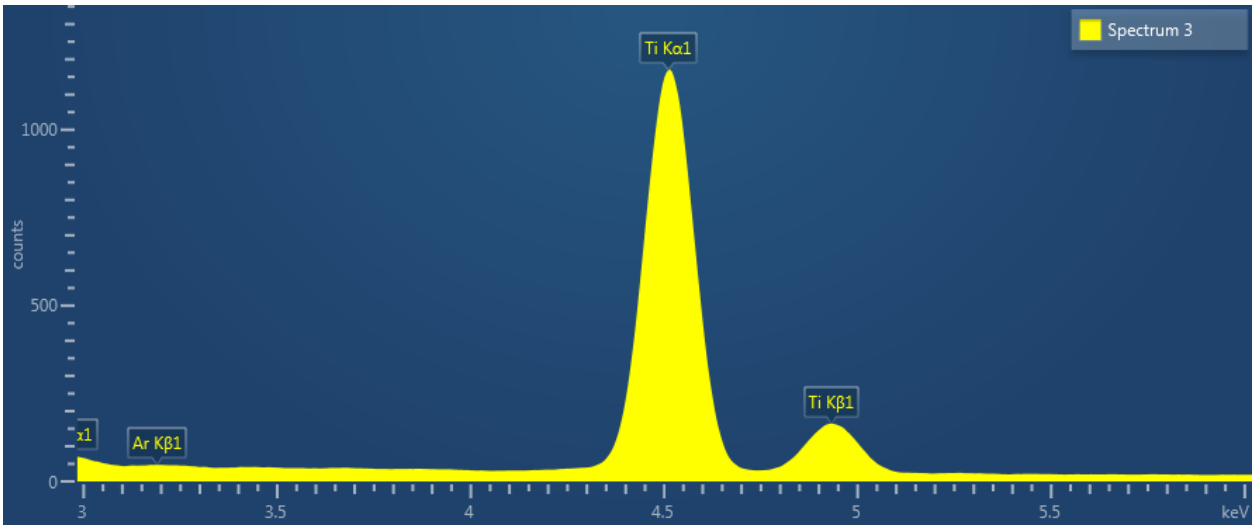

Figure 75 Zoomed-in detail of the EDX spectrum for Point 3 (3 to 6 keV)

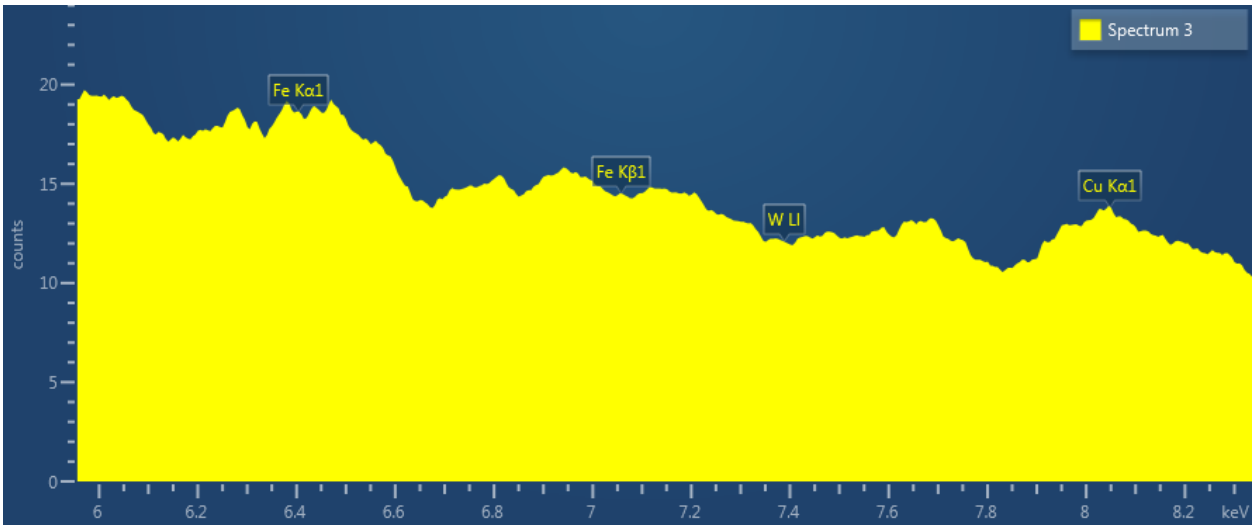

Figure 76 Zoomed-in detail of the EDX spectrum for Point 3 (6 to 8 keV)

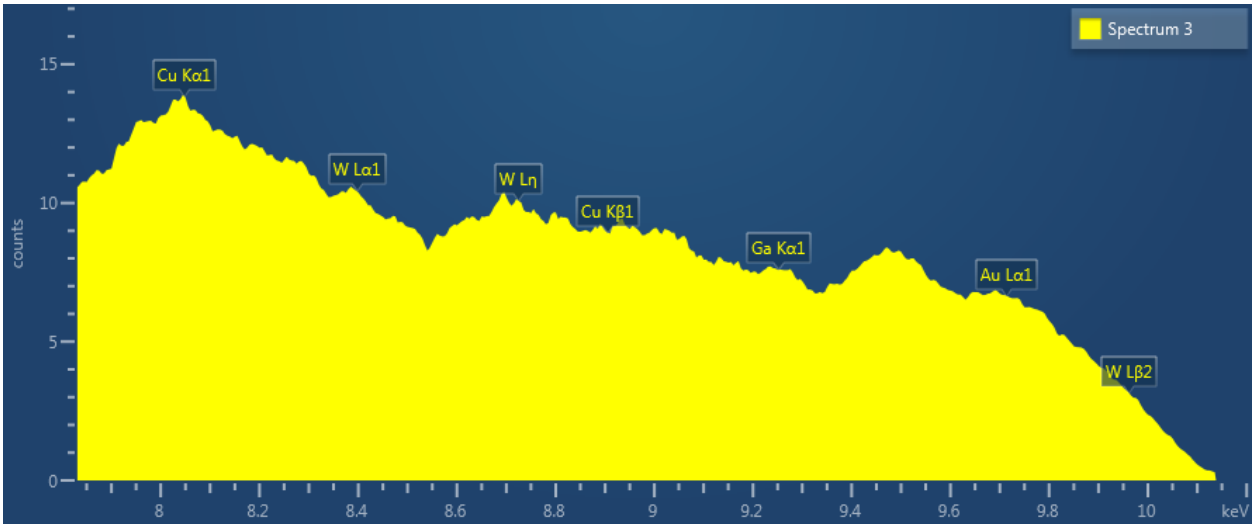

Figure 77 Zoomed-in detail of the EDX spectrum for Point 3 (8 to 10 keV)

- Composition (at%) of elements found in the Fe-TiO_2 specimen along “Line Data 2”

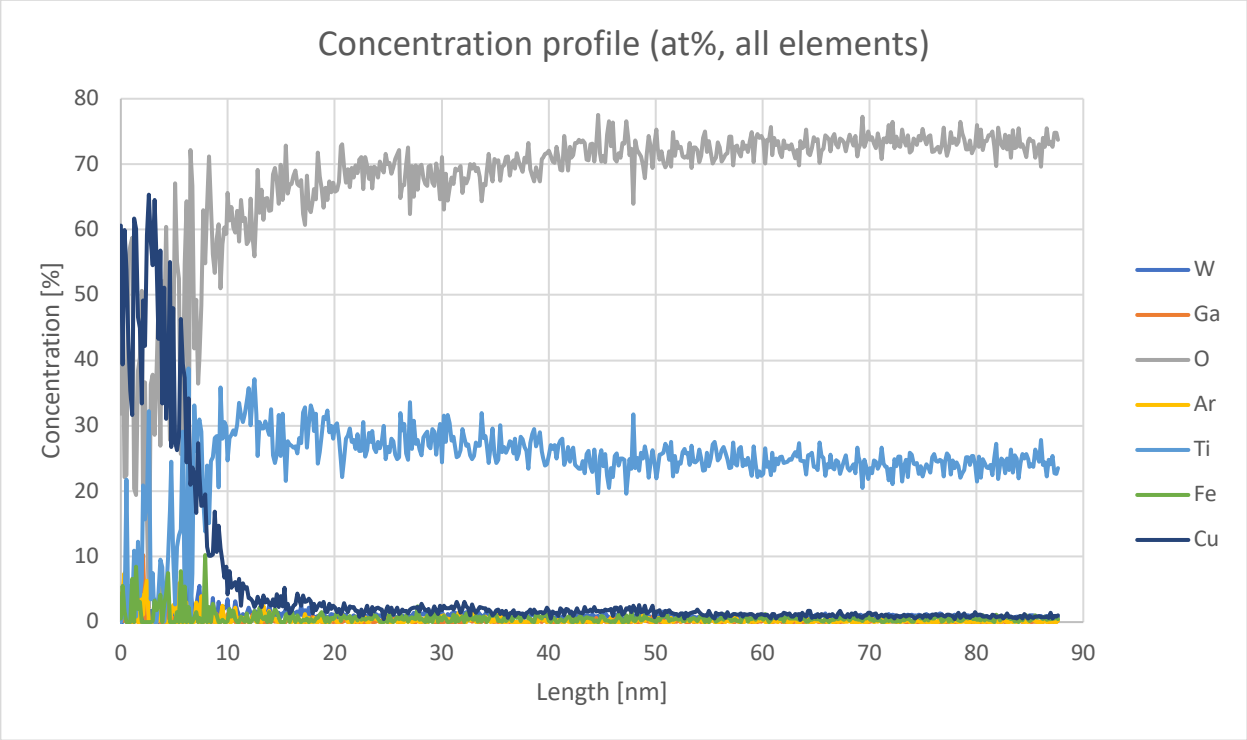

Figure 78 Concentration profile for elements found in Fe-TiO_2 thin specimen along “Line Data 2”

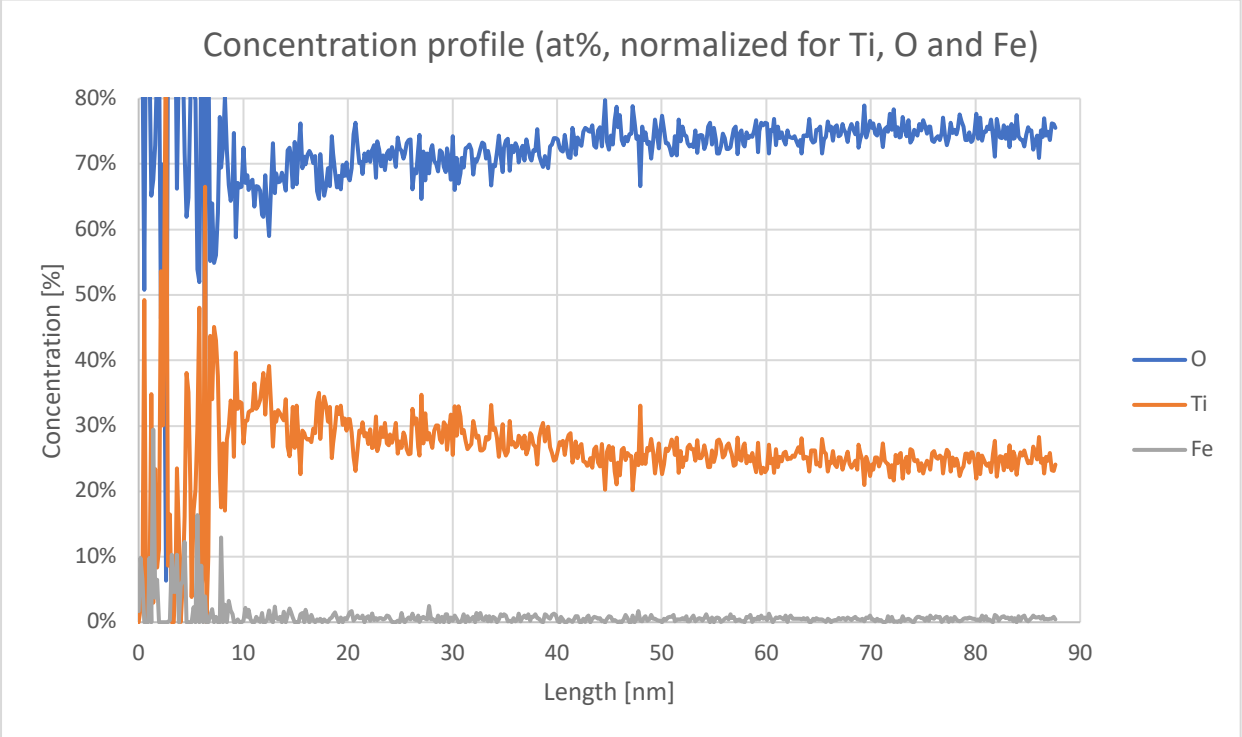

Figure 79 Normalized concentration profile for O, Ti and Fe found in Fe-TiO_2 thin specimen along “Line Data 2”

- EDX elemental mapping attempt using the SU9000 microscope

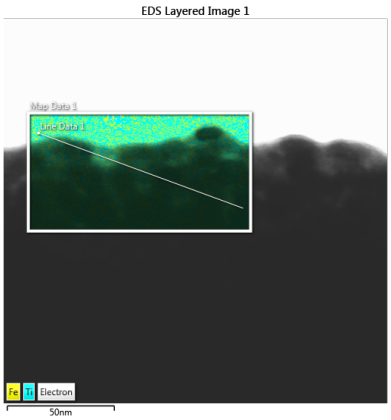

Figure 80 Bright field image showing the specimen area surveyed to generate compositional maps

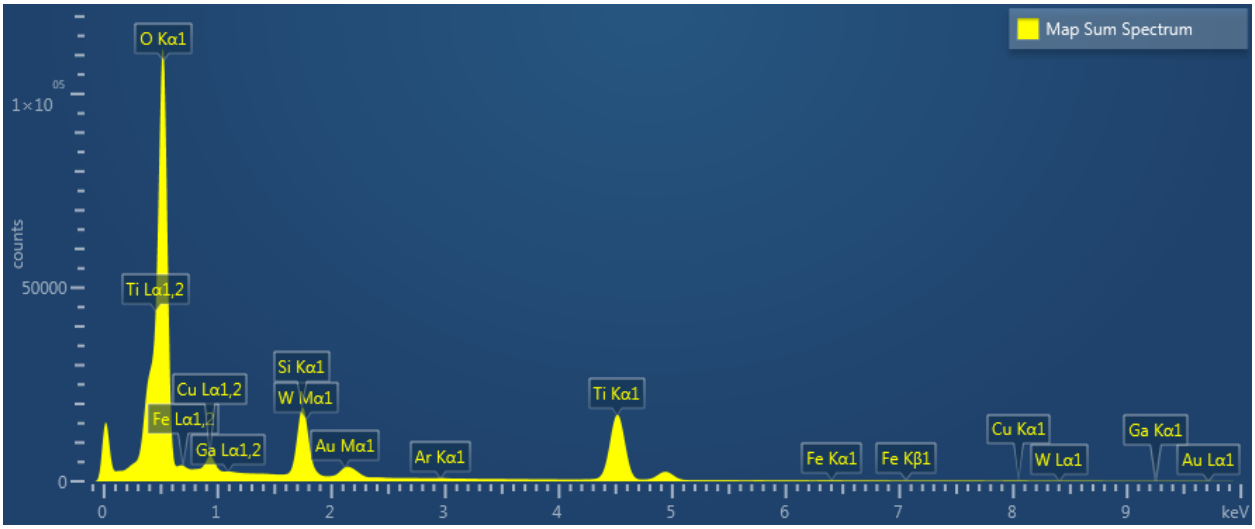

Figure 81 Map Sum EDX spectrum of site labeled “Map Data 1”

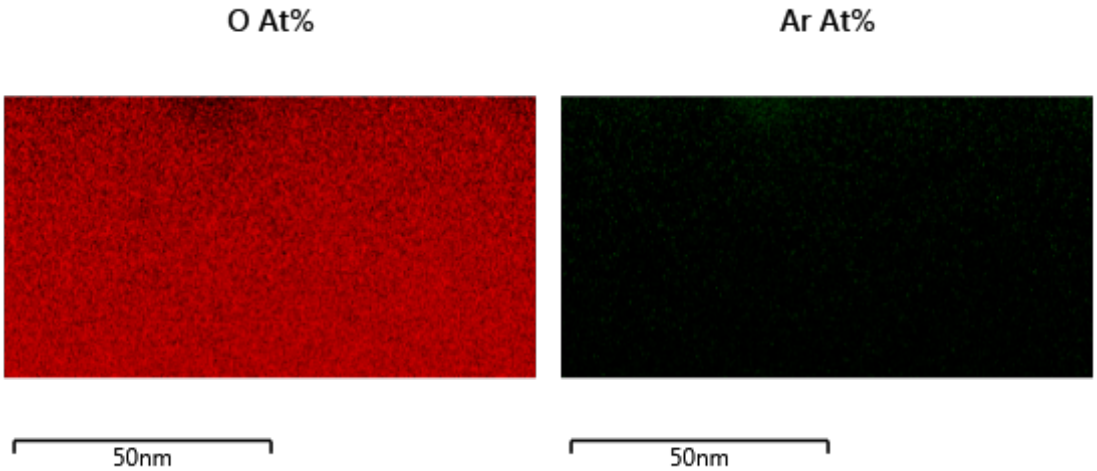

Figure 82 Compositional maps (atomic %) of oxygen (left) and argon (right)

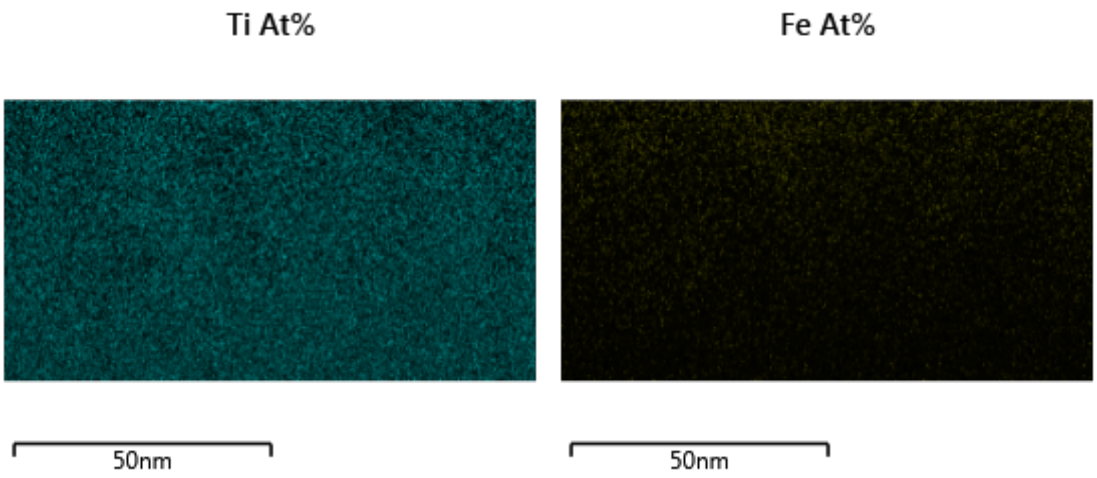

Figure 83 Compositional maps (atomic %) of titanium (left) and iron (right)

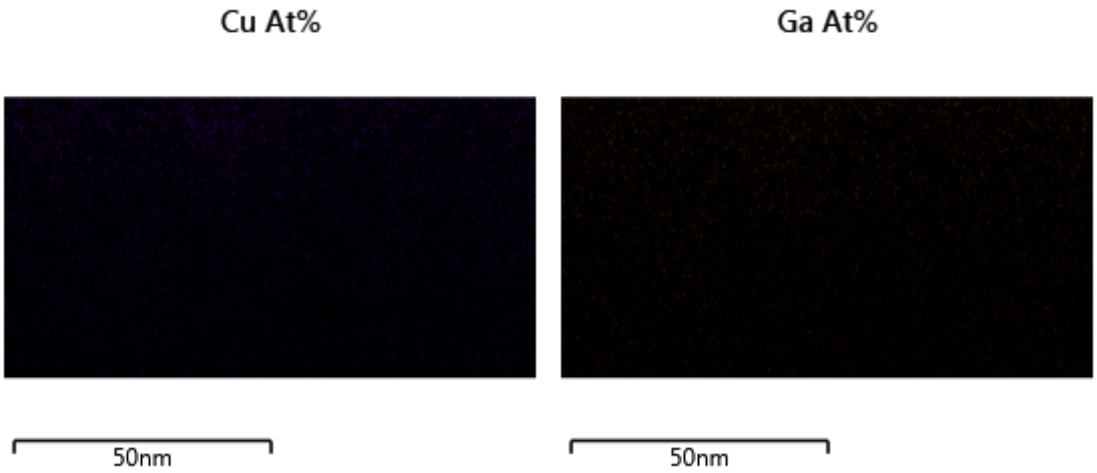

Figure 84 Compositional maps (atomic %) of copper (left) and gallium (right)

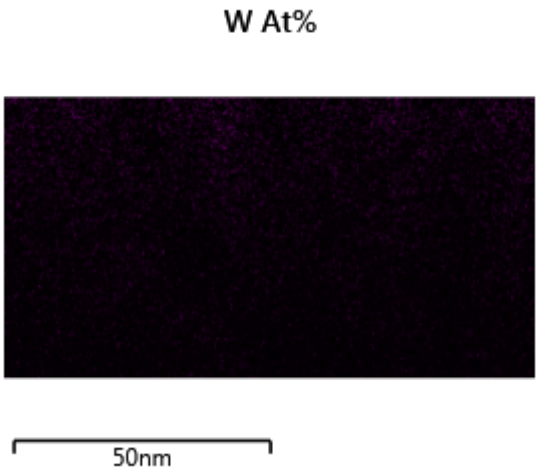

Figure 85 Compositional maps (atomic %) of tungsten

Appendix D

- XRD data

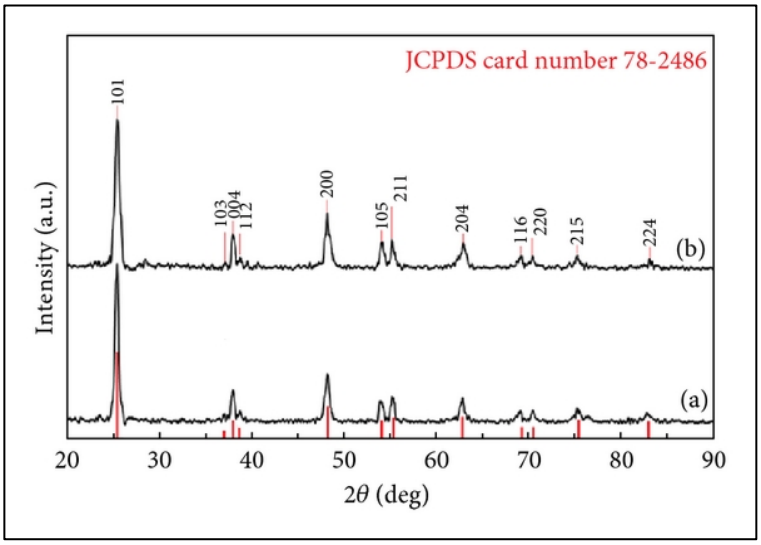

Figure 86 Illustrative x-ray diffraction spectrum of a pure anatase sample (taken from [114])

- Anatase crystallography data

Table 14 X-ray diffracting angles of pure anatase TiO_2, with the corresponding interplanar spacings and Miller indices indicating the diffracting atomic planes [111]

2θ (degrees)	d-spacing (Å)	Miller indices (hkl)
25.23	3.5294	101
36.86	2.4383	103
37.72	2.3847	004
38.46	2.3406	112
47.89	1.8995	200
53.77	1.7049	105
54.89	1.6726	211
61.92	1.4985	213
62.51	1.4858	204
68.59	1.3682	116
70.05	1.3431	220
74.83	1.2688	215
75.78	1.2553	301
82.41	1.1703	224
82.87	1.1650	312

- Theoretical interplanar spacings for anatase titania

Table 15 Possible values of interplanar spacings for anatase titania (calculated using Equation 55), with respective reciprocal distances and theoretical 2θ values (calculated using Equation 41 and $\lambda = 1.54$ Å). Planes present in XRD spectra are bold and highlighted

(hkl)	$h^2 + k^2$	d [A]	1/d [1/nm]	2/d [1/nm]	2θ (degrees)
001	0	9.5390	1.05	2.10	9.27
002	0	4.7695	2.10	4.19	18.60
003	0	3.1797	3.14	6.29	28.06
004	**0**	**2.3848**	**4.19**	**8.39**	**37.72**
005	0	1.9078	5.24	10.48	47.67
100	1	3.7990	2.63	5.26	23.42
101	**1**	**3.5294**	**2.83**	**5.67**	**25.23**
102	1	2.9716	3.37	6.73	30.07
103	**1**	**2.4383**	**4.10**	**8.20**	**36.86**
104	1	2.0198	4.95	9.90	44.88
105	**1**	**1.7049**	**5.87**	**11.73**	**53.77**
110	2	2.6863	3.72	7.45	33.35
111	2	2.5857	3.87	7.73	34.69
112	**2**	**2.3406**	**4.27**	**8.54**	**38.46**
113	2	2.0520	4.87	9.75	44.13
114	2	1.7834	5.61	11.21	51.22
115	2	1.5554	6.43	12.86	59.42
116	**2**	**1.3682**	**7.31**	**14.62**	**68.59**
200	**4**	**1.8995**	**5.26**	**10.53**	**47.89**
201	4	1.8629	5.37	10.74	48.89
202	4	1.7647	5.67	11.33	51.81
203	4	1.6307	6.13	12.26	56.43
204	**4**	**1.4858**	**6.73**	**13.46**	**62.51**
205	4	1.3461	7.43	14.86	69.88
210	5	1.6990	5.89	11.77	53.97
211	**5**	**1.6726**	**5.98**	**11.96**	**54.89**
212	5	1.6005	6.25	12.50	57.59
213	**5**	**1.4985**	**6.67**	**13.35**	**61.92**
214	5	1.3837	7.23	14.45	67.72
215	**5**	**1.2688**	**7.88**	**15.76**	**74.83**
220	**8**	**1.3431**	**7.45**	**14.89**	**70.05**
221	8	1.3300	7.52	15.04	70.85
222	8	1.2929	7.73	15.47	73.21
223	8	1.2373	8.08	16.16	77.08

224	**8**	**1.1703**	**8.54**	**17.09**	**82.41**
225	8	1.0983	9.11	18.21	89.17
300	9	1.2663	7.90	15.79	75.00
301	**9**	**1.2553**	**7.97**	**15.93**	**75.78**
302	9	1.2239	8.17	16.34	78.08
303	9	1.1765	8.50	17.00	81.88
304	9	1.1184	8.94	17.88	87.15
305	9	1.0551	9.48	18.96	93.89
310	10	1.2013	8.32	16.65	79.84
311	10	1.1919	8.39	16.78	80.60
312	**10**	**1.1650**	**8.58**	**17.17**	**82.87**
313	10	1.1238	8.90	17.80	86.63
314	10	1.0729	9.32	18.64	91.87
315	10	1.0166	9.84	19.67	98.64
320	13	1.0537	9.49	18.98	94.05
321	13	1.0473	9.55	19.10	94.80
322	13	1.0288	9.72	19.44	97.06
323	13	1.0002	10.00	20.00	100.85
324	13	0.9638	10.38	20.75	106.24
325	13	0.9223	10.84	21.68	113.41
400	16	0.9498	10.53	21.06	108.53
401	16	0.9451	10.58	21.16	109.32
402	16	0.9315	10.74	21.47	111.71
403	16	0.9100	10.99	21.98	115.80
404	16	0.8823	11.33	22.67	121.79
405	16	0.8502	11.76	23.52	130.11
410	17	0.9214	10.85	21.71	113.58
411	16	0.9451	10.58	21.16	109.32
412	17	0.9047	11.05	22.11	116.89
413	17	0.8850	11.30	22.60	121.18
414	17	0.8595	11.64	23.27	127.52
415	17	0.8297	12.05	24.11	136.61
330	18	0.8954	11.17	22.34	118.85
331	18	0.8915	11.22	22.43	119.70
332	18	0.8801	11.36	22.73	122.32
333	18	0.8619	11.60	23.20	126.87
334	18	0.8383	11.93	23.86	133.75
335	18	0.8106	12.34	24.67	144.00
420	20	0.8495	11.77	23.54	130.33
421	20	0.8461	11.82	23.64	131.32
422	20	0.8363	11.96	23.91	134.38

423	20	0.8207	12.18	24.37	139.88
424	20	0.8002	12.50	24.99	148.89
425	20	0.7760	12.89	25.77	166.84